Formation and Evolution of Protoplanetary Disks

Johan Appelgren

Lund Observatory
Lund University

2019-EXA148

Degree project of 60 higher education credits (for a degree of Master)
May 2019

Supervisor: Michiel Lambrechts

Lund Observatory
Box 43
SE-221 00 Lund
Sweden

Abstract

A star forms with a surrounding protoplanetary disk after the collapse of a molecular cloud core. Subsequently, over a period of several Myr this protoplanetary disk of dust and gas is accreted onto the host star. We model the formation and evolution of such a protoplanetary disk using a one-dimensional numerical model. We find that disks form on a time scale of less than 1 Myr and that the size and mass of the disk at the end of formation depend on the angular momentum of the molecular cloud core, which may explain the large diversity in observed disk masses and radii. The initial disk size subsequently sets its viscous lifetime. In order for the star to accrete the disk within 5 Myr we find that disks need to form very compact (within about 3 au). Dust disk lifetimes are investigated assuming that particles sizes are held constant by the combined effects of coagulation, bouncing and fragmentation. For dust sizes of 0.1 and 0.01 cm we find that the dust disk drains significantly faster than the gas disk, having lifetimes that are at least 2-3 Myr shorter than the 5 Myr simulation. For 0.001 cm sized dust, the dust disk only begins to rapidly drain inwards towards the end of the 5 Myr simulation, but maintaining such small particles would require very low coagulation efficiencies in the outer disk. For these particles with fixed sizes, we find that pebbles can pile up and could form planetesimals though the streaming instability early in the disk evolution at a wide range of orbital radii. With this in mind, we also briefly look into the potential of planet formation via pebble accretion, starting with embryos placed in these streaming instability active regions. We find that giant planets cores of about 10 $M_\oplus$ can emerge after the disk formation phase has ended in a timespan of about 0.25 Myr yr for 0.1 cm sized pebble at an orbit of about 10 au. For 0.01 cm sized pebbles we find that planets are able to grow to masses from a few Mars masses to a few Earth masses, both in the inner disk ($\lesssim$ 5 au) and the outer disk ($\gtrsim$ 10 au).

Acknowledgements

I wish to thank my supervisor Michiel Lambrechts for his help with this project, and for coming up with the idea behind it, so that I had the chance to do this very interesting project. His support and advice on all aspect of the project has been greatly appreciated. I also wish to thank Rebecca Forsberg for her never ending support and help.

Populärvetenskaplig beskrivning

De första idéerna om hur planeterna i solsystemet bildades härstammar från den franske filosifen René Descartes på 1600-talet. Den teori som forskare tror på idag kan spåra sitt ursprung till mitten av 1700-talet, från den svenske forskaren Emanuel Swedenborg och den tyske filosofen Immanuel Kant. Deras hypotes kallas Solnebulosan. Den föreslår att solens planesystem bildades från en disk av gas och stoft som omringade solen när den var ung.

På över 250 år har Swedenborg och Kants teori, i grunden, förändrats förvånandsvärt lite. Vi tror fortfarande att planeter bildas från en disk av damm och stoft, vilket idag kallas för en protoplanetär disk.

Åratal av forskning kring ämnet har avslöjat att det finns flertalet utmaningar att överkomma för att bygga planeter - där många av dessa utmaningar överkommits. En metod som har varit vanlig att använda är att man utgår från en färdigbildad disk designad så att den innehåller tillräckligt mycket gas och stoft för att kunna bilda solsystemet. Innan vi kände till fler planetsystem än vårt eget var detta kanske inte en dum idé, men idag känner vi till tusentals, och upptäcker nya i en rasande fart. Genom dessa upptäckter har det visat sig att vårt solsytem faktiskt skiljer sig en hel del ifrån många av dessa andra planetsystem. En model baserad på solsystemet kan således anses vara bristande i grunden.

Utgår man ifrån en färdigbildad disk tar man inte hänsyn till det stadie då stjärnan och disken bildas. Stjärnor bildas nämligen ifrån stora moln av gas och stoft som kollapsar under sin egen gravitation. I denna process kommer en del av gasen och stoftet att landa så att det bildar en disk runt stjärnan, och det är detta som bildar den protoplanetära disken.

I detta projekt vill vi utveckla en modell där vi inkulderar hur stjärnan och den protoplanetära disken bildas. Genom att använda datorsimuleringar kommer vi undersöka hur det kollapsande molnets egenskaper, så som rotation och massa, påverkar hur disken bildas och utvecklas. Vi vill även undersöka ifall detta kan påverka hur planeter bildas.

Contents

Chapter 1

Introduction

1.1 Star formation

Stars are formed within giant molecular clouds (GMCs), which are over-dense regions of gas and dust in the ISM. As the name suggests, GMCs are dominated by molecular hydrogen gas, rather than atomic gas. GMCs are not homogeneous structures. They contain dense filaments, clumps and cores. Clumps are the regions where stellar clusters form. The most dense regions within clumps are the cores, which is the birthplace of individual star or small star systems (McKee & Ostriker 2007). A core forms a star by collapsing gravitationally. Due to conservation of angular momentum, some of the infalling material will settle onto a disk surrounding the star.

The density profile of molecular cloud cores has been shown to be consistent with that of a Bonnor-Ebert sphere (Alves et al. 2001; Kandori et al. 2005; Kirk et al. 2005; Teixeira et al. 2005). A Bonnor-Ebert sphere is a self-gravitating symmetric sphere under hydrostatic equilibrium, in a pressurised medium, with the maximum mass it can have before becoming gravitationally unstable (Bonnor 1956; Ebert 1957). A supercritical Bonnor-Ebert sphere has a density such that hydrostatic equilibrium will break.

Very young stars, often called young stellar objects (YSOs), are divided into classes based on slope of the spectral energy distribution in the mid infrared. This is done because the dust in the disk around the star is much cooler than the star so it produces an infrared excess in the spectral energy distribution. The classification is thought to follow the evolutionary stages of a YSO. The classes are as follows. Class 0 YSOs are the youngest object and have no infrared excess. These objects still embedded in their envelope, that is some of the molecular cloud core has not yet collapsed onto the star and disk, instead surrounding it as an envelope. Class I objects are still embedded, but have formed a circumstellar disk so they show an infrared excess. Class II objects are no longer embedded and have formed a substantial disk. They therefore show a strong infrared excess. These are the typical

T-Tauri stars. Class III stars have lost most of their circumstellar disk, so they show little infrared excess. A sketch of these stages can be seen in Figure 1.1.1.

An early proposal for how stars can form within molecular cloud cores is the inside out collapse scenario (Shu 1977). The physical state of this collapse is that the collapsing core initially starts out in hydrostatic equilibrium. At some point, the central density of the core is increased by some perturbation. The outer regions of the core are not immediately affected by this, as they feel the same gravitational pull as before. However, the shell closest to the core breaks hydrostatic equilibrium and starts to gravitationally collapse. As one shell has collapsed, the next one loses its pressure support from below and begins to collapse, and so on. Shu (1977) approximates the pre-collapse density profile of the cloud with a singular isothermal sphere, which goes as r^{-2}. It can be shown that this density profile leads to a constant mass accretion rate onto the disk. In this project we will consider the same inside out scenario, but we will use a Bonner-Ebert sphere density profile as in Takahashi et al. (2013), rather than the r^{-2} profile used by Shu (1977). This will lead to a collapse where the mass accretion rate onto the disk is not constant.

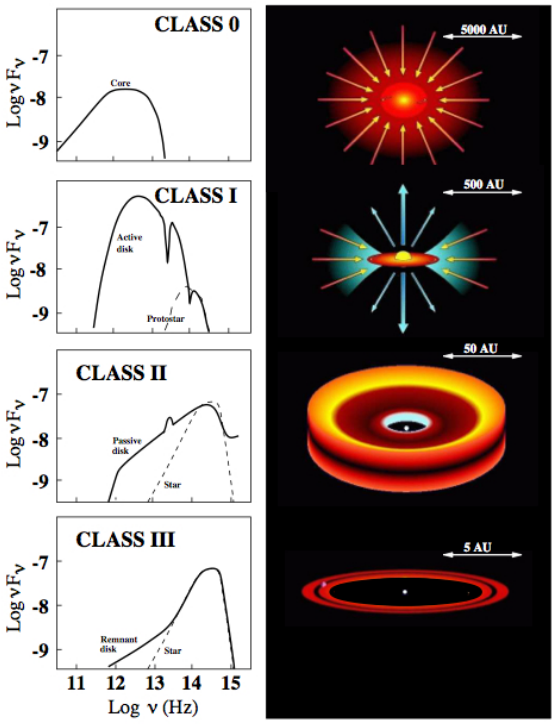

Figure 1.1.1: Illustration of the four stages of young stellar objects (YSOs). In the class 0 stage the YSO is still embedded in its surrounding envelope and radiates no excess in the infrared. Class I objects have disk but are still embedded in the envelope. They show an infrared excess. Class II objects are not embedded, have substantial disks and show a strong excess infrared radiation. By stage III most of the disk has been lost, so the infrared excess is low. Credit: (Isella 2006)

Magnetism in GMC cores affect the formation of disks. Under ideal MHD conditions, formation of disks can be suppressed. In these conditions, the magnetic field lines are frozen into the cloud core. Because of this, as the core collapses it leads to a situation where the magnetic field strength increases rapidly with decreasing radius. As such, material falling through the collapsing cloud eventually becomes dominated by the magnetic field from the star. The magnetic field is able to strip the collapsing material of angular momentum, stopping the inflow of material onto the disk. This is the 'magnetic breaking catastrophe' (Galli et al. 2006). Since we do observe disks around protostars, something is lacking from this picture. There are a number of proposed solutions to this

issue, including e.g., non-ideal MHD, magnetic field rotation misalignment and turbulence (Li et al. 2014). However, the effect of the magnetic field on the collapse is beyond the scope of this project, and will therefore not be considered.

1.2 Protoplanetary disks

The classical protoplanetary disk model is the minimum mass solar nebula (MMSN) (Hayashi 1981). This is a model derived from the solar system. It is constructed by taking all the solids in the solar system, that is rocks and ice, and distributing them according to a power law, extending out to 36 au. This outer radius comes from the assumption that the solids grew into the planets in the solar system with a minimum radial displacement. It is then assumed that there is 100 times more gas than solids in this disk, since that is approximately the dust-to-gas ratio in the interstellar medium. It is further assumed that the dust is evenly spread in the disk. However, one can criticise this model on several ground. First, while it was reasonable to construct a model based on the Solar system in 1981, before other planetary systems had been discovered, today we know thousands of such systems. Using the Solar system as an archetypical planetary systems, even though there is a vast diversity in known exoplanetary systems is somewhat arbitrary. It is also a model which has no time evolution (although one can of course evolve a MMSN through time e.g. viscous evolution), but protoplanetary disk must evolve with time, since they dissipate at some point.

1.2.1 Observational constraints

Protoplanetary disks are short lived on an astronomical time scale. The typical lifetime of a disk is on the order of a 2-3 million years with an upper limit of about 10 million years (Fedele et al. 2010; Haisch et al. 2001). The main process of dissipating the disk is through accretion onto the star. The material accreted onto the disk emits light in the UV range, which then creates an excess of UV emission. It is by measuring this UV excess that accretion from the disk to the star is measured. The observed accretion rate from protoplanetary disks onto protostars are in the range $10^{-11} - 10^{-7}$ $M_\odot$ yr^{-1} (Hartmann et al. 1998, 2016; Manara et al. 2016). Other processes which dissipate the disk include the formation of giant planets and the final clearing of gas by photoevaporation (Owen et al. 2012, 2011, 2010). Examples of observed protoplanetary disks can be seen in Figure 1.2.1.

Najita & Bergin (2018) compared the sizes of class I and class II YSOs and found that class II object have consistently larger radii, as measured by gas tracers, than class I sources. Decreasing disk masses and increasing disk sizes for older objects is consistent with viscous evolution of the gas disk, in which gas can be accreted onto the star by transporting angular momentum outwards in the disk. The physical mechanism behind transporting

the angular momentum could not be determined from the study, but it argues for disks evolving viscously.

Observationally, gas masses are believed to be in the range $10^{-5} - 10^{-1}$ $M_{\odot}$ (Ansdell et al. 2016; Bergin et al. 2013; McClure et al. 2016; Miotello et al. 2017; Pascucci et al. 2016). However, Galván-Madrid et al. (2018) investigated the effect of self-obscuration in protoplanetary disks. They found that current estimates of disk masses can be underestimated by as much as a factor 10. Disk masses between $M_{\rm Disk} = 0.01 - 2M_{\odot}$ were needed to reproduce observed spectral indices. Ballering & Eisner (2019) also found that disk masses were underestimated. They fitted radiative transfer models to spectral energy distributions of 132 disks and found that masses were underestimated by a factor of $\sim 1 - 5$ when using (sub-)millimetre measurements, compared to their results.

Manara et al. (2018) compared the total mass of known exoplanetary system to that of known protoplanetary disks, which are 1-3 Myr old. What they find is that the exoplanetary systems are equally, or more, massive than the most massive protoplanetary dust disks. To explain this, Manara et al. (2018) suggest two solutions. The first solution proposes that planetary cores form early, before these disks are observed. Disk masses tend to decrease with age, it is therefore possible that young disks (< 1 Myr) were massive enough to form the observed exoplanet population. The other solutions is that the disk is refilled with material from the ISM, either continuously or in episodically.

1.2.2 Theoretical work on protoplanetary disk evolution

Protoplanetary disks form together with the star as the rotating molecular cloud core collapses. The cloud core contains too much angular momentum for all of it to be deposited on the star. If angular momentum is conserved, material will therefore land in a disk surrounding the star. A parcel of gas will fall onto a radius in the disk where the Keplerian angular momentum is the same as the angular momentum it had in the rotating cloud. The parcel with highest angular momentum will fall the furthest out at a radius called the centrifugal radius. Each consecutively collapsing spherical shell will have a larger centrifugal radius and the final centrifugal radius will be set by the total angular momentum budget of the cloud core.

Gas being accreted onto the star is losing angular momentum. In order to conserve angular momentum of the system, the angular momentum from the accreted gas must be transported somewhere via some mechanism. One such mechanism is turbulence. The turbulence in the disk can acts as a viscosity, making the disk undergo viscous evolution. In this process, the bulk of the gas is being transported inwards in the disk. Simultaneously, angular momentum is transported outwards. One mechanism of creating turbulence in the disk is the so called magneto-rational instability (MRI) (Balbus & Hawley 1991). They found that disks becomes unstable and turbulent even under a weak magnetic field.

Recent works have however questioned if the MRI is a viable mechanism for angular mo-

mentum transport in protoplanetary disk, as ionisation levels in the disk may be to low. Work by Bai & Stone (2013) has shown that the MRI might be suppressed in the disk. They include the non-ideal MHD effect of Ohmic resistivity and ambipolar diffusion. The results are that the MRI is completely suppressed in the disk. Instead, a magnetocentrifugal wind is created. This wind carries away angular momentum efficiently enough that observed accretion rates onto stars can be explained.

The main component of a protoplanetary disk is the gas disk, but it also contains a dust component. These two components evolve differently, because they are affected by different processes in the disk. There is a pressure gradient present in the disk which the gas is affected by. This gives the gas additional support against the gravitational pull of the star. As a consequence, the gas is able to orbit with a sub-Keplerian velocity and still maintain a stable orbit. The dust disk does not feels this pressure support. If the dust is very small it will be tightly coupled to the gas and follow the gas streamlines. As the dust grows to become larger pebbles, it will begin to decouple from the gas. Because it does not feel the pressure support, it orbits with a Keplerian velocity, i.e. faster than the gas. Due to the difference in velocity, the larger dust particles experience a head wind from the gas. This robs the dust particles of angular momentum, causing them to rapidly drift inwards to the star (Weidenschilling 1977).

It has been shown that the growth and drift time scales of dust in protoplanetary disks are very rapid. Dust grows in size until it reaches a point where it starts drifting radially faster than it grows, at which point it quickly drifts onto the star on time scales of 100-1000 yr (Weidenschilling 1977). This is dubbed the radial drift barrier (Blum & Wurm 2008; Zsom et al. 2010). Particle growth is also limited by collisional fragmentation (Blum & Wurm 2000; Blum et al. 1998; Poppe et al. 1999) and bouncing (Blum & Wurm 2008; Zsom et al. 2010) to mm-cm size. These effects combine into making dust disk lifetimes short, and collisional particle growth to planetesimal sizes of km or more difficult.

The rapid loss of pebbles is problematic. From a theory standpoint it means that planet formation must also be a very rapid process, since the pebbles are the building block from which planetesimals and planets form. More importantly, from observations it appears that the dust is present much longer than the growth and drift suggests, e.g. (Andrews et al. 2016). Something therefore appears to be lacking in our understanding of dust growth and drift.

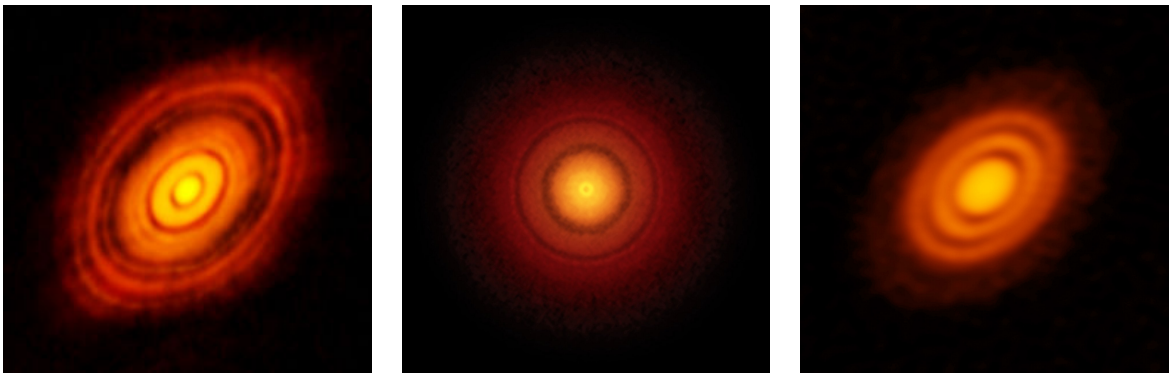

(a) HL Tau (ALMA Partnership et al. 2015)

(b) TW Hydrea (Andrews et al. 2016)

(c) HD163296 (Isella et al. 2016)

Figure 1.2.1: Examples of observed protoplanetary disks. The left panel shows the young system HL Tau. The middle panel shows TW Hydrae which may be as old as 10 Myr. The right panel shows HD163296. These disks are observed in mm emission and what is seen is the dust component of the disk. Clearly visible are ringed structures in the disk, which could be a signature of planet formation.

1.3 Planet formation

The classical model for the formation of giant planets is the so called core accretion scenario (Pollack et al. 1996). In this model, the giant planet core initially grows by acccreting km-sized planetesimals. This process halts once the core reaches its planetesimal isolation mass. Then, the core accretes gas to form a gaseous envelope. At some point, the mass of the gas envelope becomes higher than the mass in the solid core. When this occurs runaway gas accretion begins and the planet is quickly able to accrete a massive gas envelope.

The step of how mm-cm sized pebbles grow to planetesimals is not certain. The currently most promising mechanism is the streaming instability. If enough pebbles are located together, they can start to push on the slower-rotating gas around them. This causes the gas to orbit faster than its previous sub-Keplerian velocity. Pebbles that drift into this region then no longer feel as much gas drag and stick there, further pushing on the gas, increasing its orbital velocity and reducing the drag even more. This can cause a runaway process where enough pebbles become concentrated such that they gravitationally collapse to form planetesimals (Johansen et al. 2007; Youdin & Goodman 2005).

However, core accretion by planetesimal accretion is unsuccessful at explaining the formation of giant planet at large orbital radii (Pollack et al. 1996). This is because the accretion rate of planetesimals decreases rapidly will increasing orbital radius. The formation time scale of Uranus or Neptune like planets becomes longer than the typical time scale of a MMSN-like protoplanetary disk.

A mechanism of growing giant planets which solves the issue with slow planetesimal accretion is the pebble accretion scenario (Lambrechts & Johansen 2012, 2014). This scheme is similar to the core accretion scenario, but instead of accreting km sized planetesimals, the planetary embryo accretes mm-cm sized pebbles. This results in higher mass accretion rate onto the forming planet, allowing it to form within the lifetime of a protoplanetary disk.

1.4 Purpose of this work

In this work we will investigate the formation and evolution of protoplanetary disks starting from the collapse of a molecular cloud core. This will be done by constructing a one-dimensional numerical model. Using this model we will investigate how the angular momentum budget of the molecular cloud core affect the evolution and formation of protoplanetary disks. We will explore how changing rotation rate and mass of the cloud core affects the disk mass, radius and the accretion rate onto the star from the disk. With our disk formation and evolution model we then want to understand how the distribution of dust in the disk is affected by the disk evolution.We assume dust that is of constant size everywhere, and explore the effects of changing the size of the dust. Finally, we will use the dust evolution model to find the implications of our work on the formation of planetesimals and planets.

Chapter 2

Theory

In this chapter we will go through the theory of how we model the molecular cloud core using a Bonnor-Ebert sphere and how it collapses to form a star and protoplanetary disk. From there we will discuss how the protoplanetary disk evolves. The gas disk will evolve viscously, and the dust will evolve via two processes. By drifting due to gas drag and by advecting with the gas due to being coupled to it. We will then give a description of how we model planet formation via pebble accretion and how we model planet migration in the type 1 regime. Finally, we will discuss the angular momentum of the cloud core. We look at observational and numerical constraints on the specific angular momentum of cloud cores, and explain how we use these to determine the rotation rate of the cloud core.

2.1 Bonnor-Ebert sphere

The Bonnor-Ebert sphere (Bonnor 1956; Ebert 1957) is a solution to the Emden equation,

$$\frac{1}{r^2}\frac{\mathrm{d}}{\mathrm{d}r}\left(\frac{r^2}{\rho}\frac{\mathrm{d}P}{\mathrm{d}r}\right) = -4\pi G\rho, \tag{2.1}$$

where r is the radius of the sphere, ρ the density, P the pressure and G the gravitational constant. The Bonnor-Ebert solution to Equation (2.1) has the boundary conditions that the central density is finite, and that the density gradient at the outer radius of the cloud is 0. Using the ideal gas law as the equation of state, Equation (2.1) for an isothermal sphere can be written in terms of density as

$$\frac{1}{r^2}\frac{\mathrm{d}}{\mathrm{d}r}\left(\frac{r^2}{\rho}\frac{\mathrm{d}\rho}{\mathrm{d}r}\right) = -\frac{4\pi G}{c_\mathrm{s}^2}\rho, \tag{2.2}$$

where c_s is the sound speed. From this one can solve for the density profile. Under the approximation that the central density is infinite, the solution can be determined analytically and is the singular isothermal sphere (SIS) (Chandrasekhar 1957; Shu 1977). This has the density profile

$$\rho(r) = \frac{c_s^2}{2\pi G} r^{-2}. \tag{2.3}$$

This sphere extends infinitely far out in space.

As mentioned the Bonnor-Ebert sphere has a finite central density. This complicates the solution and unfortunately an analytical solution to Equation (2.2) does not exist in this case, and it must be solved numerically. How this is done is discussed in Section 3.1.

2.2 Disk formation

The protoplanetary disk forms around the host star as a molecular cloud core collapses. Due to conservation of angular momentum, some of the infalling material will fall onto the protostar, and some onto the disk. This formation scenario is the collapse of a molecular cloud core modelled by a super-critical Bonnor-Ebert sphere, following the Takahashi et al. (2013) prescription. Collapse of the sphere is induced by increasing the density of the cloud core by a factor f, breaking the hydrostatic equilibrium in the Bonnor-Ebert sphere. The innermost shells of the cloud core now begins collapses inwards. The collapse front then expands inside out as pressure support from below is lost, causing more and more of the cloud core to fall towards the star and disk system. Below is a description of how the disk forms.

2.2.1 The collapse of a single shell

The collapsing cloud is divided up into shells. A shell starts with a certain initial radius r_ini, and begins to fall once the collapse front radius, r_CF, reaches the shell. Each collapsing section of the shell lands where its angular momentum matches that of the disk, since the collapse obeys conservation of angular momentum. An illustration of this collapse scenario is shown in Figure 2.2.1.

The velocity of each collapsing shells, u, follows

$$\frac{\mathrm{D}u}{\mathrm{D}t} = \frac{c_\mathrm{s}^2}{\rho}\frac{\partial \rho}{\partial r} - \frac{GM_\mathrm{in}}{r^2} \tag{2.4}$$

$$= \frac{c_\mathrm{s}^2}{r} F(r) - \frac{GM_\mathrm{in}}{r^2}, \tag{2.5}$$

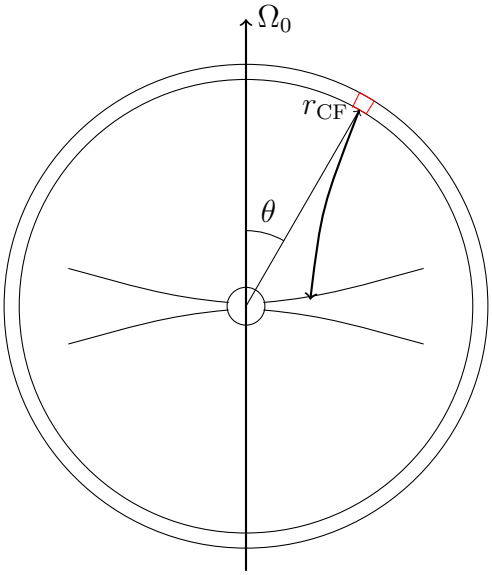

Figure 2.2.1: This illustration shows a single shell of the molecular cloud core collapsing onto the protoplanetary disk. The cloud core is in solid rotation with rotational velocity Ω_0, and the collapse obeys conservation of angular momentum. A collapsing parcel of gas (red box) starts out at radius of the collapse front, r_{CF}, and angle θ from the rotation axis. The parcel will land at a radius in the disk where the parcels angular momentum is the same as the Keplerian angular momentum around the star.

where c_{s} is the sound speed of the cloud, which is constant due to the cloud having constant temperature. ρ is the density of the cloud, G is the gravitational constant, r the current radius of the shell and M_{in} is the mass interior to the collapsing shell. The function $F(r) = r/\rho \ \partial\rho/\partial r$ is introduced here. For a Bonnor-Ebert sphere this is of order unity. Further, this is approximated as $F(r) = F(r_{\mathrm{CF}}) =$ constant, where r_{CF} is the radius of a shell as it beings to collapse. The justification of this is that each shell will spend most of its time at this radius since the collapse phase of each shell is relatively short. In hydrostatic equilibrium $F(r)$ is given by

$$F(r) = \frac{GM}{c_{\mathrm{s}}^2 r}. \tag{2.6}$$

To break hydrostatic equilibrium, the mass of the sphere is increases by a factor $f = 1.4$. Therefore, before the mass is increased by the factor f, hydrostatic equilibrium for a shell gives $F(r_{\mathrm{CF}})$ as

$$F(r_{\mathrm{CF}}) = \frac{GM_{\mathrm{in}}}{f c_{\mathrm{s}}^2 r_{\mathrm{CF}}}. \tag{2.7}$$

The acceleration, a, that parcel of gas feels is given by

$$a = -\frac{GM_{\rm in}}{r^2} + \frac{c_{\rm s}^2}{r} F(r_{\rm CF}) \tag{2.8}$$

$$= -GM_{\rm in}\left(\frac{1}{r^2} - \frac{1}{f r_{\rm CF}}\frac{1}{r}\right) \tag{2.9}$$

The acceleration can also be written in terms of the velocity, u, as

$$a = \frac{{\rm d}u}{{\rm d}t} = \frac{{\rm d}u}{{\rm d}r}\frac{{\rm d}r}{{\rm d}t} = u\frac{{\rm d}u}{{\rm d}t} = \frac{1}{2}\frac{{\rm d}u^2}{{\rm d}r}. \tag{2.10}$$

Using this and Equation (2.9), we get the velocity as

$$u(r) = \pm\sqrt{2GM_{\rm in}\left(\frac{1}{r} - \frac{1}{r_{\rm CF}} + \frac{1}{f r_{\rm CF}}\ln\left(\frac{r}{r_{\rm CF}}\right)\right)}. \tag{2.11}$$

With $u = {\rm d}r/{\rm d}t$ this is set up as an differential equation and solved to find the infall time, the time it takes for a shell to reach $r = 0$. The variable substitution $R = r/r_{\rm CF}$ is also made. The infall time then becomes

$$t_{\rm infall} = \sqrt{\frac{r_{\rm CF}^3}{M_{\rm in}}} \cdot \sqrt{\frac{1}{2G}} \int_0^1 \frac{{\rm d}R}{\sqrt{\frac{1}{f}\ln R + \frac{1}{R} - 1}} \tag{2.12}$$

$$= \sqrt{\frac{r_{\rm CF}^3}{\int_0^{r_{\rm CF}} 2\pi r^2 \rho(r){\rm d}r}} \cdot \sqrt{\frac{1}{2G}} \int_0^1 \frac{{\rm d}R}{\sqrt{\frac{1}{f}\ln R + \frac{1}{R} - 1}}. \tag{2.13}$$

Joining all constant into one as

$$\beta = \sqrt{\frac{1}{2G}} \int_0^1 \frac{{\rm d}R}{\sqrt{\frac{1}{f}\ln R + \frac{1}{R} - 1}}, \tag{2.14}$$

gives the final expression for the infall time for a shell at initial radius $r_{\rm CF}$ as

$$t_{\rm infall} = \sqrt{\frac{r_{\rm CF}^3}{M_{\rm in}}}\,\beta = \sqrt{\frac{r_{\rm CF}^3}{\int_0^{r_{\rm CF}} 2\pi r^2 \rho(r){\rm d}r}}\,\beta. \tag{2.15}$$

From Equation (2.15) we can also get the expansion of the collapse front per unit time as ${\rm d}r_{\rm CF}/{\rm d}t$.

2.2.2 Mass infall rate

It is assumed that all sections of a shell collapses onto the disk at the same time and that angular momentum is conserved during the collapse. Each parcel of gas will therefore land on the disk where its angular momentum matches that of the disk. This is the point where the centrifugal and gravitational forces are in balance.

The mass contained within a spherical shell of radius $r_{\rm CF}$ and thickness per unit time $\mathrm{d}r_{\rm CF}/\mathrm{d}t$ is given by $4\pi\rho r_{\rm CF}^2 \mathrm{d}r_{\rm CF}/\mathrm{d}t$. This gives the amount of mass swept up per unit time as the collapse front expands, which is also the amount of mass which lands on to the disk per unit time.

$$\dot{M}_{\rm infall} = 4\pi\rho r_{\rm CF}^2 \frac{\mathrm{d}r_{\rm CF}}{\mathrm{d}t}. \tag{2.16}$$

To find a full expression for this we need an expression for $\mathrm{d}r_{\rm CF}/\mathrm{d}t$. This can be found by differentiating Equation (2.15) with respect to $r_{\rm CF}$, giving

$$\frac{\mathrm{d}r_{\rm CF}}{\mathrm{d}t} = \frac{2r_{\rm CF}\beta^2}{3t\beta^2 - 2\pi t^3\rho(r_{\rm CF})}. \tag{2.17}$$

In this system the mass accretion onto the disk is dependant on time. This is different from the singular isothermal sphere (SIS) of (Shu 1977). The SIS is a Bonnor-Ebert sphere approximated as having an infinite central density. The resulting density profile is

$$\rho_{\rm SIS} = \frac{c_{\rm s}^2}{2\pi G r^2}. \tag{2.18}$$

Using Equation (2.13), the infall time for the SIS is

$$t_{\rm infall,SIS} = \sqrt{\frac{r_{\rm CF}^3}{2G\int_0^{r_{\rm CF}} 2\pi r^2 \dfrac{c_{\rm s}^2}{2\pi G r^2}\mathrm{d}r}} \cdot \int_0^1 \frac{\mathrm{d}R}{\sqrt{\dfrac{1}{f}\ln R + \dfrac{1}{R} - 1}} \tag{2.19}$$

$$= \frac{r_{\rm Cf}}{2^{1/2}c_{\rm s}} \cdot \int_0^1 \frac{\mathrm{d}R}{\sqrt{\dfrac{1}{f}\ln R + \dfrac{1}{R} - 1}}. \tag{2.20}$$

From this one can then find $\mathrm{d}r_{\rm CF}/\mathrm{d}t$ as

$$\mathrm{d}r_{\rm CF}/\mathrm{d}t|_{\rm SIS} = 2^{1/2}c_{\rm s} \cdot \left(\int_0^1 \frac{\mathrm{d}R}{\sqrt{\dfrac{1}{f}\ln R + \dfrac{1}{R} - 1}} \right)^{-1}. \tag{2.21}$$

Now, using Equations (2.16), (2.18), and (2.21), the mass accretion rate for a SIS in this collapse scenario is

$$\dot{M}_{\rm SIS} = 1.02\ \frac{c_{\rm s}^3}{G}. \tag{2.22}$$

2.3 Distribution of mass across the disk

To get the mass infall rate per unit disk radius, a, the variable is changed from disk radius a, to angular momentum j, and then from angular momentum to the angle θ, as seen in Figure 2.2.1. The infall rate per unit disk radius can then be expressed as

$$\frac{\partial \dot{M}_{a,\text{infall}}}{\partial a} = 2\frac{\partial \dot{M}_{a,\text{infall}}}{\partial \theta}\frac{\partial \theta}{\partial j}\frac{\partial j}{\partial a} \tag{2.23}$$

$\dot{M}_{a,\text{infall}}$ is the total mass that lands on the disk within radius a. The factor 2 comes from the fact that material falls onto the disk both sides of the disk. The small parcel of gas with the same angular momentum in Figure 2.2.1, has the thickness $\mathrm{d}r_{\text{CF}}$ and width $\mathrm{d}\theta$. The mass of this parcel is given by

$$\mathrm{d}M_a = 2\pi\rho \cdot (\sin\theta\ r_{\text{CF}}) \cdot (r_{\text{CF}}\ \mathrm{d}\theta)\mathrm{d}r_{\text{CF}}. \tag{2.24}$$

Differentiating this with respect to t, one can show that the infall rate per unit angle, i.e. derivative of Equation (2.16) with respect to θ, is

$$\frac{\partial \dot{M}_{a,\text{infall}}}{\partial \theta} = \frac{\dot{M}}{2}\sin\theta. \tag{2.25}$$

With this, the infall rate per unit radius is

$$\frac{\partial \dot{M}_{a,\text{infall}}}{\partial a} = \dot{M}\sin\theta\frac{\partial \theta}{\partial j}\frac{\partial j}{\partial a}. \tag{2.26}$$

The angular momentum of a parcel in the shell at radius r_{CF} and angle θ from the rotation axis of the cloud is given by

$$j = \left(r_{\text{CF}}\sin\theta\right)^2\Omega_0. \tag{2.27}$$

Solving this for $\sin^2\theta$ and differentiating with respect to j one finds

$$\frac{\partial \theta}{\partial j} = \frac{1}{\sin\theta}\frac{1}{2\Omega_0 r_{\text{CF}}^2}\left(1 - \frac{j}{\Omega_0 r_{\text{CF}}^2}\right)^{-1/2}. \tag{2.28}$$

Inserting this into Equation (2.23), one gets the mass infall rate per unit radius as

$$\frac{\partial \dot{M}_{a,\text{infall}}}{\partial a} = \frac{\dot{M}_{\text{infall}}}{2\Omega_0 r_{\text{CF}}^2}\left(1 - \frac{j}{\Omega_0 r_{\text{CF}}^2}\right)^{-1/2}\frac{\partial j}{\partial r}. \tag{2.29}$$

This is also the mass infall rate that Takahashi et al. (2013) arrives at. Ω_0 is the angular frequency of the rotating molecular cloud, r_{CF} is the initial radius of the currently collapsing shell, and j is the angular momentum of the collapsing gas parcel. We can convert the source term in Equation (2.29) to a surface density source by dividing it by $1/2\pi a$,

$$\frac{\partial \Sigma}{\partial t} = \frac{1}{2\pi a}\frac{\partial \dot{M}_{a,\text{infall}}}{\partial a} = \frac{1}{2\pi r}\frac{\dot{M}_{\text{infall}}}{2\Omega_0 r_{\text{CF}}^2}\left(1 - \frac{j}{\Omega_0 r_{\text{CF}}^2}\right)^{-1/2}\frac{\partial j}{\partial r}. \tag{2.30}$$

2.3.1 Formulation in terms of the centrifugal radius

The angular momentum of a collapsing parcel, j, is given by Equation (2.27). Since angular momentum is conserved, this equals the Keplerian angular momentum in the disk where the parcel lands. Therefore, j is also

$$j = (GMa)^{1/2}. \tag{2.31}$$

Here, M is the mass contained in the disk within the radius a. One can now identify that the $\Omega_0 r_{\rm CF}^2$ term in Equation (2.30) is the maximum angular momentum in the currently collapsing shell, i.e. where $\theta = 90^\circ$ and $\sin\theta = 1$. This will have the same value as the angular momentum at the outer most radius where material lands on the disk, which is the centrifugal radius, $R_{\rm c}$. Equating these two gives

$$\Omega_0 r_{\rm CF}^2 = (GMR_{\rm c})^{1/2}. \tag{2.32}$$

Using these two equations in Equation (2.30), one finds the source term as

$$S_{\rm g}(r,t) = \frac{\partial\Sigma}{\partial t} = \frac{\dot{M}_{\rm infall}}{8\pi R_{\rm c}^2}\left(\frac{r}{R_{\rm c}}\right)^{-3/2}\left[1-\left(\frac{r}{R_{\rm c}}\right)^{1/2}\right]^{-1/2}. \tag{2.33}$$

This is also the source term that Hueso & Guillot (2005) derived for their model for the formation of a protoplanetary disk.

2.4 Evolution of protoplanetary disk

2.4.1 Viscous evolution of the gas disk

The turbulent viscosity, ν, of the disk is parametrized using the α disk model prescription by Shakura & Sunyaev (1973). In this prescription ν takes the form

$$\nu = \alpha H_{\rm g} c_{\rm s}, \tag{2.34}$$

where $H_{\rm g}$ is the scale height of the disk, given by

$$H_{\rm g} = \frac{c_{\rm s}}{\Omega}, \tag{2.35}$$

where Ω the Keplerian angular velocity. The sound speed is coupled to the temperature and the method used to calculate this is discussed in Section 3.4. α is a parameter < 1. From observations and theoretical work, α values in the range $10^{-3} - 10^{-1}$ have been found (Hartmann et al. 1998; Pinte et al. 2016).

In the growth phase the disk it is expected to becomes massive relative to the star and possibly become gravitationally unstable. Angular momentum can then be transported in the disk via gravitational torques (Zhu et al. 2010). This can happen if the Toomre parameter is,

$$Q = \frac{c_{\rm s}\Omega_k}{\pi G\Sigma} \lesssim 2. \tag{2.36}$$

This would effectively give a higher α value. α from the gravitational torque can be modelled as

$$\alpha_Q = \exp\left[-Q^4\right], \tag{2.37}$$

Takahashi et al. (2013); Zhu et al. (2010). The viscosity that does not arise from the gravitational torque is denoted as $\alpha_{\rm m}$. The total value of α is then given by

$$\alpha = \alpha_Q + \alpha_{\rm m}. \tag{2.38}$$

Pringle (1981) expresses the viscous time evolution of the surface density, Σ, in an accretion disk as

$$\frac{\partial\Sigma_{\rm g}}{\partial t} = \frac{3}{r}\frac{\partial}{\partial r}\left[r^{1/2}\frac{\partial}{\partial r}\left(\nu\Sigma_{\rm g}r^{1/2}\right)\right] \tag{2.39}$$

Here, r is the radius in the disk and ν is the turbulent viscosity. This expression comes from the continuity equation and angular momentum conservation. In cylindrical coordinates, the continuity equation is

$$\frac{\partial\Sigma_{\rm g}}{\partial t} = -\frac{1}{r}\frac{\partial}{\partial r}\left(r\Sigma_{\rm g}v_{\rm r}\right), \tag{2.40}$$

where $v_{\rm r}$ is the radial velocity. Conservation of angular momentum leads to the following equation,

$$\frac{\partial}{\partial t}\left(r^2\Omega\Sigma_{\rm g}\right) + \frac{1}{r}\frac{\partial}{\partial r}\left(\Sigma_{\rm g}r^3\Omega v_{\rm r}\right) = \frac{1}{2\pi r}\frac{\partial G}{\partial r}. \tag{2.41}$$

Ω is the angular frequency, and the torque G is given by

$$G = 2\pi r\cdot\nu\Sigma_{\rm g}r\frac{{\rm d}\Omega}{{\rm d}r}\cdot r. \tag{2.42}$$

Under the assumption of a point mass Keplerian potential, the angular frequency is proportional to the radius as $\Omega\propto r^{-3/2}$. Using this, Equations (2.40) and (2.41) combine into Equation (2.39).

Such a disk evolves by gas being accreted towards the central object, the protostar in the case of a protoplanetary disk. As this gas moves inwards in the disk, it will lose

angular momentum. Because the angular momentum of the system must be conserved, this accretion of gas onto the star is accompanied by a simultaneous flow of gas outwards in the disk. This gas gains angular momentum, conserving it as a whole. The mass accretion rate through the disk is given by

$$\dot{M}_{\text{accrete}} = 3\pi\nu\Sigma_{\text{g}}. \tag{2.43}$$

The accretion rate through the disk is constant. This rate is therefore also the rate at which mass is accreted from the disk onto the star. Equation (2.39) can be combined with the source term from the collapsing cloud core. This is done through simple addition of the two parts,

$$\frac{\partial\Sigma_{\text{g}}}{\partial t} = \frac{3}{r}\frac{\partial}{\partial r}\left[r^{1/2}\frac{\partial}{\partial r}\left(\nu\Sigma_{\text{g}}r^{1/2}\right)\right] + S(r,t). \tag{2.44}$$

2.4.2 Evolution of the dust

Particle drift

A drifting dust particle in a protoplanetary disk moves with the radial velocity given by Equation (2.45) (Nakagawa et al. 1986)

$$v_{\text{r}} = -\frac{2\tau_{\text{f}}}{1+\tau_{\text{f}}^2}\ \eta\ v_{\text{k}} \tag{2.45}$$

where τ_{f} is the Stokes number, a measure of how aerodynamically coupled a particle is to the gas, ϵ is the dust-to-gas ratio, v_{k} is the Keplerian velocity and η is a dimensionless parameter which gives the pressure support of the gas. This equation is valid as long as $\epsilon << 1$, otherwise the 1 in the denominator is replaced by $(1+\epsilon)^2$. It is given by

$$\eta = -\frac{1}{2}\left(\frac{H_{\text{g}}}{r}\right)^2\frac{\partial\ln P}{\partial\ln r}. \tag{2.46}$$

In this equation, $\partial\ln P/\partial\ln r = -2.75$, for a disk with a temperature structure that goes as $r^{-1/2}$ and a radial surface density slope of -1. This approximation hold well for most of the disk, during most of the evolution. However, in the early times and the outer parts of the gas disk, the radial surface density slope can be steeper than -1 due to the exponential edge of the disk, which gives a large pressure gradient and $\dfrac{\partial\ln P}{\partial\ln r}$ has a larger absolute value. We will nevertheless use a fixed value for $\partial\ln P/\partial\ln r$ in our numerical simulation in order to prevent issues near the edge of the disk, which causes the dust surface density to become negative just outside the edge of the dust disk.

The formula for calculating the Stokes number depends on in which drag regime the particles are. It will depend on the mean free path of the particles, λ_{mfp}. In the mid-plane of

the disk it is given as

$$\tau_{\rm s} = \begin{cases} \dfrac{\rho_\bullet\ R_\bullet}{\rho_{0,g} c_{\rm s}} \Omega_k = \dfrac{\sqrt{2\pi}\rho_\bullet\ R_\bullet}{\Sigma_{\rm g}} & \text{if } \lambda_{\rm mfp} > \dfrac{4}{9} R_\bullet, \\ \dfrac{4 R_\bullet^2 \rho_\bullet}{9 \lambda_{\rm mfp} \rho_{0,g} c_{\rm s}} \Omega_k = \dfrac{4 R_\bullet^2 \rho_\bullet}{9 \lambda_{\rm mfp}} \dfrac{(2\pi)^{1/2}}{\Sigma_{\rm g}} & \text{if } \lambda_{\rm mfp} < \dfrac{4}{9} R_\bullet, \end{cases} \tag{2.47}$$

(Youdin 2010), where one uses that the gas surface density is given by

$$\Sigma_{\rm g} = \sqrt{2\pi} \rho_0 H_{\rm g}. \tag{2.48}$$

The first case, when $\lambda_{\rm mfp} > 4/9 R_\bullet$ is called the Epstein regime and the second case is called the Stokes regime. The mean free path is given by

$$\lambda_{\rm mfp} = \frac{m_{\rm g}}{\sigma_{\rm mol} \rho_{\rm g}}, \tag{2.49}$$

where $m_{\rm g}$ is the molecular gas mass and $\sigma_{\rm mol} = 2.0 \cdot 10^{-15}$ cm^2 is the molecular collision cross section.

Dust surface density

The dust surface density evolution can be evolved through the following continuity equation,

$$\frac{\partial \Sigma_{\rm d}}{\partial t} = -\frac{1}{r} \frac{\partial}{\partial r} \left(r \Sigma_{\rm d} v_{\rm r} \right). \tag{2.50}$$

$\Sigma_{\rm d}$ is the dust surface density, r the radius in the disk, and $v_{\rm r}$ the radial velocity of the dust. For dust particles $v_{\rm r}$ is given by Equation (2.45). Dust particles that are completely or partially coupled with the gas will also feel the additional contribution from the radial gas flow.

2.5 Giant planet formation

2.5.1 Pebble accretion

The cores of giant planets can grow by accreting dust pebbles entering within approximately the Hill sphere of the core. When the radius within which pebbles are accreted onto the planet core is smaller than the dust scale height, pebble accretion proceeds in the 3D regime. In this case the accretion rate onto a planet core can be given by

$$\dot{M}_{\rm Core} = \pi t_{\rm fric} G M_{\rm core} \frac{\Sigma_{\rm d}}{\sqrt{2\pi} H_{\rm d}}, \tag{2.51}$$

(Lambrechts et al. 2019). $M_{\rm core}$ is the mass of the planet core, $H_{\rm d}$ is the scale height of the dust, which is assumed to be $H_{\rm d} = 0.01 H_{\rm g}$. The motivation for this choice is that in the observed young disk HL Tau, the dust appears to be well settled towards the mid plane (Pinte et al. 2016). $t_{\rm fric}$ is the friction time, given by

$$t_{\rm fric} = \frac{\rho_\bullet R_\bullet}{\rho_0 c_{\rm s}}. \tag{2.52}$$

$R_\bullet$ is the radius of the dust particles, $\rho_\bullet$ is the particle density, which is taken as $\rho_\bullet = 1.6$ g cm^{-3} (Birnstiel et al. 2012), and ρ_0 is midplane density.

2.5.2 Planet migration

Planets embedded in a protoplanetary disk will create spiral density waves outside and inside the planet. These density waves will exert a torque on the planet. The torques are not of equal strength, with the outer density wave exerting a stronger torque. The net effect of this is that the planet loses angular momentum and migrates inwards (Goldreich & Tremaine 1980; Ward 1997). This is the so-called type 1 migration. A planet undergoing this type of migration moves at a rate which can be expressed as

$$\frac{{\rm d}r}{{\rm d}t} = -c \frac{M_{\rm c}}{M_\star} \frac{\Sigma_{\rm g} r^2}{M_\star} \left(\frac{H}{r} \right)^{-2} v_{\rm k} \tag{2.53}$$

(Lambrechts & Johansen 2014; Paardekooper et al. 2010). Here, c is a parameter whose value depends on the pressure and temperature gradients in the disk. In the isothermal regime this can be taken to be $c = 2.8$ (Paardekooper et al. 2010).

2.6 Cloud core angular momentum

The specific angular momentum of the molecular cloud core is the ratio of angular momentum to mass,

$$\frac{J}{M} = \frac{I \Omega_0}{M}. \tag{2.54}$$

M is the mass of the cloud core and J is the angular momentum. This is in turn determined by the moment of inertia, I, and the rotation rate, which we assume to be uniform, Ω_0 of the cloud core. It has been shown by from observations and numerical simulations of molecular cloud cores that the specific angular momentum scales with the core radius as $\sim R^{3/2}$, with a large spread, e.g. (Burkert & Bodenheimer 2000; Goodman et al. 1993). Figure 2.6.1 shows this relation from the observed molecular cloud cores of Goodman et al. (1993). The

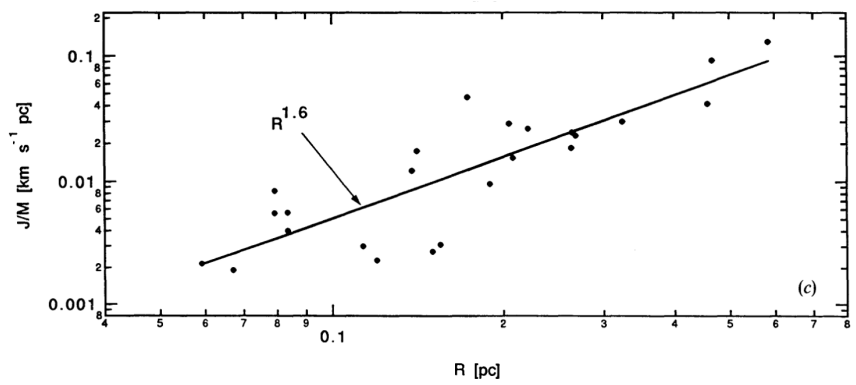

Figure 2.6.1: Specific angular momentum of molecular cloud cores observed by Goodman et al. (1993). The dots are observed cloud cores and the curve is comes from that $J/M \propto \Omega_0 R^2$, and, from fitting their observations, that $\Omega_0 \propto R^{-0.4}$. The specific angular momentum scales with radius as $\mathrm{R}^{1.6}$. Image credit: Goodman et al. (1993).

dots are the observed cloud cores. The curve comes from the relation $J/M \propto \Omega_0 R^2$ and from fitting their observations Goodman et al. (1993) found $\Omega_0 \propto R^{-0.4}$.

Burkert & Bodenheimer (2000) modelled turbulent molecular cloud cores and found that the specific angular momentum of cloud cores have an average value of

$$\frac{J}{M} = 7.0 \cdot 10^{20} \left(\frac{R}{0.1 \text{ pc}} \right)^{3/2} \text{ cm}^2 \text{ s}^{-1}, \tag{2.55}$$

but with a large spread. Similarly, (Goodman et al. 1993) found that the specific angular momentum scales as

$$\frac{J}{M} = 1.5 \cdot 10^{21} \left(\frac{R}{0.1 \text{ pc}} \right)^{1.6} \text{ cm}^2 \text{ s}^{-1}. \tag{2.56}$$

This results in a faster rotation rate than in Equation (2.55). Both of them already give high rotation rates. The J/M relation from (Burkert & Bodenheimer 2000) is used, since it results in a centrifugal radius which seems more reasonable at $\sim$ 280 au, rather than $\sim$ 1100 au, as the relation from van Dishoeck et al. (1993) does. Using Equation (2.55) and (2.54), the rotation rate of the cloud core can be found as

$$\Omega_0 = \frac{M}{I} \, 7.0 \cdot 10^{20} \left(\frac{R}{0.1 \text{ pc}} \right)^{3/2} \text{ cm}^2 \text{ s}^{-1}. \tag{2.57}$$

For a 1 $\mathrm{M}_\odot$ cloud core, with a 0.01 $\mathrm{M}_\odot$ protostar seed giving a total mass of 1.01 $\mathrm{M}_\odot$, modelled by Bonnor-Ebert sphere with a radius of 7.4 kpc, the rotation rate becomes

$$\Omega_{0,1M_\odot} = 6.07 \cdot 10^{-14} \text{ s}^{-1}. \tag{2.58}$$

Chapter 3

Method

In this chapter we will go though the numerical methods used in our model. We will describe how we find the Bonnor-Ebert sphere density profile and the discretization scheme we use in the model for the disk evolution and formation. The temperature structure of the disk is also explained. In the final section we test the code using a singular isothermal sphere and discuss how the Bonnor-Ebert sphere differs from the singular isothermal sphere. We also discuss some numerical issues that we find and how we solve some of them and why others are not a major problem.

3.1 Bonnor-Ebert sphere

3.1.1 Solving for the density profile

Solving for the density profile of an Bonnor-Ebert sphere is done numerically. We change variables from radius and density to the a-dimensional variables

$$x = \frac{r}{R_{\rm c}}, \tag{3.1}$$

$$y = \frac{\rho}{\rho_c}. \tag{3.2}$$

ρ_c is the central density and $R_{\rm c}$ is the characteristic radius of the sphere, given by

$$R_{\rm c} = \frac{c_{\rm s}}{\sqrt{4\pi G \rho_c}}. \tag{3.3}$$

If we then write $u = \ln y$, Equation (2.1) in terms of these a-dimensional variables is

$$\frac{1}{x^2}\frac{\mathrm{d}}{\mathrm{d}x}\left(x^2\frac{\mathrm{d}u}{\mathrm{d}x}\right) = -e^u, \tag{3.4}$$

with boundary conditions

$$u(0) = 0, \tag{3.5}$$

$$\frac{\mathrm{d}u}{\mathrm{d}x} = 0. \tag{3.6}$$

Equation (3.4) can be expressed as a system of two first order differential equations,

$$\frac{\mathrm{d}z}{\mathrm{d}x} = -x^2 e^u, \tag{3.7}$$

$$\frac{\mathrm{d}u}{\mathrm{d}x} = \frac{z}{x^2}. \tag{3.8}$$

The boundary conditions for these two equations are

$$z(0) = 0, \tag{3.9}$$

$$u(0) = 0. \tag{3.10}$$

This can then be solved with a standard ODE solver. A curve of the resulting density profile is shown in Figure 3.1.1.

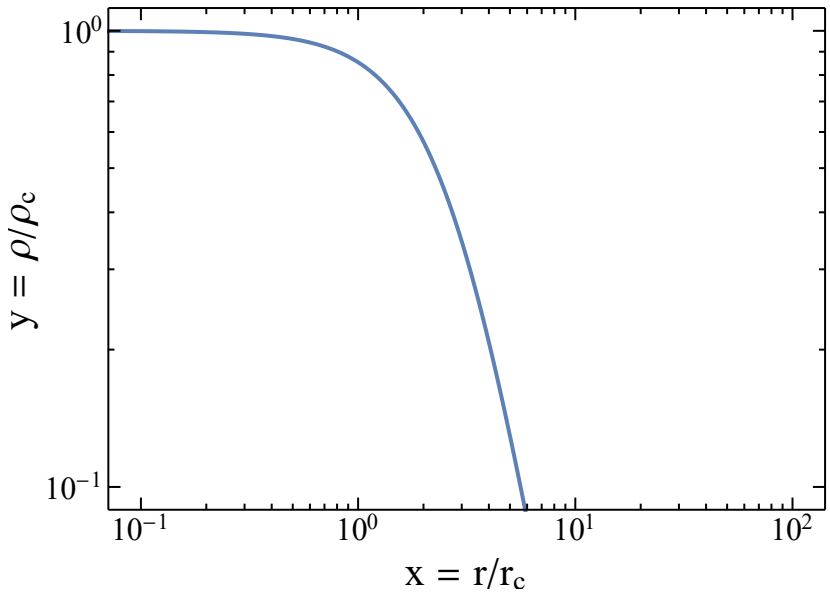

Figure 3.1.1: The blue curve shows the density profile of a Bonnor-Ebert sphere, in the a-dimensional quantities $x = r/R_\mathrm{c}$ and $y = \rho/\rho_c$.

3.1.2 Mass, radius and central density

For a Bonnor-Ebert sphere of mass M_BE, there exists a critical minimum radius for which the sphere is stable. If this radius shrinks, or the mass within increases, the sphere becomes

unstable and collapses. This radius is given by

$$R_{\rm BE} = \frac{G\ M_{\rm BE}}{2.42\ c_{\rm s}^2}. \tag{3.11}$$

This radius is also given by

$$R_{\rm BE} = \frac{x_{\rm crit}}{\sqrt{4\pi}} \frac{c_{\rm s}}{\sqrt{G\rho_{\rm c}}}. \tag{3.12}$$

$x_{\rm crit} = 6.5$ is the critical radius at which the Bonnor-Ebert sphere is stable towards collapse expressed in the dimensionless variable x. $\rho_{\rm c}$ is the central density of the sphere. From this one can solve for the central density as

$$\rho_{\rm c} = \frac{x_{\rm crit}^2}{4\pi} \frac{c_{\rm s}^2}{G} \frac{1}{R_{\rm BE}^2}. \tag{3.13}$$

To induce gravitational collapse of the Bonnor-Ebert sphere the mass of the sphere is increased by a factor $f > 1$. We select the desired final mass $M_{\rm BE}$, divide this by f. We then use this divided mass with Equation (3.11) to find the corresponding radius. With this radius we then use Equation (3.13) to find the central density of the sphere. To get the sphere back up to the desired mass we then increase the density by the factor f. The protostar is initialized with a seed with a mass that is 1/100 of the cloud core.

3.2 Gas surface density

The surface density evolution and equation takes the form of

$$\frac{\partial \Sigma_{\rm g}}{\partial t} = \frac{3}{r} \frac{\partial}{\partial r} \left[r^{1/2} \frac{\partial}{\partial r} \left(\nu \Sigma_{\rm g} r^{1/2} \right) \right] + \frac{\dot{M}_{\rm Infall}}{8\pi R_{\rm c}^2} \left(\frac{r}{R_{\rm c}} \right)^{-3/2} \left(1 - \left(\frac{r}{R_{\rm c}} \right)^{1/2} \right)^{-1/2}, \tag{3.14}$$

from combining Equation (2.44) and (2.33). In the first step of solving this equation, it is rewritten following the prescription by Bath & Pringle (1981). By making the substitution $X = 2r^{1/2}$ and $S = X\Sigma_{\rm g}$ Equation (3.14) can be rewritten as

$$\frac{\partial S}{\partial t} = \frac{12}{X^2} \frac{\partial^2}{\partial X^2} (S\nu) + \frac{X\dot{M}_{\rm Infall}}{8\pi R_{\rm c}^2} \left(\frac{X^2}{4R_{\rm c}} \right)^{-3/2} \left(1 - \left(\frac{X^2}{4R_{\rm c}} \right)^{1/2} \right)^{-1/2} \tag{3.15}$$

$$\Leftrightarrow \frac{X^2}{12} \frac{\partial S}{\partial t} = \frac{\partial^2}{\partial X^2} (S\nu) + \frac{\dot{M}_{\rm Infall} \left(\frac{X^2}{R_{\rm c}} \right)^{1/2}}{6\pi X \left(4 - 2 \left(\frac{X^2}{R_{\rm c}} \right)^{1/2} \right)^{1/2}} \tag{3.16}$$

This equation is solved numerically using a one-dimensional finite volume scheme. The integration domain is divided into N cells of equal logarithmic size. The centre of a cell is X_j, and the edges are $X_{j-1/2}$ and $X_{j+1/2}$, separated by the distance h_j. In the one-dimensional finite volume scheme, the value of a function in each cell is approximated by the average over the entire cell as follows:

$$\frac{X^2}{12}\frac{\partial S}{\partial t} \approx \frac{1}{h_j}\int_{X_{j-1/2}}^{X_{j+1/2}} \frac{X^2}{12}\frac{\partial S}{\partial t}\,\mathrm{d}X \tag{3.17}$$

$$= \frac{1}{h_j}\int_{X_{j-1/2}}^{X_{j+1/2}} \frac{\partial^2}{\partial X^2} S\nu\,\mathrm{d}X + \frac{1}{h_j}\int_{X_{j-1/2}}^{X_{j+1/2}} \frac{\dot{M}_{\mathrm{Infall}}\left(\frac{X^2}{R_\mathrm{c}}\right)^{1/2}}{6\pi X\left(4-2\left(\frac{X^2}{R_\mathrm{c}}\right)^{1/2}\right)^{1/2}}\,\mathrm{d}X \tag{3.18}$$

$$= \frac{1}{h_j}\left(\underbrace{\frac{\partial}{\partial X}S\nu|_{X_{j+1/2}}}_{=F(X_{j+1/2})} - \underbrace{\frac{\partial}{\partial X}S\nu|_{X_{j-1/2}}}_{=F(X_{j-1/2})}\right) + \frac{1}{h_j}\left[\frac{\dot{M}_{\mathrm{Infall}}}{6\pi}\left(4-2\left(\frac{X^2}{R_\mathrm{c}}\right)^{1/2}\right)^{1/2}\right]_{X_{j-1/2}}^{X_{j+1/2}} \tag{3.19}$$

$$= \frac{1}{h_j}\left(F(X_{j+1/2}) - F(X_{j-1/2})\right) + \frac{1}{h_j}\left[\frac{\dot{M}_{\mathrm{Infall}}}{6\pi}\left(4-2\left(\frac{X^2}{R_\mathrm{c}}\right)^{1/2}\right)^{1/2}\right]_{X_{j-1/2}}^{X_{j+1/2}} \tag{3.20}$$

$F(X_{j+1/2}) = \frac{\partial}{\partial X}S\nu|_{X_{j+1/2}}$ is defined as the flux over edge $X_{j+1/2}$. $F(X_{j+1/2})$ being the derivative of $S\nu$ with respect to X, is approximated by

$$F(X_{j+1/2}) = \frac{S\nu|_{X_{j+1}} - S\nu|_{X_j}}{h_i}. \tag{3.21}$$

h_i is the distance between the center of cell j and $j+1$. The evolution of S can then be written as

$$\frac{\partial S}{\partial t} = \frac{12}{X^2}\frac{1}{h_j}\left(F(X_{j-1/2}) - F(X_{j+1/2})\right) + \frac{12}{X^2}\frac{1}{h_j}\left[\frac{\dot{M}_{\mathrm{Infall}}}{6\pi}\left(4-2\left(\frac{X^2}{R_\mathrm{c}}\right)^{1/2}\right)^{1/2}\right]_{X_{j-1/2}}^{X_{j+1/2}}. \tag{3.22}$$

Substituting back Σ_g for S gives the final form of the surface density equation as

$$\frac{\partial \Sigma_{g,j}}{\partial t} = \frac{12}{X^3}\frac{1}{h_j}\left(F(X_{j-1/2}) - F(X_{j+1/2})\right) + \frac{12}{X^3}\frac{1}{h_j}\left[\frac{\dot{M}_{\text{Infall}}}{6\pi}\left(4 - 2\left(\frac{X^2}{R_c}\right)^{1/2}\right)^{1/2}\right]_{X_{j-1/2}}^{X_{j+1/2}}. \tag{3.23}$$

3.2.1 Boundary conditions

Outer boundary

The boundary condition at the outer edge is set up so that the surface density follows an exponential continuation of the two outer cells. That is, since the grid is logarithmic, the surface density between cell N and $N+1$ has the same ratio as that of cell $N-1$ and N. The surface density in the boundary cell is then given by

$$\Sigma_{g,N+1} = \frac{\Sigma_{g,N}}{\Sigma_{g,N-1}} \cdot \Sigma_{g,N}. \tag{3.24}$$

An exponential continuation of the surface density profile is used as the outer boundary condition because the solution to Equation (3.14) naturally leads to an exponentially decaying profile. This profile comes from an analytical solution to Equation (3.14), which can be found under certain conditions (Pringle 1981).

Inner boundary

At the inner edge of the disk, the boundary condition was set up so that the mass accretion through the inner boundary cell is the same as though cell 1. This is the mass that is accreted onto the star. All mass that leaves cell 1 through its inner edge, is accreted onto the star.

The mass accretion is given by

$$\dot{M} = \Sigma_g \cdot 3\pi\nu. \tag{3.25}$$

If $\dot{M}$ is the same for cell 0 and 1, this gives

$$\Sigma_{g,0} \cdot 3\pi\nu_0 = \Sigma_{g,1} \cdot 3\pi\nu_1 \tag{3.26}$$

$$\Rightarrow \Sigma_{g,0} = \Sigma_{g,1}\frac{\nu_1}{\nu_0} \tag{3.27}$$

3.3 Dust surface density

The dust surface density is modelled both by advecting the dust with the gas, and by letting it drift through the disk. To advect the dust it is treated as if it were perfectly coupled to the gas and evolved as a tracer of the gas. We define the dust surface density as $\epsilon\Sigma = \Sigma_{\rm g} \cdot \epsilon$, where ϵ is the dust-to-gas ratio and $\Sigma_{\rm g}$ the gas surface density. Following the method used for the gas evolution, the flux of dust over the cell edges is ϵ times the flux of gas, F, given by Equation (3.21). The dust flux is now

$$\epsilon F = \epsilon \cdot F. \tag{3.28}$$

The gas advection component of the dust evolution is then given by

$$\frac{\partial \epsilon\Sigma_{{\rm Adv},j}}{\partial t} = \frac{12}{X^3}\frac{1}{h_j}\left(\epsilon F(X_{j-1/2}) - \epsilon F(X_{j+1/2})\right). \tag{3.29}$$

The drift component of the dust evolution is solved from Equation (2.50) using an upwind scheme. The change in cell j is given by

$$\frac{\partial \epsilon\Sigma_{{\rm Drift},j}}{\partial t} = -\frac{1}{r_j}\frac{1}{\Delta r}\left(r_{j+1}\Sigma_{d,j+1}v_{r,j+1} - r_j\Sigma_{d,j}v_{r,j}\right) \tag{3.30}$$

Where $v_{\rm r}$ is given by Equation (2.45).

The complete dust evolution is then obtained by combining Equation (3.29) and (3.30) with the dust source term. The dust source term is taken as 1/100 of the gas source term, as this is roughly the dust-to-gas ratio of the interstellar medium (Goldsmith et al. 1997).

$$S_d = \frac{S_g}{100} \tag{3.31}$$

The complete dust evolution is now

$$\frac{\partial \epsilon\Sigma}{\partial t} = \frac{\partial \epsilon\Sigma_{{\rm Adv},j}}{\partial t} + \frac{\partial \epsilon\Sigma_{{\rm Drift},j}}{\partial t} + S_d \tag{3.32}$$

3.3.1 Dust boundary conditions

Outer dust boundary

The outer dust boundary is set up in the same way as for the gas, i.e. the exponential continuation. The surface density of the outer boundary cell, that is cell $N+1$, is then given by

$$\Sigma_{d,N+1} = \frac{\Sigma_{d,N}}{\Sigma_{d,N-1}} \cdot \Sigma_{d,N}. \tag{3.33}$$

As opposed to the gas surface density, this is not a natural effect of the solution to the surface density evolution equation. However, the dust disk is unlikely to extend all the way to the edge of the integration domain since the dust drifts inwards in the disk. The outer edge is therefore only affected by the initial, practically empty, disk that is created for numerical reasons, and this does follow an exponential decay.

Inner dust boundary

The inner boundary conditions is set up so that the mass accretion rate of dust is the same in the inner boundary cell and cell 1. This mass accretion rate is given by

$$\dot{M}_d 2\pi r \Sigma v_{\mathrm{r}}. \tag{3.34}$$

If we equate these for the inner boundary cell and cell one we get

$$2\pi r_0 \Sigma_{d,0} v_{r,0} = 2\pi r_1 \Sigma_{d,1} v_{r,1} \tag{3.35}$$

$$\Rightarrow \Sigma_{d,0} = \frac{r_1}{r_0} \Sigma_{d,1} \frac{v_{r,1}}{v_{r,0}}. \tag{3.36}$$

3.4 Temperature structure

The disk is set up as an isothermal disk following the MMSN prescription of Hayashi (1981). In this model the disk is assumed to be optically thin, and the only heating source is radiation from the star. The temperature is then given by a balance of incoming and outgoing radiation. The resulting temperature profile is given by

$$T = \begin{cases} 280 \left(\dfrac{L_\star}{L_\odot} \right)^{1/4} r^{-1/2} \text{ K}, & \text{if } T > 10 \text{ K} \\ 10 \text{ K}, & \text{else} \end{cases} \tag{3.37}$$

$L_\star$ is the luminosity of the star. This is approximated with the luminosity of an equivalent main sequence star through the relation

$$\frac{L_\star}{L_\odot} = \left(\frac{M_\star}{M_\odot} \right)^4, \tag{3.38}$$

(Duric 2004), which approximately holds in the mass range 0.5 $\mathrm{M}_\odot \lesssim M \lesssim$ 2.0 $\mathrm{M}_\odot$ that is investigated in this project. From the temperature, the sound speed, c_{s}, is calculated from

$$c_{\mathrm{s}}^2 = \frac{kT}{\mu m_{\mathrm{h}}}, \tag{3.39}$$

where k is the Boltzmann constant, $m_{\rm h}$ the mass of a hydrogen atom and $\mu = 2.34$ is the mean molecular weight (Hayashi 1981). Note that this is a crude approximation for an forming and evolving disk. The real temperature structure will be a balance of external radiation, both from the central star and external stars, viscous heating, heating due to infalling material and the energy that the disk radiates away.

3.5 Code testing

3.5.1 Singular isothermal sphere tests

This test were performed for the singular isothermal sphere approximation of the Bonnor-Ebert sphere. In this case the mass infall rate is constant (Shu 1977) and given by Equation (2.22). The disk α value was $\alpha = 10^{-2}$,the angular frequency of the cloud core was $\Omega_0 = 10^{-4}$, and the temperature of the cloud core was $T_{\rm cd} = 10$ K. The disk was also assumed to be isothermal, with the temperature structure given by Equation (3.37). These tests were performed partially as a test of the core, and partially to better understand how a singular isothermal sphere differs from a Bonner-Ebert sphere.

In this test we vary the seed and cloud masses, but keep the sum of the two constant. We ran two cases, one with a seed mass of 0.1 $M_\odot$ and a cloud mass of 1.0 $M_\odot$, and second with a seed and cloud mass of 0.4 $M_\odot$ and 0.7 $M_\odot$ respectively. Each case simulated $5 \cdot 10^6$ yr of disk evolution.

The surface density profile after $5 \cdot 10^6$ yr of both cases is shown in Figure 3.5.1. Both cases have an almost identical final state. From this it appears that it is the total mass of the system that matters for the final state. How it is distributed between the seed and cloud matters less for the final surface density.

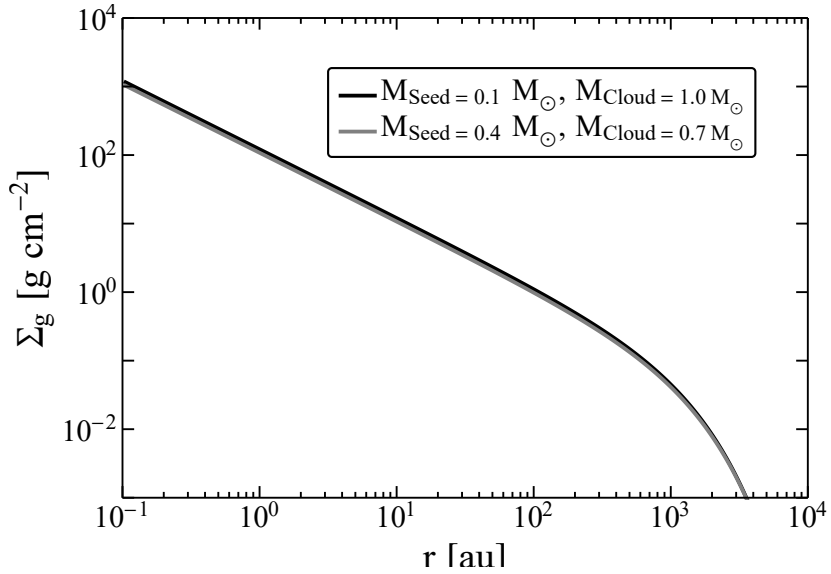

Figure 3.5.1: The final gas surface density after $5 \cdot 10^6$ yr. The two cases have the same total seed plus cloud mass, but different individual masses of the seeds and clouds. The final surface density differs very little for the two cases.

The initial distribution of mass in the seed and cloud is not without consequence. Figure 3.5.2 shows the accretion rate onto the star from the disk as a function of time. One can see that the lower mass seed case has a higher accretion rate through the entire simulation. There are also two clear regimes in the accretion rate. At first, the accretion rate is nearly constant with time, and after some point it shows a power law shape. The change between the two regimes happens when the cloud collapsing onto the disk has been emptied of material. That is, as long as material keeps falling on to the disk, the accretion rate onto the star remains relatively constant. After this the accretion rate drops as the surface density of the disk decreases.

Figure 3.5.3 shows the disk and stellar mass over the $5 \cdot 10^6$ yr period for the same cases. The dashed lines are the disk masses, and the solid lines represent the stellar masses. The disks grow in mass at a different pace, with the higher mass seed case growing faster, but they reach very similar maximum masses. The situation is much the same for the stellar masses. The high seed mass case has a faster evolution than the low seed mass case. Starting with a more massive seed, and less massive cloud, is similar to starting at a later time.

3.5.2 Comparing the BE-sphere and the SIS

A comparison of the disk mass infall rate for the collapsing BE-sphere and the collapsing singular isothermal sphere (SIS) is shown in Figure 3.5.4. The collapsing BE-sphere with a

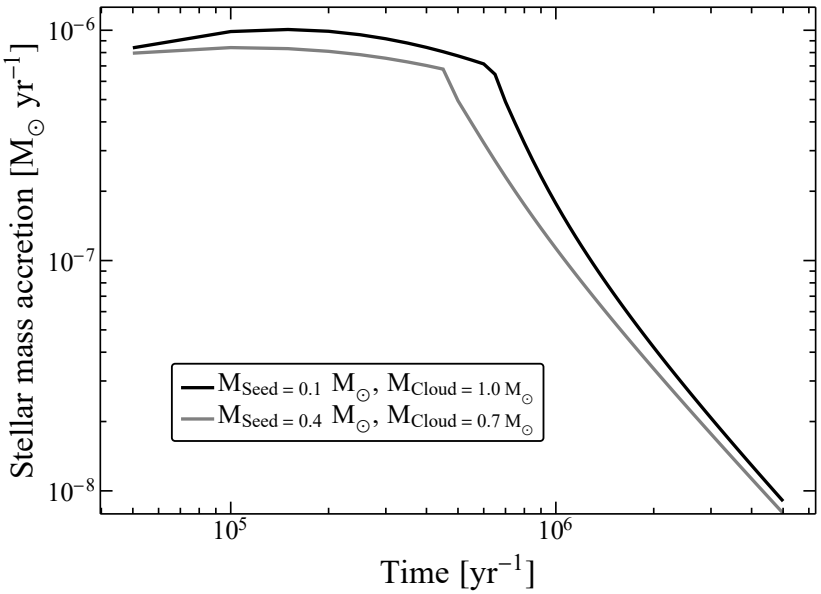

Figure 3.5.2: Accretion rate onto the star from the disk over a $5 \cdot 10^6$ yr period. The initially lower mass seed (black curve) accretes at a higher rate at all times. This is likely due to the higher viscosity caused by the lower mass seed.

mass of 1 $M_\odot$ and a temperature of 10 K. One can see that the disk fed by the BE-sphere initially accretes roughly $\sim$ 2 order of magnitude slower, but after $\sim 8 \cdot 10^4$ yr ($\sim$ 1/3 of the collapse phase time of the BE-sphere) it overtakes the singular isothermal sphere. Note that in the SIS the disk needs to accrete for a bit more than 3 times longer than the BE-sphere to accrete 1 $M_\odot$.

3.5.3 Mass loss

While testing the effects of varying the seed and cloud mass, we noticed an issue where the final mass of the star and disk did not add up to the total mass of the seed and the cloud. Investigating this loss of mass, we found that the total mass added per unit time by the source term was lower than the mass infall rate, $\dot{M}$. This issue was present also with the time dependent mass infall rate. Figure 3.5.5 shows the accretion rate, both from the expected $\dot{M}$ that is calculated from the shell collapse, and what the actual infall rate from the source term is. Figure 3.5.5 also illustrates that the source term appears to be quite numerically unstable. Sometimes the accretion rate is too high, and sometimes too low. The source of this is that the simulated grid only extends from 0.1 au outwards. Any material that would fall onto the disk within 0.1 au was not captured. To confirm that this was the case we set up an additional grid, extending from 10^{-7} au to 0.1 au. In this grid material was added from the source term, but not viscously evolved. The sum of the infall rate onto this inner grid, and the main outer grid indeed adds up to the mass infall

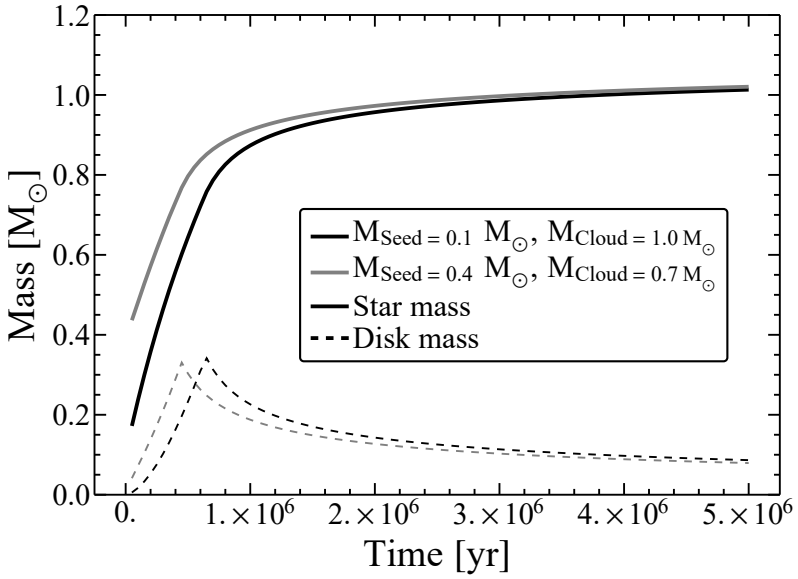

Figure 3.5.3: Disk (dashed curves) and stellar (solid curves) masses over the $5 \cdot 10^6$ yr period for the case of a 0.4 $M_\odot$ seed with a 0.7 $M_\odot$ cloud and a 0.1 $M_\odot$ seed with a 1.0 $M_\odot$ cloud. One can see that the two cases reach similar final stellar masses and have a similar maximum disk mass. The higher seed mass case (gray curve) evolves faster than the low seed mass case (black curve).

rate $\dot{M}$, confirming the suspicion that the missing inner part of the disk was the source of the mass loss.

This could be fixed by extending the grid inwards, but this becomes computationally expensive and therefore undesirable. Also, protoplanetary disks are not expected to extend all the way to the star, as magnetic fields from the star will transport material away from the disk onto the star. This inner edge of the disk is believed to be at ~ 0.1 au (Hartmann et al. 2016). Instead, we set up an inner grid extending out to 0.1 au. We calculate how much mass would land on this inner grid, and add it to the star. This is justified since any material drifting through the inner edge of the main grid is treated as being accreted onto the star. Any material landing inside it should therefore also be accreted by the star. Figures 3.5.5 shows the infall rate onto this inner disk, as well as the outer disk and the sum of the two, over $5 \cdot 10^6$ yr. The sum is generally closer to the expected value. Figure 3.5.6 shows the total mass of the system over $5 \cdot 10^6$ yr. The blue curve is the expected mass, and the dashed red the actual mass. The two match very well, confirming that the inner grid fixed the mass loss issue.

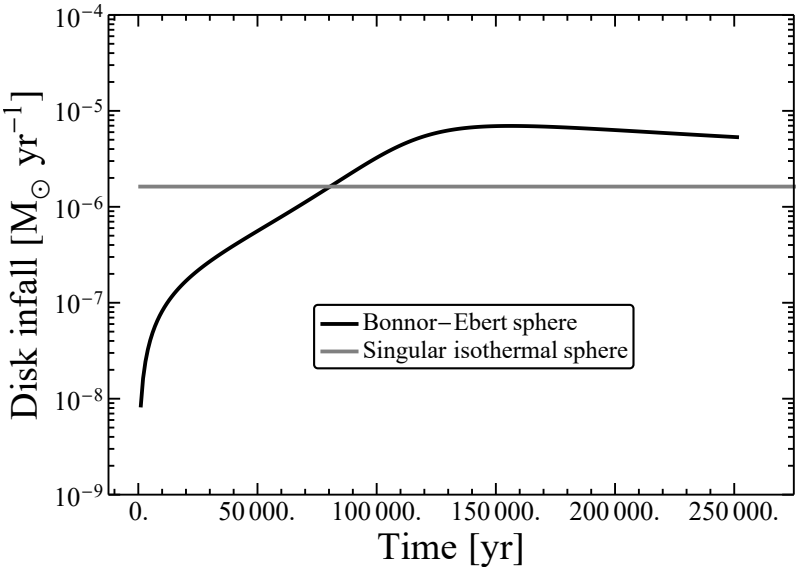

Figure 3.5.4: Comparison of the disk mass infall rate for a 1 $M_\odot$ Bonnor-Ebert sphere (black curve) and the singular isothermal sphere (grey curve). The disk in the singular isothermal sphere accretes at a constant rate, set by the temperature of the cloud. During the initial stages of the collapse the Bonnor-Ebert solution accretes ~ 2 orders of magnitude slower, increasing with time. At $\sim 8 \cdot 10^4$ yr it overtakes the singular isothermal sphere and accretes roughly and order of magnitude faster for the remainder of the collapse.

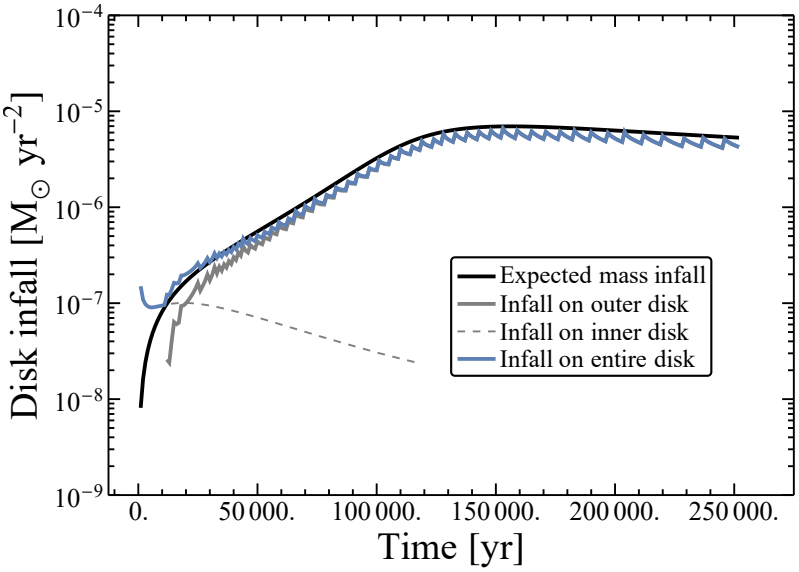

Figure 3.5.5: What the mass accretion onto the disk should be (black), and what is actually added through the numerical procedure. The mass infall rate onto the disk is sometimes underestimated, and sometimes overestimated. This suggests that it is numerically unstable. Still, the total mass which lands on the disk+star is consistent with what is expected, see Figure 3.5.6.

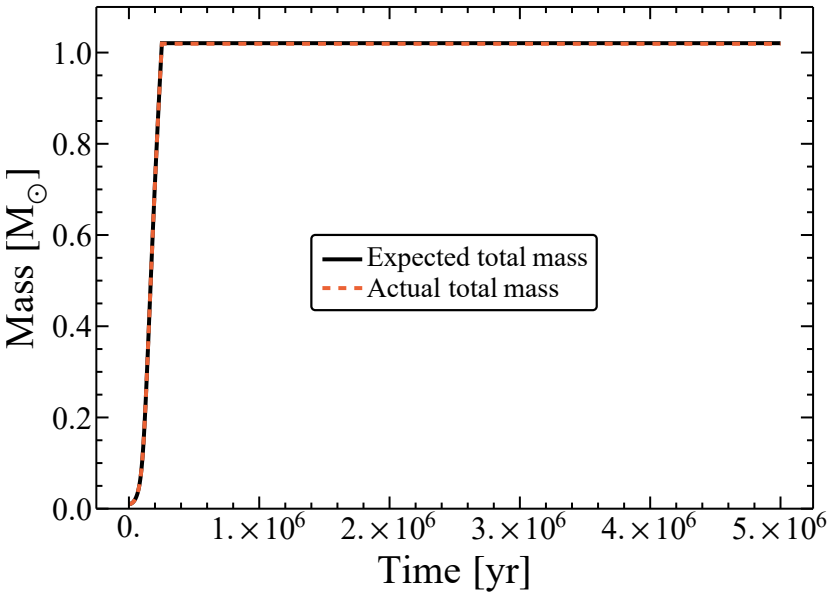

Figure 3.5.6: Expected total mass (black) and actual total mass (dashed orange) of the disk and star system. The two masses are almost identical throughout the simulation of $5 \cdot 10^6$ yr, even though the accretion rate shows some instability, see Figure 3.5.5.

Chapter 4

Results

This chapter will present the results of our numerical simulations. In section 4.1 we will go through a reference simulation of a 1 $M_\odot$ collapsing to form a disk and star. We will examine how both the gas and dust disk forms and evolves, and analyse some of the properties of the disk. This is done to give us a general understanding of the disk so that we can compare it to simulations with different initial conditions. After we have looked at the reference case we move on to Section 4.2 where we make a parameter space study of the dust size and the initial conditions of the cloud core. We will begin by investigating the effect of increasing and decreasing the dust size on the evolution of the dust disk. We will then move on to how the angular momentum of the cloud core affects the gas and dust disk formation and evolution. We do this by changing the rotation rate and mass of the cloud core.

4.1 Reference simulation

In this section we present the results of simulating a reference case, named `refrun`. In Section 4.2 we will explore the dependency on various model parameters. This simulation of the formation of the protoplanetary disk through the collapse of a Bonnor-Ebert sphere, and subsequent evolution, was made with the cloud and disk parameters shown in Table 4.1. The molecular cloud core is assumed to be isothermal and have a temperature of 10 K (van Dishoeck et al. 1993). The evolution of the protoplanetary disk was simulated for $5 \cdot 10^6$ yr.

Table 4.1: Disk and cloud parameters used in all the cases explored. Note that the $R_{\texttt{c,Max}} = 1$ au case was only used to further explore the parameter range in Figure 4.2.9.

Run	$M_{\rm BE}$	Ω_0 [s^{-1}]	$T_{\rm cd}$ [K]	$\alpha_{\rm m}$	$R_{\rm c,Max}$ [au]	Dust size [cm]
`refrun`	1.0	$6.07 \cdot 10^{-14}$	10	0.01	276.6	0.01
$R_{\texttt{c,Max}} = 1$ au	1.0	$3.65 \cdot 10^{-15}$	10	0.01	1.0	0.01
`Low-`Ω_0	1.0	$6.07 \cdot 10^{-15}$	10	0.01	2.8	0.01
$R_{\texttt{c,Max}} = 50$ au	1.0	$2.58 \cdot 10^{-14}$	10	0.01	50.0	0.01
`Low-mass`	0.5	$8.55 \cdot 10^{-14}$	10	0.01	69.5	0.01
`High-mass`	2.0	$4.27 \cdot 10^{-14}$	10	0.01	1111.7	0.01
`Large-dust`	1.0	$6.07 \cdot 10^{-14}$	10	0.01	276.6	0.1
`Small-dust`	1.0	$6.07 \cdot 10^{-14}$	10	0.01	276.6	0.001

4.1.1 The gas disk

The rate at which material falls onto the disk during the formation phase varies with time. This can be seen in Figure 4.1.1, which shows the disk mass infall rate as a function of time. The entire formation phase last $\sim 2.5 \cdot 10^5$ yr, and during this time the infall rate varies by several orders of magnitude. During the first half of the formation phase the infall rate increases from $\sim 10^{-8}$ M$_\odot$ yr^{-1} to $\sim 10^{-5}$ M$_\odot$ yr^{-1}. After this initial phase, the infall rate remains almost constant for the remainder of the formation phase.

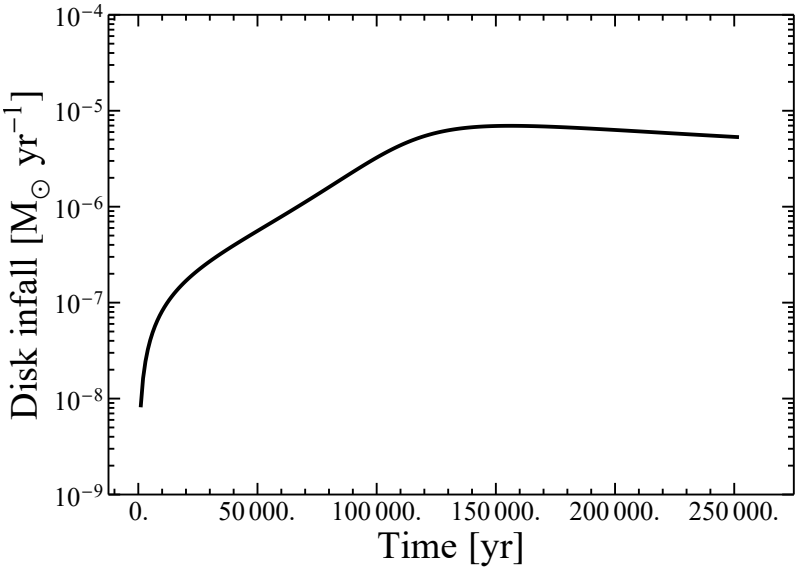

Figure 4.1.1: Infall rate of gas onto the disk during the formation phase of the `refrun`. During the first $1.25 \cdot 10^5$ yr the infall rate grows to a peak value of $\sim 10^{-5}$ M$_\odot$ yr^{-1}. For the remaining time of the formation phase the disk accretes mass at a high rate of almost $\sim 10^{-5}$ M$_\odot$ yr^{-1}.

Figure 4.1.2 shows the gas surface density at a number of snap shots in time, lighter coloured lines show earlier times. The dashed black line shows the final centrifugal radius. The first snap shot shows the disk after $5 \cdot 10^4$ yr. This is during the first half of the formation phase of the disk. The disk has started to build up in the inner parts ($\lesssim 3$ au), while simultaneously evolving viscously. At this point the viscous evolution of the disk is quite prominent. An explanation for this disk profile can be found in the infall rate onto the disk. At $5 \cdot 10^4$ yr the infall rate onto the disk is quite low, therefore, viscous evolution should be the dominant process determining the shape of the surface density profile. The formation phase ends at $\sim 2.5 \cdot 10^5$ yr. At this time, the outer regions of the disk become Toomre unstable, causing the viscosity parameter α to increase as described in Section 2.4. In this region gas will therefore be transported away more efficiently. One can see this in the profile of surface density. The outer parts of the disk have a steeper slope than the inner parts. The disk also has a sharper outer edge than at other times. Figure 4.1.3 shows the Toomre Q value at the same snap shots in time as the gas surface density plot. At the end of the formation phase the Toomre Q is $Q \sim 1.2$ at radii > 3 au, showing that it is gravitationally unstable at this time. Mild Toomre instability is present within the final centrifugal radius up to $\sim 7 \cdot 10^5$ yr. However, shortly after the formation phase is over α_{m} dominates over α_Q. The dashed lines show Q for a model where α is not allowed to increase as $\exp\left[-Q^4\right]$. Since α remains lower, the disk is not drained as quickly, allowing the surface density to become higher. Therefore Q becomes lower.

After this the disk only evolves viscously. One can see how this evolution proceeds in Figure 4.1.2. The inner disk is drained by gas being accreted onto the star and the outer disk grows by the simultaneous outward transport of gas in order to conserve angular momentum.

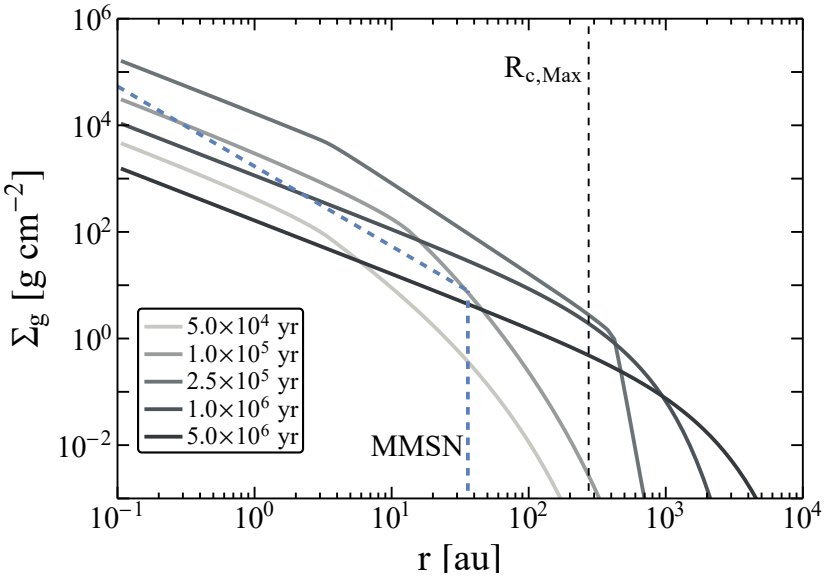

Figure 4.1.2: Surface density of the gas disk at different snap shots in time of the `refrun`. The dashed black line shows the final centrifugal radius and the dashed blue line shows the minimum mass solar nebula model of Hayashi (1981). One can see how the disk builds up during the formation phase. During most of this phase the infall onto the disk is the dominant factor determining the profile of the disk. After the formation phase the disk takes on the shape of a viscously evolving disk.

The dashed blue line in Figure 4.1.2 shows the profile of the minimum mass solar nebula model of Hayashi (1981). The similarities between the MMSN and the `refrun` are limited. At 10^5 yr the two disks does have similar gas surface densities at the edge of the MMSN disk, but other than that the similarities are lacking. There is a difference in the slope of the profile. The MMSN has a -3/2 slope in the gas surface density, whereas we find a disk that eventually settles into a slope closer to -1, as ones expects from a viscously evolving disk. The gas disk we find also extends significantly further out than the MMSN disk at all times.

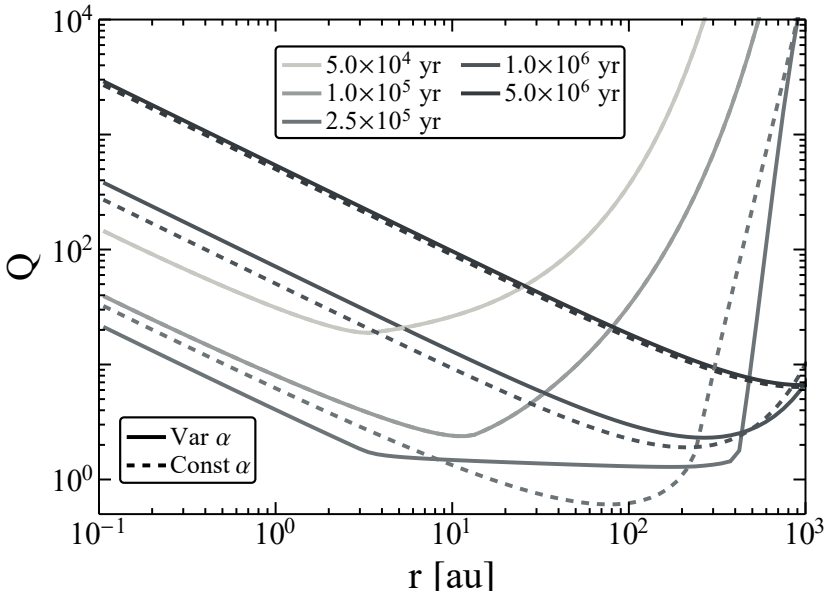

Figure 4.1.3: Toomre Q value at different snap shots of the `refrun`. The solid lines shows the Q value when α is allowed to change as describes in Section 2.4. At the late stages of the formation phase the Q value drops below 2, as can be seen in the $2.5 \cdot 10^5$ yr curve, showing that the disk is becoming gravitationally unstable. Comparing the dashed and solid curves, one can see how the prescription for increasing α with decreasing Q prevents Q from becoming very low.

We now consider the evolution of the total mass budget of the disk. During the formation phase ($\lesssim 2.5 \cdot 10^5$ yr) the stellar mass accretion rate grows with the increasing disk mass until the collapse is finished. This can be seen in Figure 4.1.4, where the accretion rate onto the star (black curve) and onto the disk (grey curve) is plotted versus the disk mass. The behaviour of the stellar accretion rate closely mimics that of the disk infall rate. The stellar mass accretion rate depends on the surface density and the viscosity. As the star grows in mass the viscosity drops as

$$\nu \propto \Omega_{\rm k}^{-1} = \left(\sqrt{\frac{M_{\rm star}\, G}{a^3}} \right)^{-1} \tag{4.1}$$

which gives a change of about 1 order of magnitude over the $5 \cdot 10^6$ yr simulation. But, the surface density, and thus the disk mass, grows due to the infall of gas onto the disk. This balance between decreasing viscosity and increasing surface density causes the growth of the accretion rate to slow down and eventually turn in to a decrease. Once the formation phase is over, the infall from the cloud core no longer replenishes the gas which is accreted onto the star. The disk mass then decreases, which results in a lower surface density and a drop in the accretion rate. We also find that at times $> 5 \cdot 10^5$ yr after the end of the formation phase the accretion rate onto the star scales with time as $\dot{M}_{\rm accrete} \propto t^{-\xi}$ where $\xi = 1.2$ in the `refrun` case.

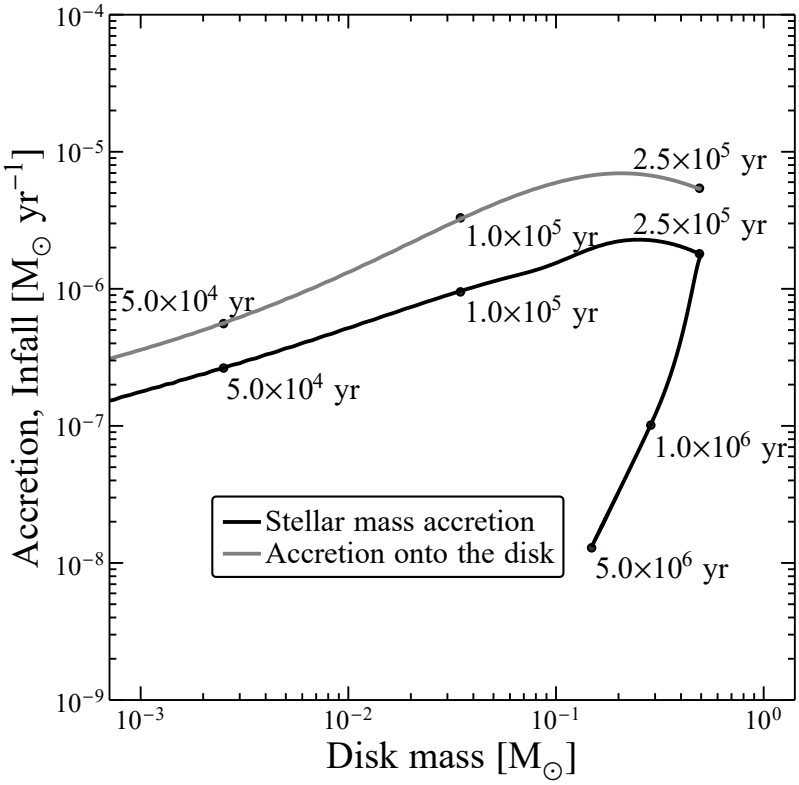

Figure 4.1.4: Stellar mass accretion rate and disk infall rate as a function of the disk mass in the `refrun`. In the first 10^5 yr the stellar mass accretion rate grows quickly as the disk begins to form close to the star. The stellar accretion rate profile mimics that of the disk infall rate closely. Once the formation phase is over at $2.5 \cdot 10^5$ yr, the stellar accretion rate drops steadily with the decreasing disk mass.

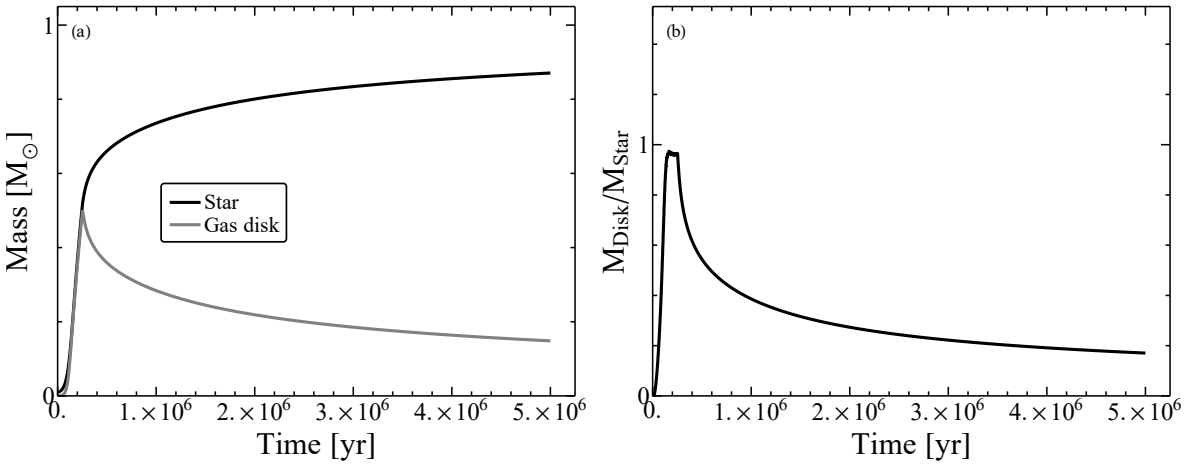

Figure 4.1.5: The left figure shows the mass of the star (black curve) and the disk (grey curve), and the right figure shows the ratio of the disk and star mass. During the formation phase ($\lesssim 2.5 \cdot 10^5$ yr), the gas disk mass grows faster than the stellar mass. The mass ratio reaches peaks at the end of the formation phase with a value of $M_{\rm Disk}/M_{\rm Star} = 0.97$. The disk then drops in mass as the infall has stopped and the star accretes gas from the disk. At the end of the $5 \cdot 10^6$ yr period the disk mass is still significant, with a mass ratio of 0.17.

Panel (a) in Figure 4.1.5 shows the star and disk mass as a function of time, and panel (b) shows the ratio of the disk and star mass. In the first $1.5 \cdot 10^5$ yr, the ratio of the masses increase quickly as the disk grows faster than the star. After $1.5 \cdot 10^5$ yr the disk and star have similar masses, giving a ratio that is ~ 0.95. Once here, the disk no longer outgrows the star and the ratio remains nearly constant until the end of the formation phase, where the disk starts to be drained. This peak coincides with the disk becoming gravitationally unstable. This increases the viscosity, thus driving up the stellar accretion rate, causing the star to grow faster. At the end of the $5 \cdot 10^6$ yr period, the mass ratio is $M_{\rm Disk}/M_{\rm Star} = 0.17$.

Looking at the state of the disk in the `refrun` at the end of the $5 \cdot 10^6$ yr simulation, this disk remains very massive and has a high accretion rate. The final mass of the disk is 0.15 $M_\odot$ and the accretion rate is $1.3 \cdot 10^{-8}$ $M_\odot$ yr^1. Generally, one expect disk masses to be no more than 0.1 $M_\odot$ at any time of the disk evolution (Ansdell et al. 2016; Bergin et al. 2013; McClure et al. 2016; Miotello et al. 2017; Pascucci et al. 2016). Accreting the whole disk in $5 \cdot 10^6$ yr appears to be difficult for such a large centrifugal radius. The maximum disk mass is also very high, nearly the same as the stellar mass. This also makes the approximation that the angular momentum at some radius in the disk is simply given by the Keplerian angular momentum provided by the star less accurate, since the disk itself can exert a significant gravitational pull.

After a few million yr of evolution, one also expects photoevaporation to begin to dissipate

the disk. But photoevaporation typically starts at a rate of $\sim 10^{-9}$ $M_\odot$ yr^{-1} (Owen et al. 2011), which is still an order of magnitude lower than the end state accretion through the disk of the `refrun`. This seems to show that the centrifugal radius in the `refrun` is too large, since both disk mass and accretion rate are tied to it, and remain high at the end of the $5 \cdot 10^6$ yr simulation. In Section 4.2 we will run the simulations with different parameters to see how the disk evolution depends on the initial conditions, and what is needed to end up with a disk which is more in line with expectations.

4.1.2 The dust disk

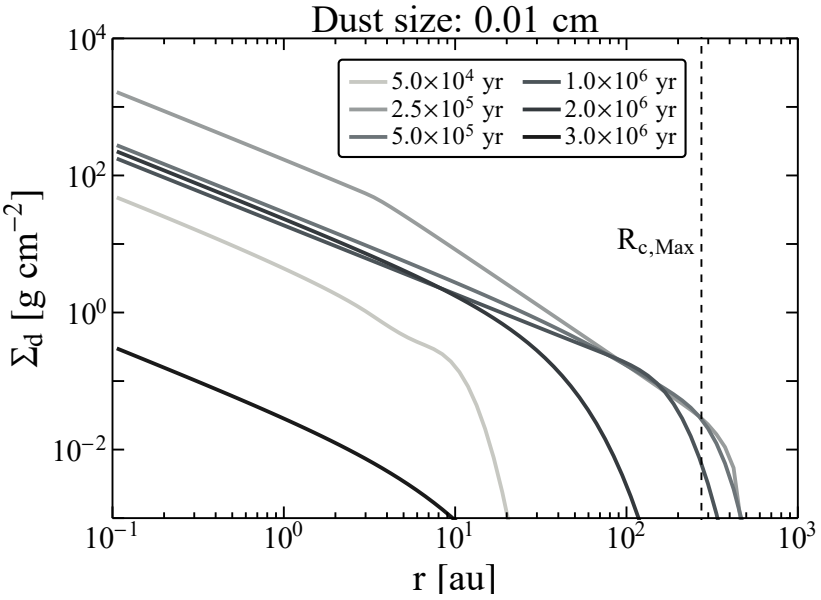

Figure 4.1.6: Surface density of dust at different snap shots in time of the `refrun`. After the formation phase is over, some dust is transported with the gas outwards past the centrifugal radius ($2.5 \cdot 10^5$ yr curve). As the dust drifts inwards, this outer dust acts as a reservoir which feeds the inner disk. This causes the surface density of dust in the inner disk to have a very slow decrease as long as the reservoir is able to feed it. This can be seen in the small change between the $5 \cdot 10^5$ yr curve and the $2 \cdot 10^6$ yr curve. Once the outer reservoir is empty, the disk begins so drain quickly, as the $3 \cdot 10^6$ yr curve shows.

In this section we examine how the dust disk evolves. The dust used here is of a constant size $r_d = 0.01$ cm. Note that it is unlikely that dust would remain at a constant size for the lifetime of the dust. It is generally believed to initially be μm in size. Quickly though, the dust will grow to mm-cm size, before the growth stops due to the fragmentation/bouncing barrier (Blum & Wurm 2000, 2008; Blum et al. 1998; Poppe et al. 1999; Zsom et al. 2010). More complete codes taking the coagulation and drift of dust into account have been made by e.g. Birnstiel et al. (2010); Brauer et al. (2008). Observations of class I protostars also show that the dust might grow to mm size already in the envelope surrounding the forming star and disk (Miotello et al. 2014). The 0.01 cm dust size adopted here is a compromise between the unknown initial and final limiting sizes, since we do not model dust coagulation. In Section 4.2.1 we will explore the effect of using different dust sizes.

The evolution of the dust surface density is shown in Figure 4.1.6. The snap shot shows the dust disk during the early part of the formation phase. Here, one can see how the dust builds up in the innermost part ($\lesssim 3$ au). Outside of this the dust has flowed outwards by being coupled with the viscously evolving gas. The disk continues to build up during the rest of the formation phase. Once the formation phase is over, the dust keeps evolving

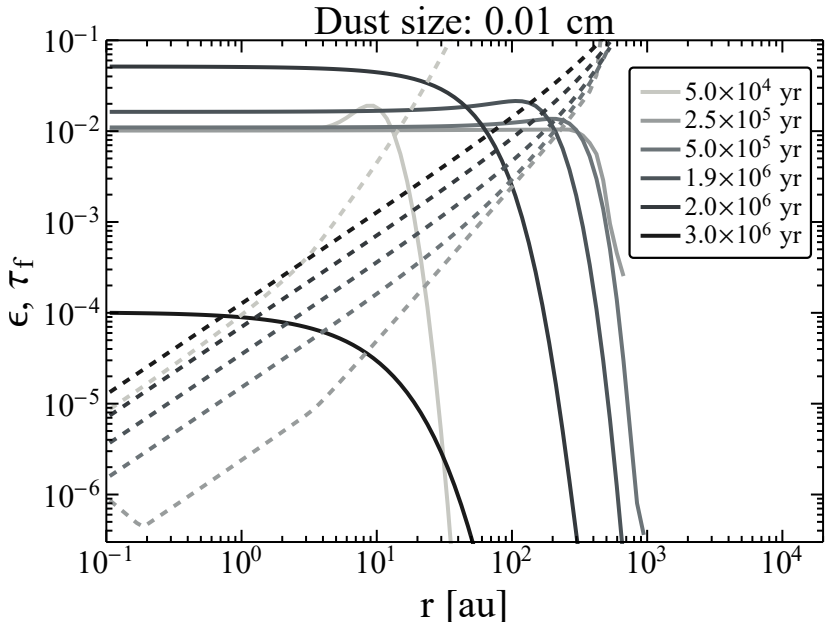

Figure 4.1.7: Dust to gas ratio (solid curves) at different snap shots in time of the `refrun`. For this size of dust, the dust-to-gas ratio peaks at $1.9 \cdot 10^6$ yr with a value of $\epsilon = 0.051$. The dashed lines show the Stokes number of the particles. In the regions where the dust-to-gas ratio is not insignificantly small, the Stokes numbers are very low and decreasing inwards due to the increasing gas surface density. At the $2.5 \cdot 10^5$ yr mark, one can see that in the innermost parts of the disk, the dust enters the Stokes drag regime. The Stokes number then goes up with decreasing disk radius.

as described in Section 3.3. Notable here is the change between the $5 \cdot 10^5$, $1 \cdot 10^6$, and $2 \cdot 10^6$ yr. Between the $5 \cdot 10^5$ and $1 \cdot 10^6$ yr, the surface density drops in the inner disk, as the dust in this region drifts inwards. But, between $1 \cdot 10^6$ and $2 \cdot 10^6$ yr, the surface density again increases. This happens because while dust is drained from the inner disk, the outer disk has received enough dust from the viscous evolution that it is able to later replenish the inner parts with drifting pebbles. In the outer part of the disk this can be clearly seen. At $2 \cdot 10^6$ yr the outer disk is being drained, but the inner disk is increasing in gas in surface density from this gas draining from the outer disk. After the outer reservoir of dust has been depleted, the remaining dust disk depletes quickly. From $2 \cdot 10^6$ to $3 \cdot 10^6$ yr the surface density has dropped more than two orders of magnitude.

The evolution of the dust-to-gas ratio, ϵ, is perhaps more interesting than the evolution of the dust itself. This can be seen in Figure 4.1.7. Initially, the dust-to-gas ratio is 1/100, which is the ratio between the dust and gas source terms. The dust-to-gas ratio changes very little during the first 10^6 yr. During this phase Stokes numbers are very small, and the dust almost completely coupled to the gas. Viscous evolution of the dust dominates over the drift, causing the dust to follow the gas very closely. This causes the dust-to-gas ratio to remain very close to 1/100. However, once the dust disk goes into the phase of being

drift dominated the outer disk replenishes the inner disk, and the dust-to-gas ratio begins to increase. It reaches a maximum value of $\epsilon = 0.051$ at $1.9 \cdot 10^6$ yr. This behaviour occurs because while the inner gas disk is drained by the accreting star, it has no outer reservoir which replenishes it at the same rate as the dust has. Therefore, the gas surface density drops faster than the dust surface density. This causes the dust-to-gas ratio to increase during this period. Once the outer disk has been depleted of dust, the dust surface density drops quickly as the dust drift drains the inner disk. The dust-to-gas ratio then also drops quickly, as can be seen in the $3 \cdot 10^6$ yr curve of Figure 4.1.7. Since the gas disk remains significant until the end of the $5 \cdot 10^6$ yr period simulated, the dust disk lifetime is shorter than the gas disk lifetime by at least $2 \cdot 10^6$ yr.

If the dust-to-gas ratio is sufficiently high, coupled with large enough Stokes numbers, the protoplanetary disk can be come streaming instability active. For a given Stokes number, there is a critical dust-to-gas ratio, ϵ_c, for which the streaming instability becomes active. This is given by Equation (4.2) (Yang et al. 2017).

$$\log(\epsilon_c) = 0.10\,(\log(\tau_f))^2 + 0.20\log(\tau_f) - 1.76 \qquad (\tau_f < 0.1), \tag{4.2}$$

This gives the condition that the streaming instability can be active if

$$\frac{\epsilon}{\epsilon_c} > 1. \tag{4.3}$$

In the `refrun`, the streaming instability is active in the very early phases of the disk, beginning at $1.5 \cdot 10^4$ yr at an orbital radius of ~ 1 au. The streaming instability region remains active for another $1.5 \cdot 10^4$ yr, moving out to ~ 4.2 au at the end of this phase. This can be seen in Figure 4.1.8, which show contour plots of dust-to-gas ratio and the critical dust-to-gas ratio over time and disk radius. At $8.6 \cdot 10^5$ yr, the disk becomes streaming instability active again, this time at an orbital radius of ~ 150 au. The streaming instability remains active in the disk until a time of $\sim 1.95 \cdot 10^6$ yr. Over this period, the region in which it is active expands and moves through the disk.

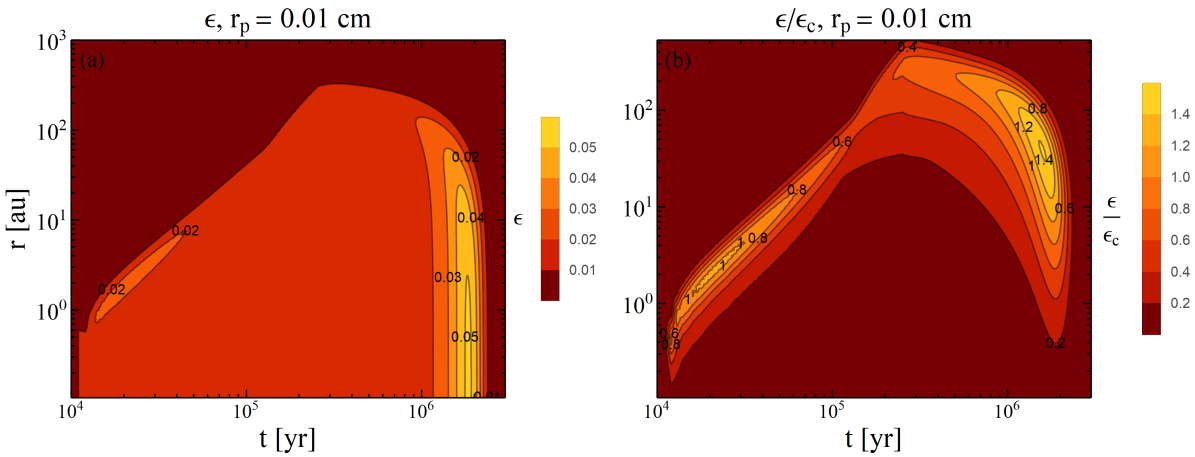

Figure 4.1.8: Contour plots of the dust-to-gas ratio (panel a) and the ratio between the dust-to-gas ratio and the critical dust-to-gas ratio needed for the streaming instability to becomes active (panel b). The dust-to-gas ratio increases at times between 10^6 and $2 \cdot 10^6$ yr in the inner parts of the disk, reaching its maximum in the innermost parts. In panel b one can see that the streaming instability condition is reached at very early times in the disk at a radius of a few au, and between 10^6 and $2 \cdot 10^6$ yr at orbits of 10-150 au.

4.2 Exploring parameter space

4.2.1 Dust size

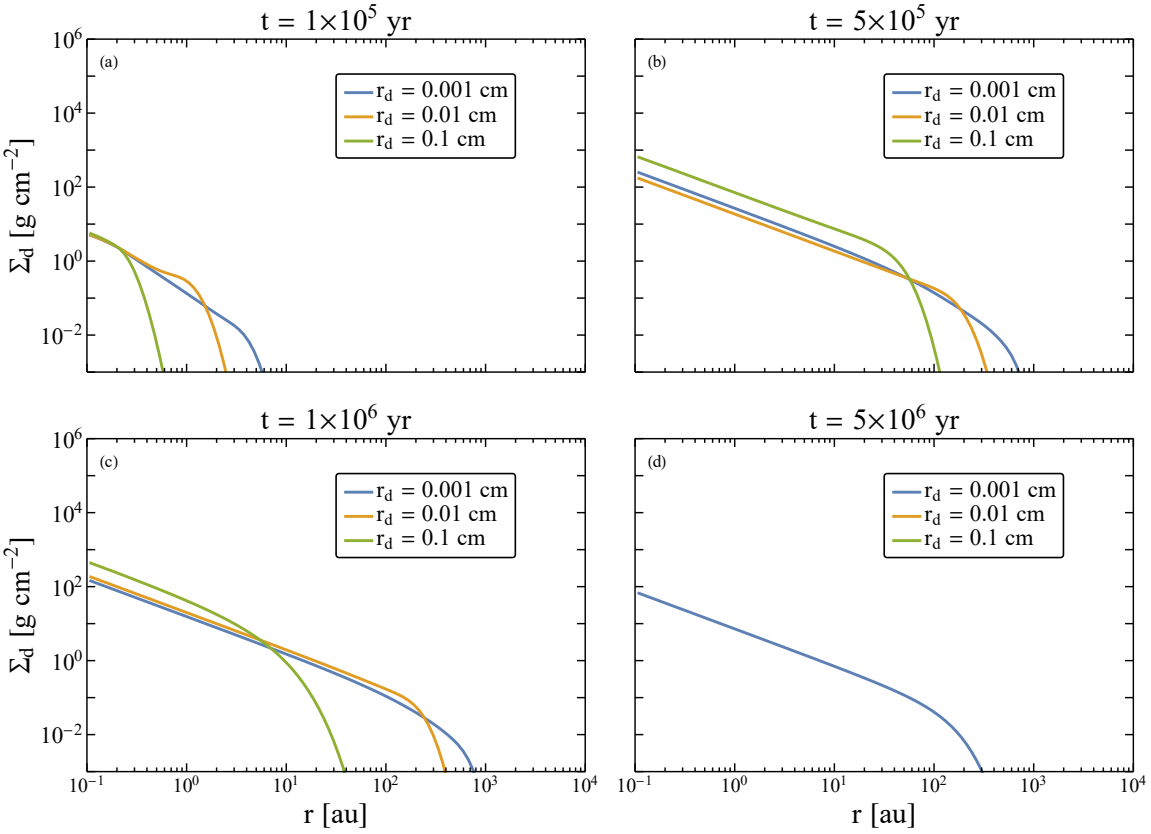

Figure 4.2.1: Snap shots in time of dust surface density for different dust sizes at $1.0 \cdot 10^5$, $5.0 \cdot 10^5$, $1.0 \cdot 10^6$, and $5.0 \cdot 10^6$ yr. Panel (a) shows the dust surface density near the mid point of the formation phase. At this time the dust surface densities are near identical, except for in the outermost part of the disk. The largest dust (green curve) has the largest Stokes number and becomes drift-dominated first. This can be seen in panel (c), where the large dust has drained from the outer disk. The inner disk is replenished with dust, increasing the surface density in the inner disk. The two smaller dust cases have not yet begun to experience significant drift, and surface densities are relatively unchanged from previous times. At $5.0 \cdot 10^6$ yr, the large dust and reference case have both been completely drained, but the small dust size case has not.

In this section we will explore how different dust sizes affect the evolution of the dust disk. Since larger dust are more affected by the gas drag it drifts faster than the smaller dust. Therefore, it will not be as long lived. How this affects the dust-to-gas ratio is not as obvious however. We will compare the results of using dust of sizes 0.1, 0.01, and 0.001

cm. The other run parameters are kept the same as in the `refrun` case, and can be seen in Table 4.1.

During the initial part of the formation phase, dust surface densities are similar in all three cases. Panel (a) of Figure 4.2.1 shows this at $1.0 \cdot 10^5$ yr. In the very outer parts of the disk one can see that the largest dust case (green curve) does not as much follow the viscous evolution of the gas disk as the other two cases, due to it being less coupled to the gas. As time goes on, this case is drained faster than the other two cases for this reason. It takes $\sim 1.0 \cdot 10^6$ yr to drain this disk, whereas the `refrun` case takes $\sim 2.8 \cdot 10^6$ yr to drain completely and the small dust case drains very little in the $5.0 \cdot 10^6$ yr simulation. This can be seen in Figure 4.2.2, which shows the total mass in the dust disk, and the mass outside of 100 au.

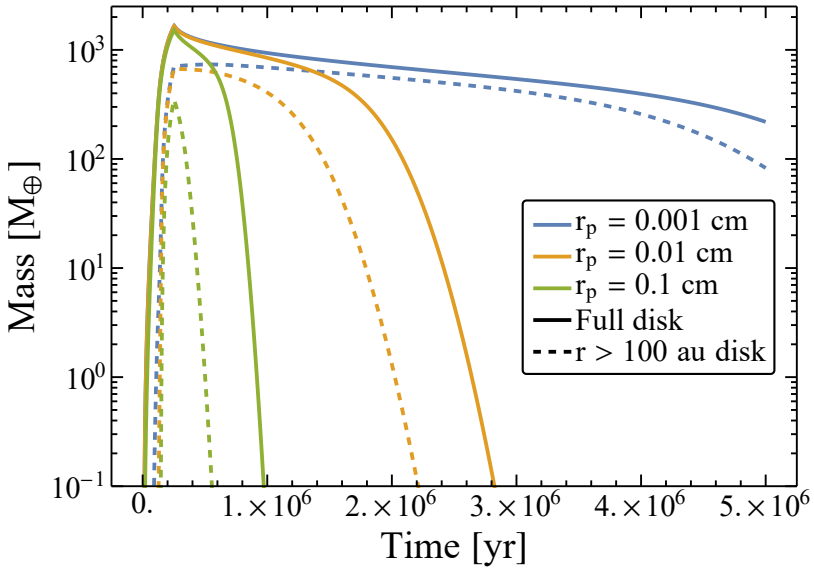

Figure 4.2.2: Dust masses in the whole disk (solid curves) and outside of 100 au (dashed curves). The 0.1 cm size dust case (green curves) drains the outer disk in $\sim 6 \cdot 10^5$ yr and the whole disk in $\sim 1.0 \cdot 10^6$ yr. The 0.01 cm case (yellow curves) drains the outer disk in $\sim 2.1 \cdot 10^6$ yr. The whole disk is drained in about 10^6 yr later. The smallest dust case retains its dust disk for the entire $5 \cdot 10^6$ yr period, and the outer disk contains 55 % of it even at the end of the $5 \cdot 10^6$ yr period.

We now explore how the dust-to-gas ratio evolves differently for the three dust size cases. Figure 4.2.3 shows the dust-to-gas ratio at $2.5 \cdot 10^5$, $5.0 \cdot 10^5$, $2.0 \cdot 10^6$, and $4.5 \cdot 10^6$ yr in panel (a), (b), (c), and (d) respectively. As discussed previously, the largest dust does not build up an outer reservoir of dust since it is more dominated by drift than viscous evolution. Therefore the largest dust drains the fastest, meaning that the dust-to-gas ratio also reaches its peak the fastest. The $r_p = 0.1$ cm case reaches a peak dust-to-gas ratio of $\epsilon = 0.062$ at the time $t = 6.8 \cdot 10^5$ yr. The smallest dust case on the other hand is very well coupled to the gas and drift only begins do dominate over viscous evolution at times

$> 4 \cdot 10^6$ yr. This small dust reaches it peak dust-to-gas ratio at the end of the $5.0 \cdot 10^6$ yr period simulated. It reaches a value of $\epsilon = 0.044$, however, since it is at the very end of the simulation it would most likely keep increasing to a higher value if the simulation lasted longer. Panel (a) in Figures 4.2.4 and 4.2.5 shows contour plots of the dust-to-gas ratio over radius and time in the entire disk.

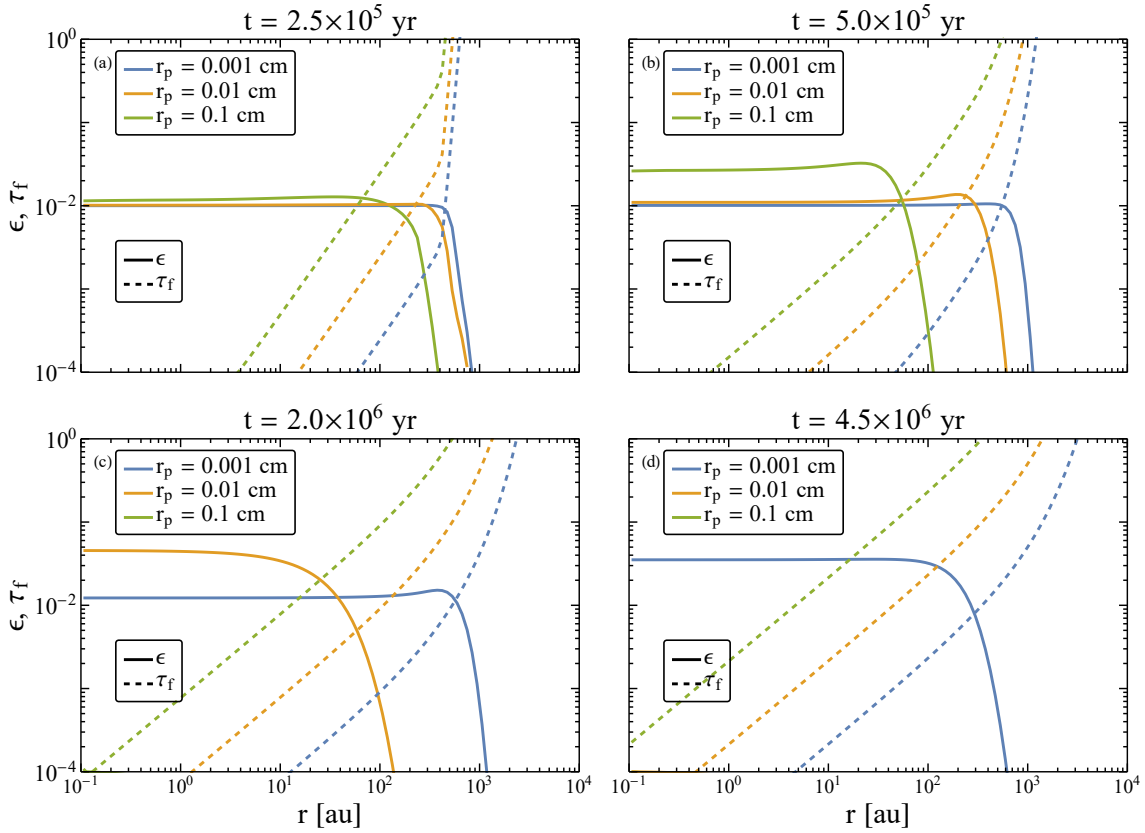

Figure 4.2.3: Maximum dust-to-gas ratio for different dust sizes, at four snapshots taken at $2.5 \cdot 10^5$, $5.0 \cdot 10^5$, $2.0 \cdot 10^6$, and $4.5 \cdot 10^6$ yr. The large dust size case does not couple to the gas as strongly as the smaller dust cases. Therefore it does not viscously evolve as much, and is not able to build up a reservoir of dust in the outer disk. The large dust size disk thus drains faster than the other cases. The smallest sized dust is well coupled to the gas, and only drifts very little. The dust-to-gas ratio therefore remains close to 1/100 for a long time. Only, towards the end of the simulation does this disk begin to drain, and it reaches its maximum dust-to-gas ratio at $5 \cdot 10^6$ yr.

All three disks with different dust sizes become streaming instability active at some point. As mentioned in Section 4.1.2, the `refrun` case becomes streaming instability active between $1.5 \cdot 10^4 - 3.0 \cdot 10^4$ yr and $8.5 \cdot 10^5 - 1.95 \cdot 10^6$ yr. The large dust case has streaming instability regions active between $\sim 3 \cdot 10^5$ yr and $\sim 8 \cdot 10^5$ yr, at radii between 100 au and 30 au the small dust has active regions from $\sim 3 \cdot 10^6$ yr to the end of the simulation at $5 \cdot 10^6$ yr. This can be seen in panel (b) of Figure 4.2.4 and 4.2.5.

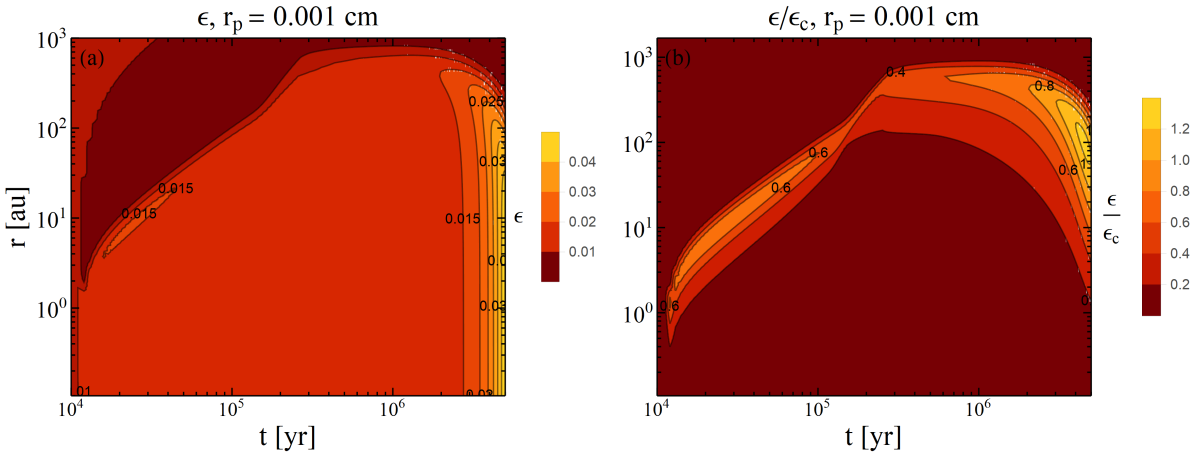

Figure 4.2.4: Panel (a): Contour plots of the dust-to-gas ratio for dust of size $r_p = 0.001$ cm. There is small pile up of pebbles around 10 au early in the disk, and a grater pile up across most of the disk starting after a few 10^6 yr. **Panel (b):** Contour plots of the streaming instability condition for dust of size $r_p = 0.001$ cm. This condition is met at radii near 100 au towards the end of the $5 \cdot 10^6$ yr simulation.

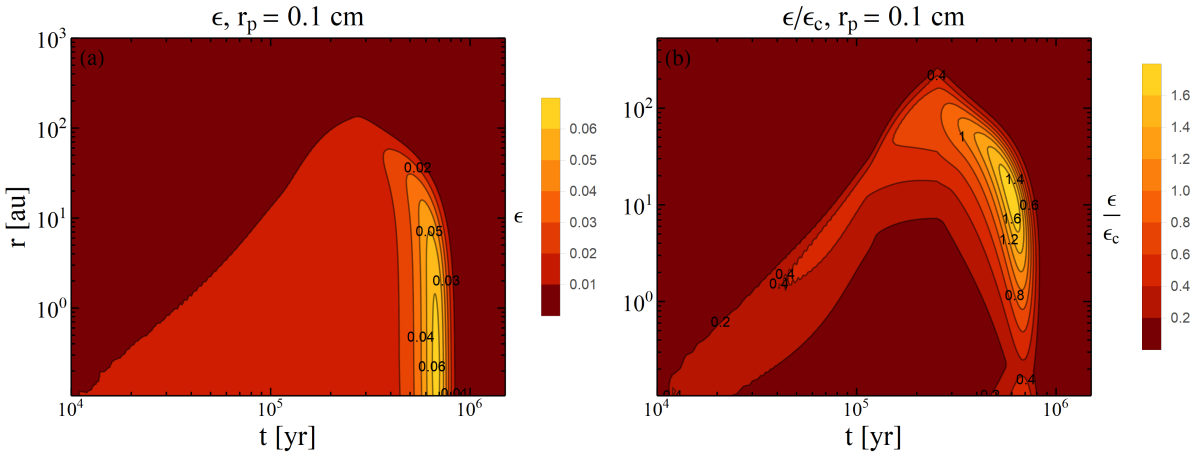

Figure 4.2.5: Panel (a): Contour plots of the dust-to-gas ratio for dust of size $r_p = 0.1$ cm. A pile up occurs after a few 10^5 yr in the inner 10 au of the disk. **Panel (b):** Contour plots of the streaming instability condition for dust of size $r_p = 0.1$ cm. The streaming instability condition is met at radii of a few to a few tens of au between $\sim 3 \cdot 10^5$ and $\sim 8 \cdot 10^5$ yr.

4.2.2 Influence of the cloud rotation on the gas disk

In this section the effect of the cloud core rotation rate on the disk is explored. From Equation (2.32), the centrifugal radius, R_c in the disk as a function of the initial collapsing shell radius, r_{CF}, is given by

$$R_c = \frac{r_{CF}^4 \Omega_0^2}{GM}. \tag{4.4}$$

The maximum centrifugal radius therefore scales with core rotation rate as

$$R_{c,Max} \propto \Omega_0^2. \tag{4.5}$$

The reference case is compared to two other cases. One where the rotation rate has been decreased by an order of magnitude, and one more case which was set up to have a maximum centrifugal radius of 50 au. The run parameters are shown in Table 4.1. We can the specific angular momentum of these cases to observations and simulations. Figure 4.2.6 shows the specific angular momentum of observed and simulated cloud cores as a function of cloud core radius. In the lower left of this figure our three rotation cases are shown by the black dots. This shows that these three rotation cases we investigate span the range of specific angular momenta expected for a core of this size.

Since angular momentum is assumed to be conserved during the collapse, increasing the rotation rate above the `refrun` leads to disks which are significantly more massive than the star. Then the approximation that the angular momentum in the disk is purely Keplerian breaks down. Therefore, this range of parameter space cannot be explored accurately in this model.

The rotation rate of the cloud core does not affect the mass infall rate onto the disk, but it causes the infalling material to be more spread out, which will change the surface density profile. This change can be seen in the maximum centrifugal radius in Table 4.1. The surface densities of gas at $5 \cdot 10^5$, $2 \cdot 10^5$, $3 \cdot 10^5$, and $5 \cdot 10^6$ yr for the three cases is shown in Figure 4.2.7. Considering panel (a), one sees that in the inner parts of the disk the surface density of the `refrun` is lower compared to the lower Ω_0 cases at the early times, because the disk extends further out than in the other cases. At later times, panels (b), (c), and (d), the viscous evolution of the disks causes the surface density in the inner disks to decrease as gas is accreted onto the star. The slower the core was rotating, the faster this decrease in surface density is. A disk from a slower rotating core essentially evolves faster than a disk from a faster rotating core. At the inner edge, the `Low` Ω_0 case changes its surface density by roughly 3 orders of magnitude from the end of the formation phase to the end of the $5 \cdot 10^6$ yr integration period. The `refrun` case changes about 2 order of magnitude in the same time span.

We now examine how gravitational instability affects the different disks. The effect of this can be seen as the two sloped profile in panel (a) of Figure 4.2.7. The slowest rotating case reaches a minimum Toomre Q of $Q_{\mathrm{Min,Low}\ \Omega} = 2.16$, and the criterion for instability

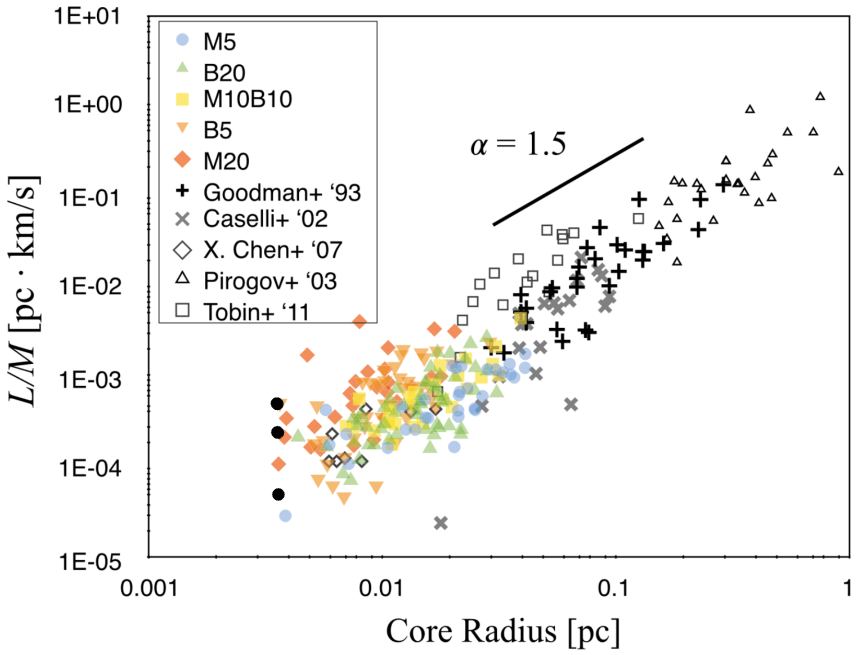

Figure 4.2.6: Specific angular momentum of observed (black and white symbols) and simulated (coloured symbols) molecular cloud cores as a function of cloud core radius. The three black dots in the lower left indicate the position of the tree rotation rate cases explored here. As can be seen they span the range of expected specific angular momenta for a cloud core of this size. Credit:

is $Q \lesssim 2$. This disk only ever becomes slightly unstable. This is because the disk is centrally located, hence, both Ω_k and the sound speed are high, which lowers Q. The intermediate rotating cases reach minimum Q values of $Q_{\mathrm{Min},R_{\mathrm{c}}50\mathrm{au}} = 1.39$ and $Q_{\mathrm{Min,ref}} = 1.29$ respectively.

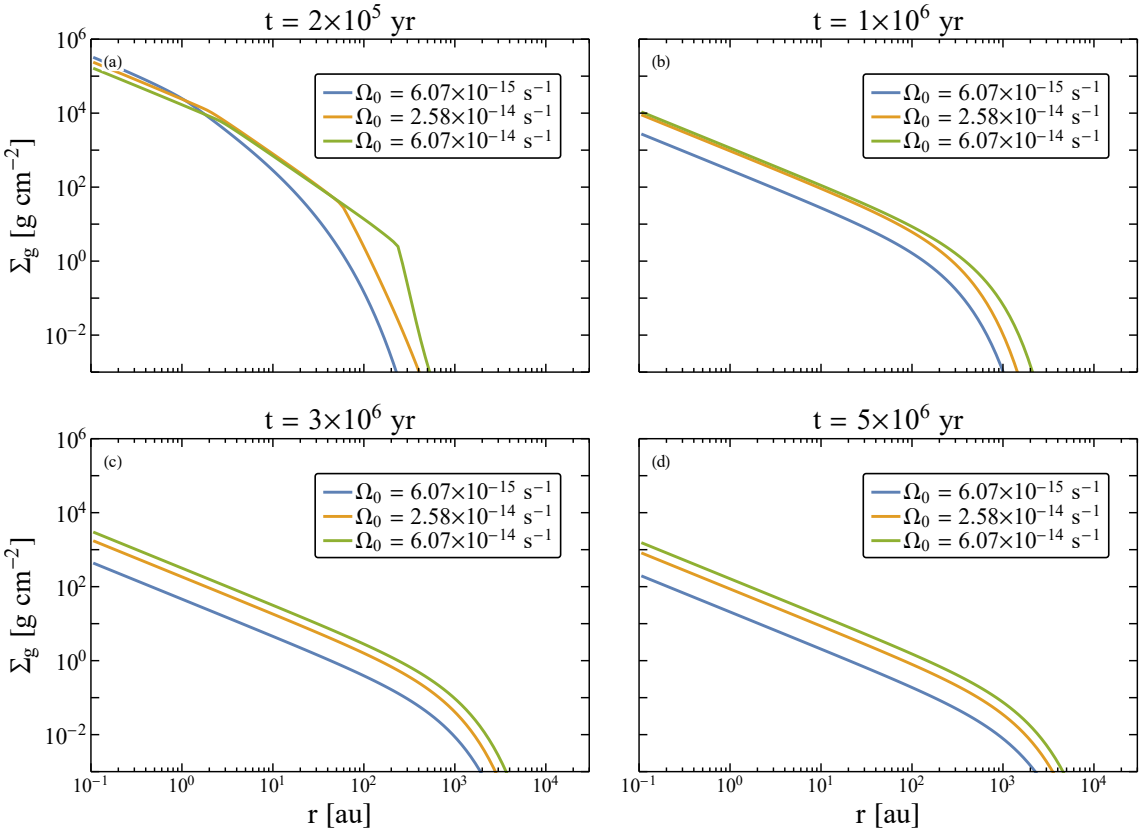

Figure 4.2.7: Panel (a) to (d) shows the gas surface density at $2 \cdot 10^5$, $1 \cdot 10^6$, $3 \cdot 10^5$, and $5 \cdot 10^6$ respectively. At $2 \cdot 10^5$ yr, the slowest rotating case (blue curve) have a higher surface density in the inner disk than the other cases. This is because the lower centrifugal radius causes more of the gas to be deposited close to the star. The $R_{c,\texttt{Max}} = 50$ `au` (yellow) case sits between the two other cases. As the disks evolve, the slower the core was rotating the faster the disk is drained. In panel (a) one can also see the effect of the gravitational instability in the two sloped profile that is present in the two intermediate cases. The fastest rotating case is so spread out that it never becomes gravitationally unstable. The slowest rotator on the other hand is to centrally located to become significantly unstable.

The slower rotating cores create disks with lower masses. Panel (a) in Figure 4.2.8 shows the mass of the star (solid curve) and the disk (dashed curve) for the three core rotation rates studied. The lower rotation rate initially creates a less massive disk because more of the infalling material lands directly onto the star, rather than landing onto the disk, due to the lower centrifugal radius. See Section 3.5.3 for a discussion on this. The faster the core rotates, the more of the infalling gas lands on the disk, creating a more massive disk. The ratio of the disk and star mass as a function of time is shown in Figure 4.2.8 (b). The `Low-`Ω_0 case has a maximum gas-disk-to-star mass ratio which is 0.17, which is 18 % of the `refrun` maximum mass ratio. The ratio at the end of the $5 \cdot 10^6$ yr period is 0.015, which is about an order of magnitude lower than the `refrun`, which has a ratio of 0.17 at

the end. The R_c = 50 au case has a ratio of 0.07 at the end.

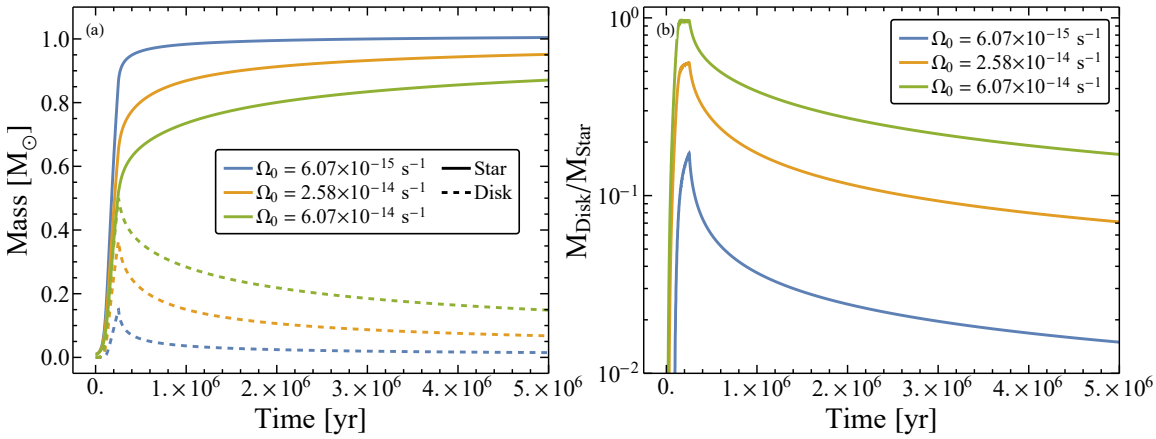

Figure 4.2.8: Panel (a) shows the masses of the stars (solid curves) and the disks (dashed curves) for the three core rotation rates cases. Panel (b) shows the ratio of the disk to star mass. A faster rotating core leads to a more massive disk and consequently a higher gas-disk-to-star mass ratio.

The stellar accretion rate and the disk infall rate as a function of disk mass is shown in panel (a) of Figure 4.2.9. The point markers show the 10^5 yr (dark blue), $2.5 \cdot 10^5$ yr (pink), $2.5 \cdot 10^6$ yr (dark green), and $5 \cdot 10^6$ (black) yr positions. The peak stellar mass accretion rate increases with decreasing core rotation rate. Here one can also see the faster evolution of the disk from the `Low` Ω_0 case (blue curve). From the end of the formation phase, the pink marker, to the end of the simulation, this disk drops more than three orders of magnitude in accretion and almost one order of magnitude in disk mass, whereas the `refrun` core (green curve) only drops about one order of magnitude less in accretion and a factor of ~ 3.5 in disk mass. From this one can conclude that disk lifetimes increase with a faster rotating cloud core, i.e. with a larger angular momentum budget in the cloud core. Photoevaporation is expected to have a rate of roughly 10^{-9} $M_\odot$ yr^{-1} (Owen et al. 2011) and will become important once accretion rates are similar. The `Low` Ω_0 case reaches an accretion rate of 10^{-9} $M_\odot$ yr^{-1} so photoevaporation is expected to clear the disk of gas, whereas the other two cases do not evolve as quickly, and hence they live longer.

Figure 4.2.9 also tells us that for a given stellar accretion rate, there is not a single corresponding disk mass. Some accretion rate could even correspond to any of the three disks in either the formation or evolution phase. However, since the formation phase is much shorter than the evolution phase, the likelihood of catching a disk in the formation phase is lower. For a given accretion rate, it is therefore more likely that the disk is in the evolution phase. Since disks from faster rotating cores evolve slower, and spends more time at a given accretion rate, it is also more likely that one catches a disk from such a faster rotating core. By connection points of equal time in panel (a) of Figure 4.2.9 one can trace isochrones over core rotation rates. These are shown in panel (b) of Figure 4.2.9. With these one can

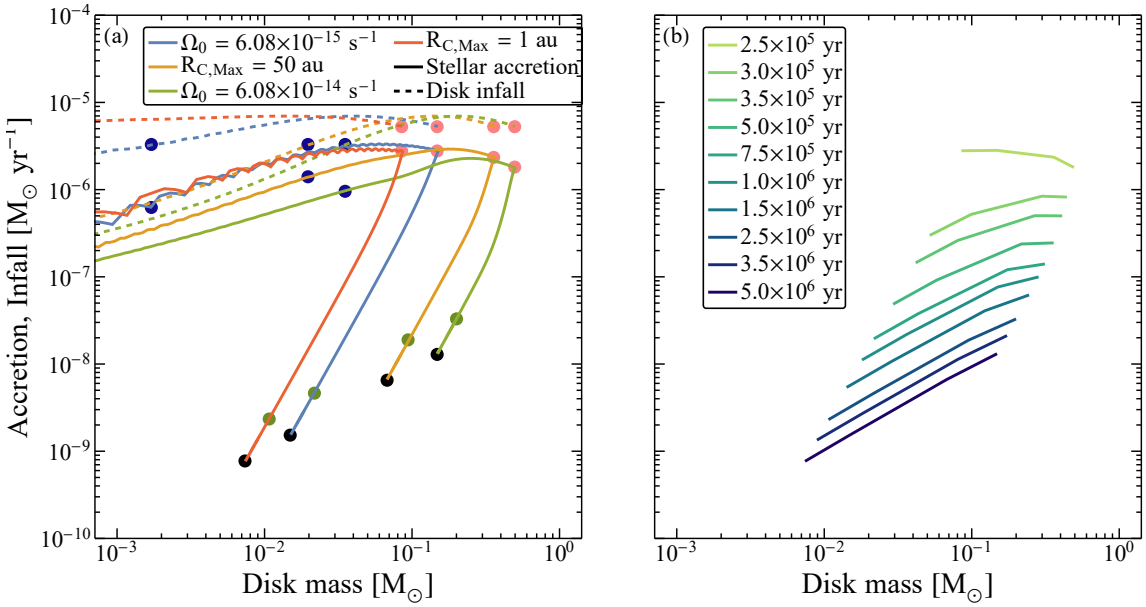

Figure 4.2.9: Panel (a): Stellar mass accretion rate (solid curves) and disk infall rate (dashed curves) for the three core rotation cases. The blue dots show the $8.5 \cdot 10^4$ yr point, the pink dots the $2.5 \cdot 10^5$ yr (end of the formation phase), and the green and black dots show the $2.5 \cdot 10^6$ and $5 \cdot 10^6$ yr mark respectively. Slower rotating cores create disks which evolve faster, decreasing more in both accretion rate and disk mass once the formation phase is over. The orange curve is a run that was made only to extend the parameter range explored in this figure and is not included in any other figure. It is discussed in Section 5.2. **Panel (b):** Isochrones showing how the accretion rate as a function of disk mass for a given age varies and evolves with different cloud core rotation rates.

finds that during the later times, the stellar accretion versus disk mass relation becomes nearly linear for different initial conditions, going as $\dot{M} \propto M_{\rm Disk}^{\beta}$, where $\beta \simeq 0.9 - 0.95$ from $2 \cdot 10^6$ yr to the final point of $5.0 \cdot 10^6$ yr.

In terms of how the stellar gas accretion rate scale with time, we find that at times $> 5 \cdot 10^5$ yr after the end of the formation phase it decreases as $\dot{M}_{\rm accrete} \propto t^{-\xi}$ where $\xi = 1.7$ for the `Low-`Ω_0 case and $\xi = 1.5$ in the $R_{\texttt{c,Max}} = 50$ `au` case. This can be compared with $\xi = 1.2$ in the `refrun` case.

4.2.3 Influence of cloud rotation on the dust disk

The run parameters used in these runs are listed in Table 4.1. These are the same as for the gas disk discussed in Section 4.2.2. The dust is of constant size $r_d = 0.01$ cm in all cases.

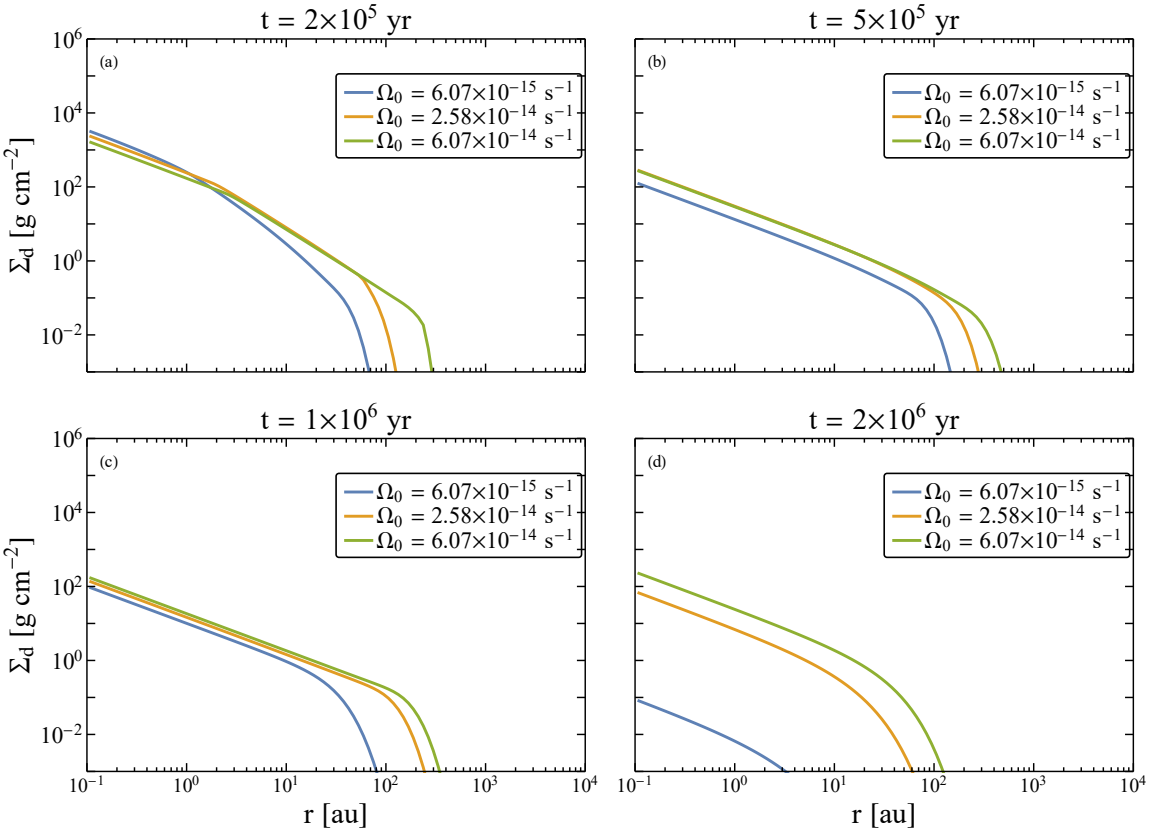

Figure 4.2.10: Surface density of dust at for the three rotation cases at $2 \cdot 10^5$, $5 \cdot 10^5$, $1 \cdot 10^6$, and $2 \cdot 10^6$ yr. Initially, the slowest rotating case (blue curve) has the highest surface density in the inner parts of the disk of the three cases, but it is not able to build up a reservoir of dust in the outer parts of the disk. It therefore drains quickly. The faster rotating cases are able to build an outer reservoir of dust and can therefore maintain the surface density in the inner disk as the reservoir feeds it with drifting dust.

The effect of the cloud rotation rate on the dusk disk surface density can be seen in Figure 4.2.10. The figure shows the disk at $2 \cdot 10^5$, $5 \cdot 10^5$, $1 \cdot 10^6$, and $2 \cdot 10^6$. At the $2 \cdot 10^5$ yr snapshot, the dust surface density mirrors that of the gas. The `Low` Ω_0 case (blue curve) has a dust disk with the smallest outer radius, but it has a slightly higher surface density in the inner disk. The `refrun` case (green curve) has the lowest surface density in most of the disk, but it also extends significantly further out. Over the next snapshots one can see how the `refrun` case is drained of dust. At $2 \cdot 10^6$ yr this disk is drained, the surface density is now less than 10^{-1} g cm^{-2} at the inner edge of the disk. The two faster rotating

cases both still have significant disks left, but are also beginning to be drained. At $3 \cdot 10^6$ yr, all three cases have drained their dust disks.

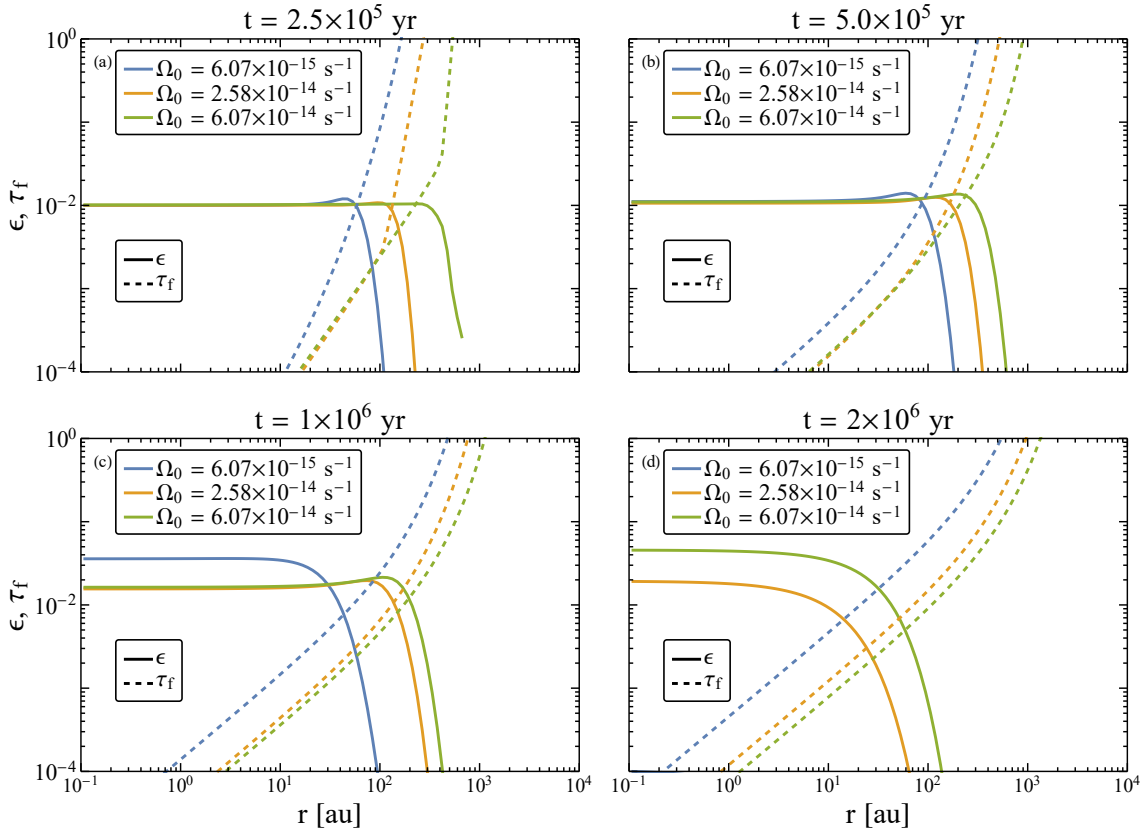

Figure 4.2.11: Dust-to-gas ratio, ϵ, (solid curves) and Stokes number, τ_f, (dashed curves) at $2.5 \cdot 10^5$, $5.0 \cdot 10^5$, $1.0 \cdot 10^6$, and $2.0 \cdot 10^6$ yr for the three rotation cases explored, using a dust size of $r_p = 0.01$ cm. In the first $5 \cdot 10^5$ yr, all disk are dominated by viscous evolution, keeping $\sigma \sim 1/100$. With time, the slower rotating case (blue curve) becomes drift dominated first and drains the fastest. In the final panel the slowest rotating case has been drained of dust, which is why it is not present

We now consider how the dust-to-gas ratio evolves between the different cases. This is shown in Figure 4.2.11. It shows the dust-to-gas ratio and the Stokes number of the dust at $2.5 \cdot 10^5$, $5.0 \cdot 10^5$, $1.0 \cdot 10^6$, and $2.0 \cdot 10^6$ yr. In panel (a) and (b) one sees that in the first $5 \cdot 10^5$ yr, the dust-to-gas ratio changes very little, showing that all three cases are in the regime where viscous evolution dominates over drift. Stokes numbers are increasing as the gas surface density drops, pushing the dust towards the drift regime. In panel (c) the dust to gas ratio of the `Low` Ω_0 case has begun to increase. The Stokes number is now large enough that this dust disk has now transitioned into the drift dominated regime. The dust-to-gas ratio in the faster rotating cases have only started to increase slightly near the edge of the dust disk. At $2 \cdot 10^6$ yr, both the `refrun` the $R_{c,\texttt{Max}} = 50$ `au` case are in the drift regime. The reference case (green curve), the $R_{c,\text{Max}} = 50$ au case (yellow curve),

and the slowest case (blue curve) reach peak dust-to-gas ratios of $\epsilon = 0.051$, $\epsilon = 0.045$ and $\epsilon = 0.045$ respectively. However, they peak at very different times. The `Low Ω` case reaches its peak value at $1.1 \cdot 10^6$ yr, $R_{c,\mathrm{Max}} = 50$ au case at $1.7 \cdot 10^6$ yr and the `refrun` case does so at $1.8 \cdot 10^6$ yr. The maximum dust-to-gas ratio is taken as the highest value that any cell in the simulation reaches. This always happens at the innermost cell. But, as one can see from panel (c) and (d) in Figure 4.2.11 the dust-to-gas ratio is almost always global in the dust disk.

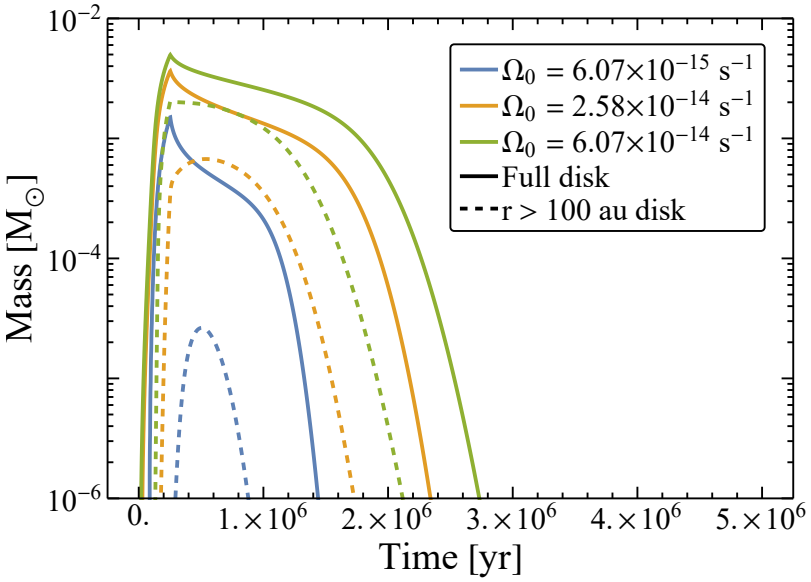

Figure 4.2.12: Dust disk masses for the whole disk (solid curves) and the outer disk $r > 100$ au (dashed curve). The faster the molecular cloud core rotates, the more dust is deposited in the outer disk, and a larger fraction of the total dust mass is present there.

Due to the larger centrifugal radius of the fastest rotating case, more of the dust is deposited at very large radii. This coupled with the outward flow of dust due to viscous evolution creates a large outer reservoir of dust. Figure 4.2.12 shows the total dust disk mass and the mass of the dust at radii $r > 100$ au. Here, one can see that the slowest rotating case (blue curve) has virtually no mass this far out. This is not surprising since the dust disk never grows this large. In the faster cases the mass in the outer disk contains a significant portion of the total dust mass. In the `refrun` case (green curve) one can see how after $\sim 1.5 \cdot 10^6$ yr, the outer disk is starting to be drained of mass, supplying the inner disk with new dust, and after $\sim 2.6 \cdot 10^6$ yr, the outer disk is completely drained.

4.2.4 The effect of different masses of cores on the gas disk

In this section we will explore how different masses of the cloud core affects the disk formation and evolution. We will compare the reference 1.0 $M_\odot$ case with that of a 0.5 and a 2.0 $M_\odot$ cloud core. The rotation rate of each cloud core is calculated using Equation (2.57). While the total angular momentum of a cloud core increases with the mass, the rotation rate decreases as the mass increases. This decrease happens because the moment of inertia increases faster with the radius than the specific angular momentum. Therefore, the rotation rate must decrease. The full run parameters of these cases are shown in Table 4.1.

As with the rotation rate, we first look at how the maximum centrifugal radius scales with cloud core mass. From Equation (4.4), the maximum centrifugal radius scales as

$$R_{\rm c,Max} \propto \frac{R_{\rm BE}^4}{M_{\rm BE}}. \tag{4.6}$$

$R_{\rm BE}$ is the radius of a cloud core modelled by a Bonnor-Ebert sphere, and $M_{\rm BE}$ is the mass of the cloud. The cloud radius scales linearly with the mass, see Section 3.1.2. Therefore the maximum centrifugal radius scales with the cloud core mass as

$$R_{\rm c,max} \propto M_{\rm BE}^3. \tag{4.7}$$

The formation phase of the disk will last longer for more massive cloud cores. The duration of the formation phase scales approximately linear with the core mass. Figure 4.2.13 shows the mass infall rate onto the disk for the 0.5, 1.0, and 2.0 $M_\odot$ cloud cores. The formation phase last $\sim 1.25 \cdot 10^5$ yr for the `Low mass` case, and $\sim 2.5 \cdot 10^5$ and $\sim 5.0 \cdot 10^5$ yr for the `refrun` and `High mass` case respectively. This is linear growth of formation time scale with the cloud mass is supported by Equation (2.15). Since $R_{\rm BE} \propto M_{\rm Be}$, via Equation (3.11), $t_{\rm infall} \propto M_{\rm BE}$. The three cases display similar behaviour. There is an initial period of increasing infall rate for the first half of the phase, and then a period with a very slowly decreasing infall rate. The three cases also reach a similar peak infall rate $\sim 7 \cdot 10^{-6}$ $M_\odot$ yr^{-1}. They reach similar peak infall rates because in the outer parts of the Bonnor-Ebert sphere, the density profile approaches that of a singular isothermal sphere, which has a constant accretion rate. The latter half of the formation phase with nearly constant accretion rate corresponds to this part of the Bonnor-Ebert sphere. Thus, the behaviour of the 2.0 $M_\odot$ case is much like that of the 0.5 $M_\odot$ case stretched out over the longer formation phase.

The evolution of the surface density over times can be seen in Figures 4.2.14. The lower mass core (blue curve) creates a disk that is both smaller in size and in surface density than the other cases. However, during the initial formation phase the situation is reversed. At this time the formation phase of the low-mass case is almost over, and this core has reached higher infall rates than the other at this time (see Figure 4.2.13). A significant portion of

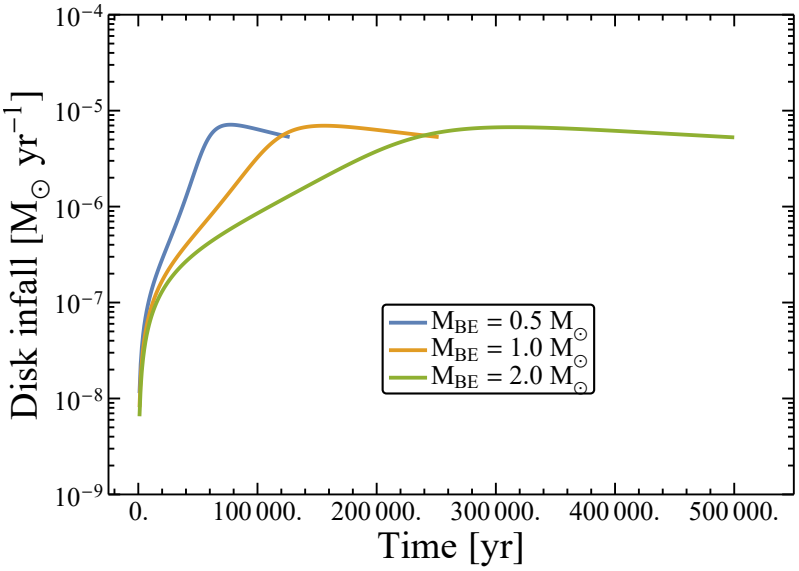

Figure 4.2.13: Disk mass infall rate for a 0.5, 1.0, and 2.0 $M_\odot$ cloud core over time. Each of the three cases reach similar peak accretion rates, but the less massive the core is the shorter the formation phase is. The profiles of all three cases are similar, only stretched out over the time of their formation phases.

its total mass has been deposited now. Since the final centrifugal radius is smaller, this mass lands in the inner disk. Therefore, the low-mass case has a higher surface density than the two other cases at this early time. All disks become gravitationally unstable towards the end of their formation phases.

Figure 4.2.15 (a) shows the evolution of the star and disk masses, and (b) the ratio of the star and disk mass for the three core masses. A lower mass core creates a disk which is of lower mass relative to the star. The peak disk-to-star-mass ratio of each case is 0.65, 0.97, and 1.44 for the 0.5, 1.0, and 2.0 $M_\odot$ cases respectively. The disk from the 0.5 $M_\odot$ core is never more massive than the star, while the 2.0 $M_\odot$ core creates a disk which is more massive than the star for $\sim 0.8 \cdot 10^6$ yr. As with the faster rotating cores, the higher disk mass is caused by the larger centrifugal radius. This in turn causes more of the infalling material to land on to the disk, rather than directly on to the star.

Considering the ratio of the disk and star mass, the high value of the 2.0 $M_\odot$ case is of concern. Such a high ratio makes the approximation of Keplerian rotation in the disk questionable, as the gravity from the disk becomes significant, which is not included in this model. The results of this case are therefore not as reliable as the others.

The stellar mass accretion rate as a function of the disk mass is shown in Figure 4.2.16. The overall behaviour of the different curves are very similar to those of the different core rotation rates in Figure 4.2.9. As with the different rotation rates, there is a degeneracy between accretion rate and disk mass for different mass cores. A single accretion rate can

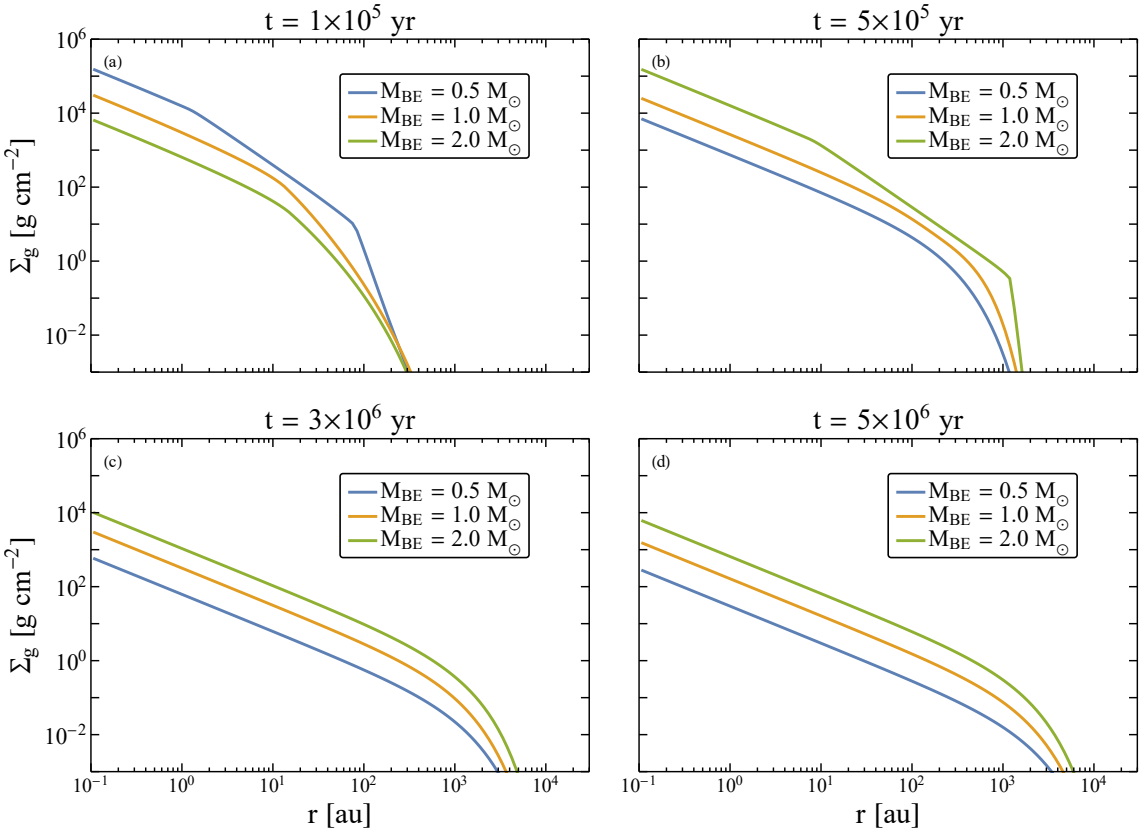

Figure 4.2.14: Gas surface density of the disk for a 0.5, 1.0, and 2.0 $M_\odot$ cloud core at $1 \cdot 10^5$, $5 \cdot 10^5$, $3 \cdot 10^6$, and $6 \cdot 10^6$ yr. The lower mass core initially becomes more massive, since at this time it has had a higher infall rate. At later times, a more massive core also creates a more massive disk with a larger outer radius.

correspond to different disk masses, depending on the mass of the molecular cloud core from which the star and disk formed. Notable is that the disk from the lowest mass core (blue curve) accretes at a slightly higher peak rate during the formation phase. The disk from a more massive core evolves slower, and hence it live longer. The change from peak to the lowest accretion rate is smaller the more massive the core was, and the disk mass similarly decreases less. Therefore, for a given accretion rate, a high-mass disk would be more likely to be observed, as it evolves slower and therefore spends more time at any given accretion rate, as with the faster rotating cores. As with the rotation rate, for a given time the accretion rate versus disk mass relation scales nearly linearly over cloud core masses as $\dot{M} \propto M_{\rm Disk}^{0.88}$.

For these different mass cases we find that at times $> 5 \cdot 10^5$ yr after the end of the formation phase the stellar gas accretion rate decreases with time as $\dot{M}_{\rm accrete} \propto t^{-\xi}$. $\xi = 1.4$ in the `Low-mass` case and $\xi = 1.1$ in the `High-mass` case, compared to $\xi = 1.2$ in the `refrun` case. We also find that at a given time after time zero the accretion rate scale with stellar

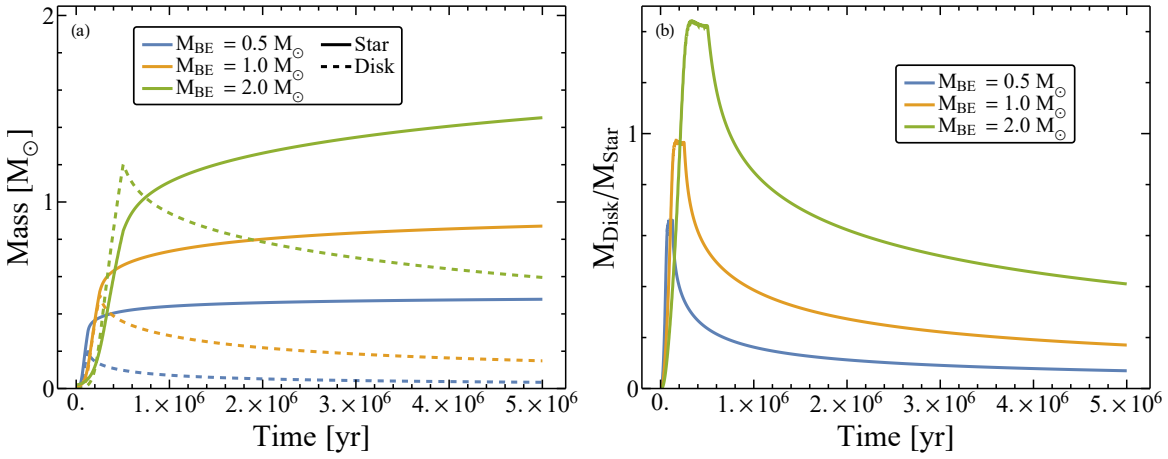

Figure 4.2.15: Panel (a) shows masses of the star and disk for a 0.5, 1.0, and 2.0 $M_\odot$ cloud core, and panel (b) shows the ratio of the disk and star mass. Since a more massive core creates a more massive disk, a higher disk-to-star-mass ratio is expected, as we also see .

mass as $\dot{M}_{\rm accrete} \propto M_\star^\zeta$, where $\zeta \sim 2.2$, although there is some variation across time, with $\zeta = 2.0$ at $2.5 \cdot 10^6$ yr. We note however that if instead of taking equal times after time zero, one instead uses equal times after the end of the formation phase then changes from $\zeta = 1.5 - 2.1$ between 10^6 yr and $5 \cdot 10^6$ yr.

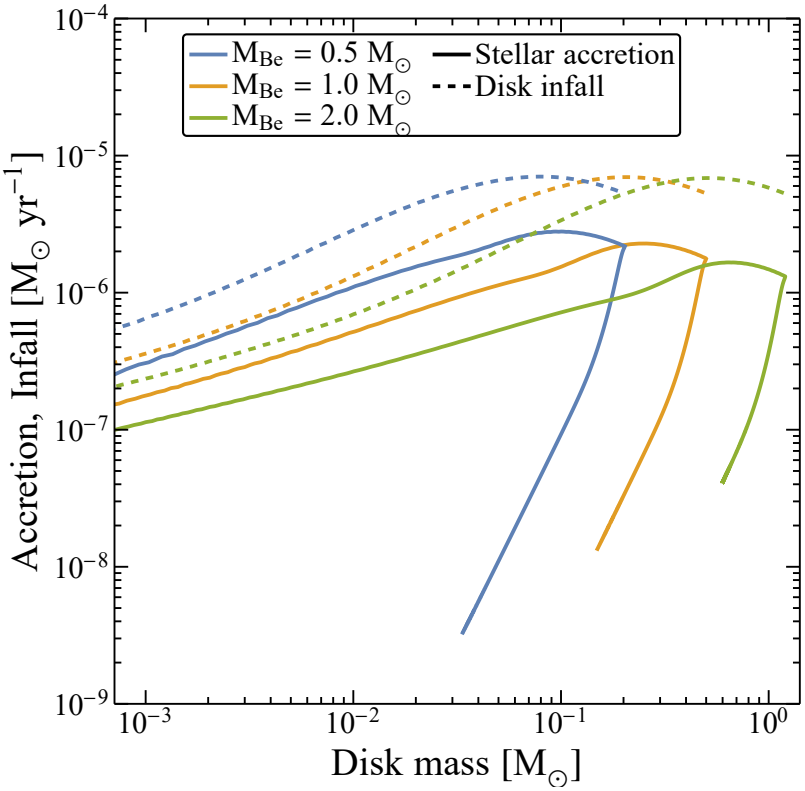

Figure 4.2.16: Accretion rate onto the star and disk infall rate as a function of disk mass for a 0.5, 1.0, and 2.0 $M_\odot$ cloud core. The lowest mass case reaches the highest peak accretion rate towards the end of its formation phase. After the formation phase is over it evolves the fastest of the three cases, reaching the lowest accretion rate and disk mass. As with the different rotation rate cases, see Section 4.2.2, there exists a degeneracy between disk masses for a given accretion rate. a single accretion rate does not correspond to a single disk mass.

4.2.5 The effect of different masses of cores on the dust disk

The run parameters of these runs are shown in Table 4.1, the same as used for the gas disk results discussed in Section 4.2.4. The dust size was constant at $r_d = 0.01$ cm.

The evolution of the dust surface density is shown in Figure 4.2.17. It shows the dust surface density for the three mass cases of 0.5, 1.0, and 2.0 $M_\odot$. As for the gas, the behaviour of the different mass disks is not surprising. The lowest mass core gives a disk with a higher dust surface density at $1 \cdot 10^5$ yr. This is caused by the low-mass core having gone through its phase of the highest infall, whereas the more massive cores have still not reached that point. After the formation phase of the most massive core is over ($\sim 5 \cdot 10^5$ yr), this core has the largest disk with the highest surface density, and vice versa. The

dust disk from a more massive core is also able to maintain a dust disk for longer, not only because it has a higher surface density after the formation phase, but also because like the fast rotators, it is able to build up a reservoir of dust far out in the disk.

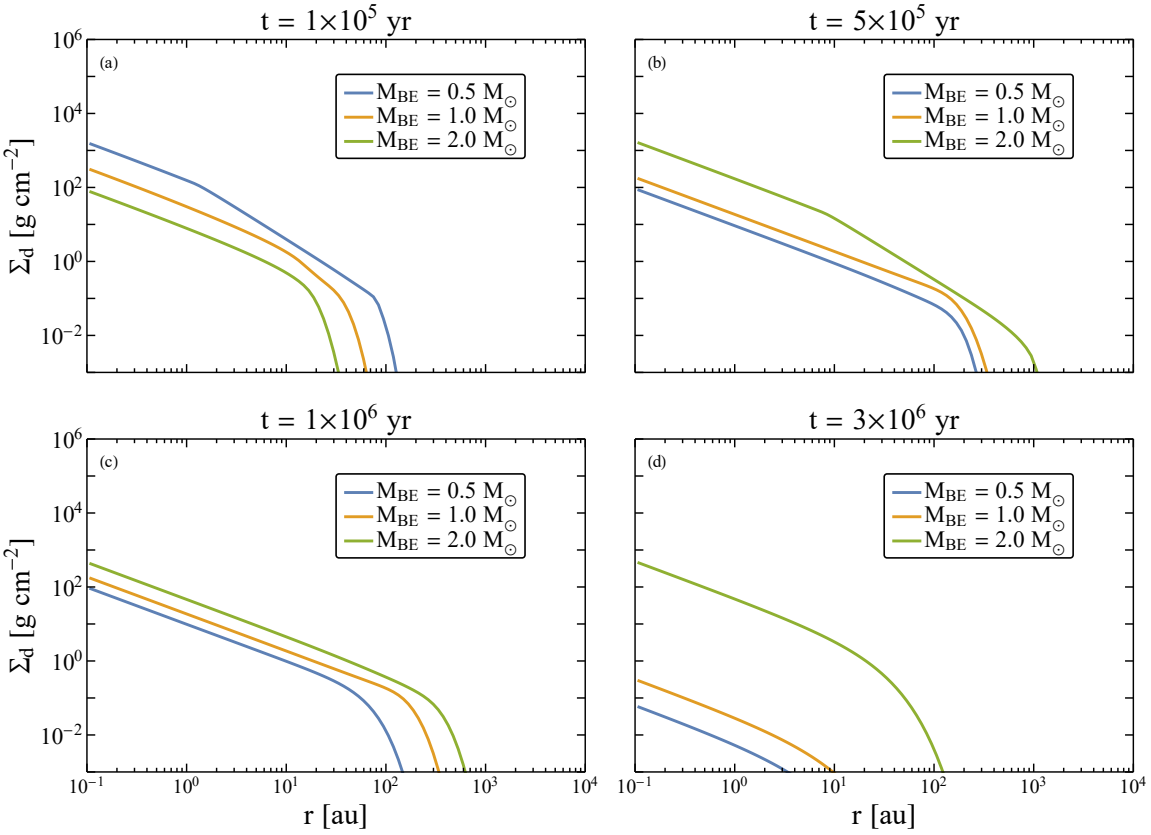

Figure 4.2.17: Surface density of dust at different times for different cloud core masses. The dust with a constant particle size of 0.01 cm behaves much as one might expect. At $1 \cdot 10^5$ yr, the dust surface density mirrors that of the gas. The lowest mass core (blue curve) has had a higher infall rate, giving a larger disk with a higher surface density. With time, the more massive cores (yellow and green curves) grow larger with a higher surface density. The most massive core (green curve) has the largest disk with the highest surface density. The dust also takes a longer time to drain from this disk than the lower core mass cases.

The mass of the dust in the whole disk and outside of 100 au is shown in Figure 4.2.18. Here, the behaviour is similar to that of the different rotating cases in Figure 4.2.12, although not as pronounced. A more massive core creates a more massive dust disk, with a larger fraction of the mass in the outer disk. This dust disk is also longer lived as the outer reservoir is able to feed the disk and keep it around for longer. This disk only starts to significantly decrease in mass after $> 3 \cdot 10^6$ yr, whereas the lowest mass case begins to rapidly drain after $< 1 \cdot 10^6$ yr, and is completely drained after $1.8 \cdot 10^6$ yr.

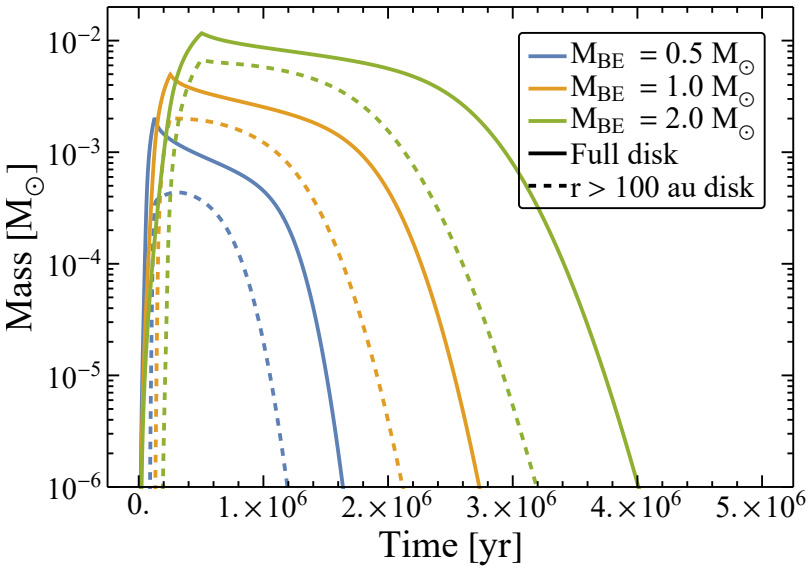

Figure 4.2.18: Dust disk masses for the whole disk (solid curves) and the outer disk $r > 100$ au (dashed curve). The more massive the cloud core is, the more massive the disk becomes, and a larger fraction of the dust is present in the outer disk. Since the `High-mass` is more massive, it also takes longer to drain the outer disk of the case. Therefore, its disk is longer lived compared to the other tow cases.

Snapshots of the dust-to-gas ratio at four different times for the three mass cases can be seen in Figure 4.2.19. At $2.5 \cdot 10^5$ yr (panel (a)) all three cases have very similar dust-to-gas ratio in most of the disk, but the dust disk extends further put in the `Low-mass` (blue curve) and the `refrun` (yellow curve) case. As the disks evolve, the `Low-mass` case drains its dust disk faster than the other two cases. At $2.0 \cdot 10^6$ yr (panel (d)) it has been completely drained, which is why the blue curve is not visible there. In panel (d) we can also see that the dust disk in the `refrun` has also begun to drain. The `High-mass` case (green curve) has not yet begun to drain significantly, even at $2.0 \cdot 10^6$ yr. The most massive case reaches a maximum dust-to-gas ratio of $\epsilon = 0.098$, and the reference case and low-mass case reach $\epsilon = 0.58$ and $\epsilon = 0.48$ respectively. They do so at $2.9 \cdot 10^6$, $2.0 \cdot 10^6$, and $1.2 \cdot 10^6$ yr, with the most massive case peaking at the latest time. Interestingly, if gravitational instability and Stokes drag is not included in the simulation, all three cases reach very similar maximum dust-to-gas ratios.

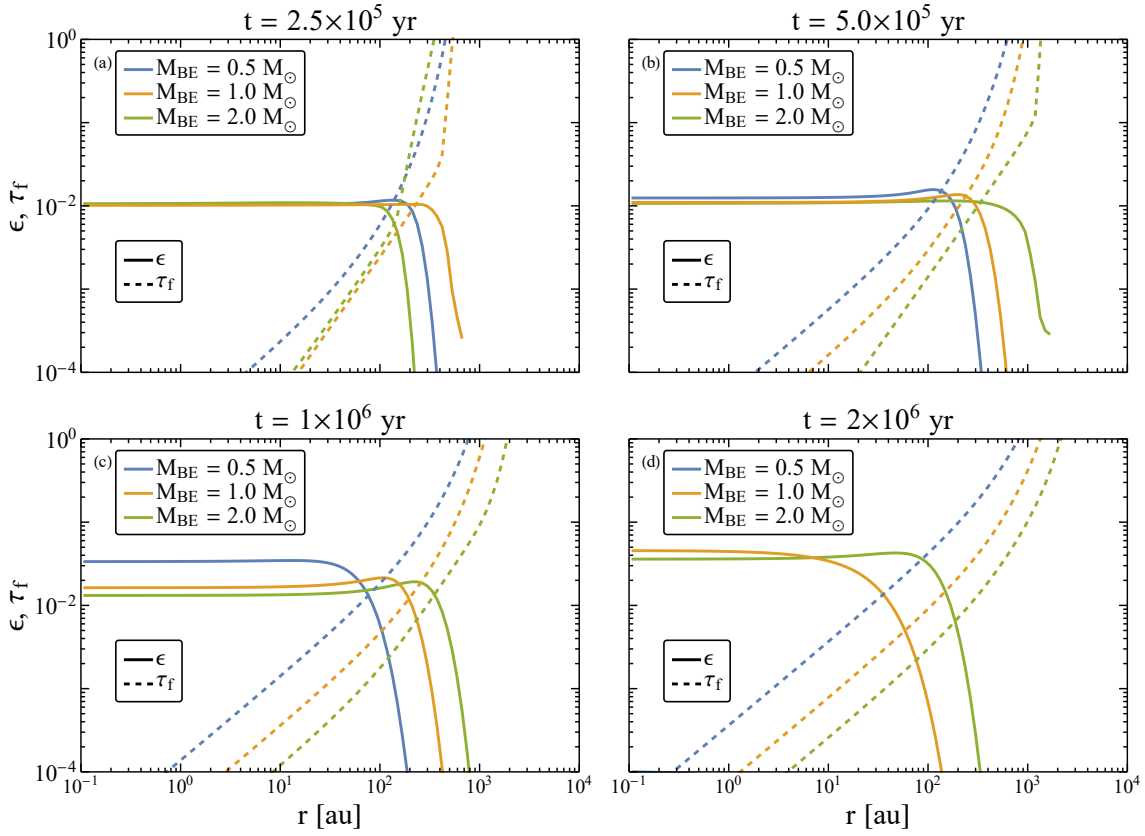

Figure 4.2.19: Dust-to-gas ratio at four snapshots in time of the three mass cases. The dust in the disk from the lowest mass core (blue curve) begins to rapidly drift inwards the earliest so it is drained the fastest. At $2 \cdot 10^6$ year this dust disk is completely drained, so it is now present in that snapshot. The more massive cores create dust disks which are more long lived, with the most massive one (green curve) creating the longest lived dust disk.

Chapter 5

Discussion & implications

In this chapter we begin by discussing the results of our parameter space study affects the gas disk, and compare these to relations measured observationally. We also discuss some caveats of the model. This is done in section 5.1. In section 5.2 we discuss the implications of our parameter space study on the dust disk. We discuss dust-to-gas ratios and the streaming instability active regions we find. Finally, we use these streaming instability active regions in our model to explore possible planet formation via pebble accretion.

5.1 The gas disk

During the viscous evolution phase we find accretion rates on to the star which range between $10^{-9} - 2 \cdot 10^{-5}$ to $\mathrm{M}_{\odot}\ \mathrm{yr}^{-1}$. The lower range of these are in agreement with observations, which show accretion rate in the range of $10^{-11} - 10^{-7}\ \mathrm{M}_{\odot}\ \mathrm{yr}^{-1}$ (Hartmann et al. 1998, 2016; Manara et al. 2016), see Figure 5.1.1. We however note that the accretion rates in this model could easily be changed by changing the choice of our viscosity parameter α_{m} in the disk, as $\dot{M}_{\mathrm{accrete}} \propto \alpha$. From the isochrones in panel (b) of Figure 4.2.9, we can see that the higher range of accretion rates we find are short lived, and the likelihood of observing a disk at that stage is therefore low. Even though the dissipation of the disk in this model is slower than one might expect, the general evolution of the accretion rate behaves roughly as one expects. Observationally, the decrease with age goes as $\dot{M} \propto t^{-\xi}$ with $\xi \sim 1.5$, and the increase with stellar mass goes as $\dot{M} \propto M_{\star}^{\zeta}$ with $\zeta \sim 1.2 - 3$ (Alcalá et al. 2014; Antoniucci et al. 2014; Fang et al. 2009; Herczeg & Hillenbrand 2008; Manara et al. 2012; Muzerolle et al. 2003; Natta et al. 2006; Sicilia-Aguilar et al. 2010; Venuti et al. 2014). We find $\xi = 1.1 - 1.7$ with ξ being higher for systems that come from cloud cores with lower angular momentum budget. For a given time we find ζ to be in the range $\zeta = 1.5 - 2.2$, depending on which time one looks at, and if one sets time zero to be the beginning of the cloud collapse or the end of the formation phase, with generally the

high values at late times. These values are in good agreement with the observed scaling relations.

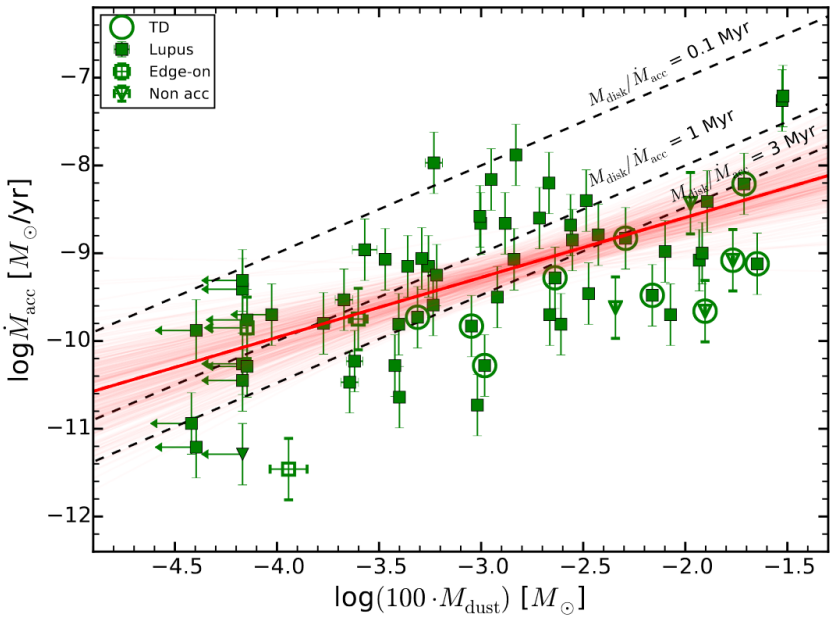

Figure 5.1.1: Stellar accretion rate as a function of 100 times the dust mass, as a gas mass proxy. The filled squares are class II objects and the open circles are transitions disks. The open squares and triangles are objects observed edge on and those whose accretion can be explained by chromospheric noise respectively. The red plot is a fit made to the class II objects and transition disks (disks with an inner cavity). The dashed lines show different values for $M_{\rm Disk}/\dot{M}_{\rm acc}$, which should be comparable with the system age. Credit: Manara et al. (2016).

The disk lifetime in the `refrun` case is long, even at $5 \cdot 10^6$ yr a significant disk with significant mass still, which would take several million years to accrete. Observationally, disks are expected to have lifetimes on the order of $\sim 3 \cdot 10^6$ yr, although ages up to 10^7 have been observed (Fedele et al. 2010; Haisch et al. 2001). In order to dissipate the disk within 5 Myr we need the disk to form very close to the star, with a low centrifugal radius as in the `Low` Ω_0 case. We can also compare this to Kimura et al. (2016) which modelled the evolution of protoplanetary disks, also starting at the collapse of a Bonnor-Ebert sphere. With their model they find disk lifetimes between 2-4 Myr. Their model includes heating due to the central star, viscous heating and heating from the infalling material, and photoevaporation. In their reference case they use a rotation rate which is $4.8 \cdot 10^{-14}$ s^{-1}, compared to $6.07 \cdot 10^{-14}$ s^{-1} used here. They do also examine rotation rates as high as $8.1 \cdot 10^{-14}$ s^{-1} and as low as $1.6 \cdot 10^{-14}$ s^{-1}.

With the long lifetimes of disks we have found in this study in mind, we can discuss the findings by Manara et al. (2018) showing that estimated masses of exoplanets in planetary

system are too large compared to estimates of dust masses in protoplanetary disks. One of the solutions they proposed to solve this tension was that the disk is refilled with material, either continuously or episodically. Our results indicates that supplying additional material to the disk would also increase the lifetime of the disk beyond observed limits. In the framework of this study, this speculative solution seem unlikely.

Manara et al. (2016) observed a relation between the disk mass and the stellar accretion rate. This can be seen in Figure 5.1.1. The relation found has a relation of $\dot{M} \propto M_{\text{Gas disk}}^{0.7}$, where the gas disk mass was taken as 100 times the measured dust disk mass[1]. Using Figure 4.2.9, one can try to understand where this relation may come from. Looking at the isochrones in panel (b), the accretion versus disk mass relation is slightly sub-linear at times $t < 10^6$ yr. At the $5 \cdot 10^6$ yr mark the relation follows $\dot{M} \propto M_{\text{Gas disk}}^{0.95}$, with the slope begin slightly shallower at earlier times. The is caused by variations in the rotation of the collapsing molecular cloud core. A similar relation is also seen when comparing different masses for the molecular cloud cores. Note that in these runs the cloud core rotation rate was also changed according to Equation (2.57). Therefore, what is found is not purely an effect of increasing the mass, but rather how different masses of stars which follow the mass-rotation rate relation of Equation (2.57) behave. At the end of the $5.0 \cdot 10^6$ yr run the accretion versus disk mass relation for the different mass cases goes as $\dot{M} \propto M_{\text{Gas disk}}^{0.82}$.

From panel (a) in Figure 4.2.9 one can see that for a given initial condition for the cloud core parameters, the relation follows a very steep curve with time. At times $> 5 \cdot 10^5$ yr after the end of the formation phase the reference case scales as $\dot{M} \propto M_{\text{Gas disk}}^{3.2}$. The near linear relation observed by Manara et al. (2016) could therefore be explained by varying initial conditions of the molecular cloud cores, while the vertical spread is due to the age difference between the systems. One caveat here is that the overlap in parameter space between our numeric model and the observations by Manara et al. (2016) is limited. This model only probes the upper right corner of parameter space in Figure 5.1.1. In light of this, an additional run was therefore made where the centrifugal radius is set to be 1 au. The results of this follows the same linear relation between accretion rate and disk mass, indicating that the behaviour would extend into the parameter space explored by Manara et al. (2016). Probing further into this parameter space could also be done by reducing the mass as well as the rotation rate, to further reduce the angular momentum budget of the cloud core.

Some caveats should be mentioned here, mainly regarding the thermodynamics of the disk. In this work we do not model viscous heating of the disk, which in a true α-disk model this

[1] Although not discussed previously, in our model the dust-togas disk ratio is close to 1/100 for $1.5 \cdot 10^6$ yr in the reference case, after which it quickly drops as the dust disk is depleted. Considering this, the assumption of Manara et al. (2016) that the gas disk is 100 times more massive than the dusk disk might not be valid for older disk where the dust has drained. However, considering the problem for theoretical protoplanetary disk models to maintain dust for the lifetime of the gas, whereas observations seem to indicate that dust is long lived (e.g. (Andrews et al. 2016)), the assumption of $M_{\text{Gas disk}} = 100 M_{\text{Dust disk}}$ could still be valid. Manara et al. (2016) also note that their direct gas disk mass measurements are very uncertain, which is why they are not used.

is expected to be important in the inner regions of the disk (Bitsch et al. 2015). However, since the nature of angular momentum transport in protoplanetary disks is becoming more uncertain and other means of evolving the disk could be at work (e.g. disk winds (Bai & Stone 2013)), the effect of viscous heating is uncertain.

When the disk becomes gravitationally unstable towards the end of the formation phase, the gravitational instability can also act as a heating source in the disk, which we have also not included. We also do not consider heating due to the infalling material, which is related to the infall rate of gas and dust onto the disk (Kimura et al. 2016), which also is high during the later stages of the formation phase. These effects would increase the disk temperature, increasing the sound speed and therefore the viscosity. However, these processes will mostly be active during the early formation phase of the disk. Their effect on the lifetime of the disk could therefore be minor.

We also do not model photoevaporation, which is the effect of X-ray and EUV photons launching disk winds that transport gas away from the disk (Owen et al. 2012, 2011, 2010). Photoevaporation is expected to happen at a rate of $\sim 10^{-9}$ $M_\odot$ yr^{-1}. Just by itself, photoevaporation would probably not affect results of the reference case very much, since this disk only reaches accretion rates of $\sim 10^{-8}$ $M_\odot$ yr^{-1} and photoevaporation would be a minor effect compared to this. However, the `Low` Ω_0 case does reach accretion rates close to 10^{-9} $M_\odot$ yr^{-1}. For this case photoevaporation could therefore become significant, and be the mechanism by which finally gets cleared of its gas component.

5.2 Dust evolution

As discussed in Section 1.2.2, from theoretical work dust disk lifetimes are expected to be short, as dust quickly grows to sizes where they drift inwards rapidly. The gas disk is expected to last a few million years (Fedele et al. 2010; Haisch et al. 2001). In the `refrun` case of this model fairly long dust lifetimes are found, on the order of a couple of millions of years for particles of 0.01 cm in size. However, in this case the gas lifetime is longer than the dust lifetime by a few million years. Therefore the large difference between dust and gas lifetimes still remains. In the `Large-dust` case, with 0.1 cm sized dust, the dust disk is drained in $\sim 10^6$ yr. In order to produce dust lifetimes that compare to that of the gas the dust needs to be very small, as found in the case where the dust size was set to 0.001 cm. However, such a small dust size is unlikely as the dust would grow collisionally until reaching the fragmentation/bouncing barrier (Birnstiel et al. 2010; Blum & Wurm 2000; Blum et al. 1998; Brauer et al. 2008; Poppe et al. 1999). To remain as small as 0.001 cm the coagulation efficiency of the dust particles would have to be very low. In order to keep a reservoir of small dust in the outer disk some mechanism which prevents the dust from growing large would be needed.

We find that the highest dust-to-gas ratio reached in the disk does not scale strongly with

the dust size. The reference case, with a dust size of 0.01 cm, reached a highest value of $\epsilon_{\mathrm{r\,=\,0.01\ cm}} = 0.051$. Dust with a size of 0.1 cm reaches the highest dust-to-gas ratio of $\epsilon_{\mathrm{r\,=0.1\ cm}} = 0.062$ and the dust with size 0.001 cm reaches a peak of $\epsilon_{\mathrm{r\,=0.001\ cm}} = 0.044$. However, as mentioned in Section 4.2.1, the smallest dust reaches this peak at the end of the $5 \cdot 10^6$ yr simulation and would continue to increase if the simulation ran for longer. Hence, one sees a small increase in the peak dust-to-gas ratio with dust size, within the $5 \cdot 10^6$ yr simulation. Similarly, the peak dust-to-gas ratio does not scale strongly with the cloud rotation rate either. The `Low` Ω_0 case and the $R_{\mathtt{c,Max}} = 50$ `au` case both peak at $\epsilon = 0.045$, only slightly lower than the `refrun`. In all of these different cases, the time at which the disk reaches the peak dust-to-gas ratio is different however. Larger dust and slower rotation rates peak faster, due to the faster dust drift in the former case and due to faster disk evolution in the latter case. Panel (a) in Figure 4.1.8 shows a contour plot of the dust-to-gas ratio over time and disk radius for the `refrun`.

Panel (b) in Figure 4.1.8 shows the ratio between the dust-to-gas ratio in the disk of the `refrun`, and the critical dust-to-gas ratio needed for the streaming instability to become active. In this model two generations of planetesimals can be created, one during the early parts of the disk formation phase, between $1.5 \cdot 10^4$ and $3 \cdot 10^4$ yr, at radii between 1 and 4 au, and another at times $8.5 \cdot 10^5$ and $\sim 2 \cdot 10^6$ yr at radii between 10 and 150 au.

The reason for why we see the early streaming instability active zone is not entirely clear. One possible explanation is that at such early times in the disk, the disk is not very massive and the gas surface densities are very low. Therefore, the Stokes numbers of dust particles are large, allowing particles to drift inwards efficiently. Meanwhile, material falls in with a constant dust-to-gas ratio. The combination of infalling material with constant dust-to-gas ratio and dust drifting inwards drives up the dust-to-gas ratio past the critical value needed for the streaming instability to become active. The second period of streaming instability in the disk starts because the dust has now begun to be dominated by drift. As dust particles with constant size drift inwards, the dust-to-gas ratio in the inner disk increases past the critical value needed to be come streaming instability active. This mechanism if dust pile up for constant particle size is the same as described in the semi-analytical model of Youdin & Shu (2002).

In the case of the dust with size $r_p = 0.1$ cm, this disk only becomes streaming instability active at $\sim 3 \cdot 10^5$ yr at radii of several tens of au, as seen in panel (b) of Figure 4.2.5. This periods lasts $\sim 5 \cdot 10^5$ yr, at the end of which it covers a radius range from a few to a few tens of au. The smallest dust case with size $r_p = 0.001$ cm also becomes streaming instability active, shown in panel (b) of Figure 4.2.4. This case becomes active after $\sim 3 \cdot 10^6$ yr at a few hundreds of au. It remains active until the end of the $5 \cdot 10^6$ yr simulation, and the regions moves inwards to between ~ 30 and ~ 100 au.

Table 5.1: Initial time and orbital radius of planetary embryos, and the dust particle size used for growing each planet.

Dust size [cm]	Initial orbital radius [au]	Initial time [yr]
0.01	4	$3.0 \cdot 10^4$
0.01	100	$1.0 \cdot 10^6$
0.01	40	$1.3 \cdot 10^6$
0.01	10	$1.7 \cdot 10^6$
0.1	40	$3.0 \cdot 10^5$
0.1	10	$5.0 \cdot 10^5$

With the results from the streaming instability condition in mind, a few runs are made where a planetary embryo of mass 0.01 $M_\oplus$ is inserted into the disk, at radii and times matching the streaming instability active regions of the simulation `refrun` and `Large-Dust`. It is thus assumed that a planetesimal 100 to 1000 km-sized planetesimal formed by the streaming instability is able to grow up to our chosen embryo mass through some combination of collisions and pebble accretion (Johansen & Lambrechts 2017). We then model the growth of the embryo via pebble accretion in the 3D regime as in Lambrechts et al. (2019) up to a mass of 10 $M_\oplus$. We do not consider a possible transition to the faster 2D pebble accretion regime Lambrechts & Johansen (2014). Planets then drift via type I migration, using a prescription from Lambrechts & Johansen (2014); Paardekooper et al. (2010). We also stop growth if the Stokes number of the dust near the planet core is $\leqslant 10^{-4}$, as such dust would be very well coupled to the gas and should not be swept up by the planet. It is further assumed that the dust scale height is given by $H_\mathrm{d} = 0.01 H_\mathrm{g}$. This is motivated by observations showing that dust disk appear to be flat (Pinte et al. 2016).

The 10 $M_\oplus$-limit is picked as this is the point where, crudely, the core can start to attract a gaseous envelope (Pollack et al. 1996) and starts opening a gap in the disk (Lubow & D'Angelo 2006). This represents approximately the end of growth by pebbles and, approximately, as the core reaches the so-called pebble isolation mass (Lambrechts et al. 2014). In reality, the latter is a function of the viscosity of the disk, the disk aspect ratio H/r, the Stokes number of the dust particles and the radial pressure gradient (Bitsch et al. 2018). However, in this work we use the more simple approach of simply looking at how fast a planet can grow to the point where it can attract a gas envelope. Both the disk with 0.01 cm sized dust and the one with 0.1 cm sized dust were investigated. The initial positions and times are shown in Table 5.1. It should be noted here that all these planets are grown independently of each other, and that the effect of each planet on the pebble flux through the disk is not taken into account.

An effect of limiting growth when Stokes numbers are smaller than 10^{-4} is that an embryo formed from the first generation of planetesimals at an orbital radii of a few au in the `refrun` grows very slowly. There is a short period before the Stokes number drops below the growth limit where the embryo can grow. Growth will begin again at later times

after approximately 10^6 yr when the Stokes numbers in this region increases to $> 10^{-4}$ again.

Panel (a) in Figure 5.2.1 shows how the mass of the planets accreting 0.01 cm sized pebbles grows over time. The planet which begins to form at $3 \cdot 10^4$ yr (red curve), from the early streaming instability region reaches a mass of 3.8 $M_\oplus$ in $\sim 10^6$ yr before the dust disk is drained. The blue and yellow curves show the two planets which starts to grow at 10^6 and $1.3 \cdot 10^6$ yr from the second streaming instability region, at radii of 100 au and 40 au respectively. The blue case reaches a mass of 1.1 $M_\oplus$. Interestingly, the yellow case catches up to the red and follow a mass growth which is very similar, also reaching a final mass of 3.8 $M_\oplus$, although as seen in panel (b) of Figure 5.2.1, they do so at different orbital radii. The final case (green curve) starts growing at $1.7 \cdot 10^6$ yr. It only reaches a final mass of 0.4 $M_\oplus$ before the dust disk is drained.

Panel (b) in Figure 5.2.1 shows the planet mass as a function of orbital radius. From this we can see that only the planet which starts to growing from the early generation of planetesimals (red curve) migrates to the inner edge of the disk. The blue case only migrates ~ 7 au to an orbital radius of 93 au. The yellow case migrates from an initial position of 40 au to 20 au after $5 \cdot 10^6$ yr. The last planet to start growing (green case) migrates from 10 au to 8 au during the simulation. It should be noted here that at the end of the $5 \cdot 10^6$ year run, the gas disk is still significant in this `refrun` case. Therefore the planets would likely keep migrating further if the simulation was extended.

Figure 5.2.2 shows the same panels as Figure 5.2.1, but for planets growing with 0.1 cm sized pebbles. This disk becomes streaming instability active earlier in the outer disk compared to the 0.01 cm case, so planet formation can start earlier in the outer regions of the disk. From panel (a) in Figure 5.2.2 we see that both planets grow to 10 $M_\oplus$ within $\lesssim 10^5$ yr. From panel (b) we can also see that the planets do not migrate significantly before they reach a mass of 10 $M_\oplus$, at which point we stop the planets from both growing and migrating. The planet starting that forms at 40 au (blue curve) migrates in to 37.2 au and the planet starting at 10 au (yellow curve) migrates to 8.4 au.

We thus demonstrate that planets can form within a timespan of less than 10^6 yr, during and shortly after the formation phase of the disk. If indeed the observed ring structures in the young protoplanetary disks are a signpost of embedded giant planets, this appears to be consistent with our findings. We would thus argue that the presence of giant planets in the very young ($\lesssim 10^6$ yr) embedded disk of HL Tau (ALMA Partnership et al. 2015) should not be excluded based on theoretical grounds.

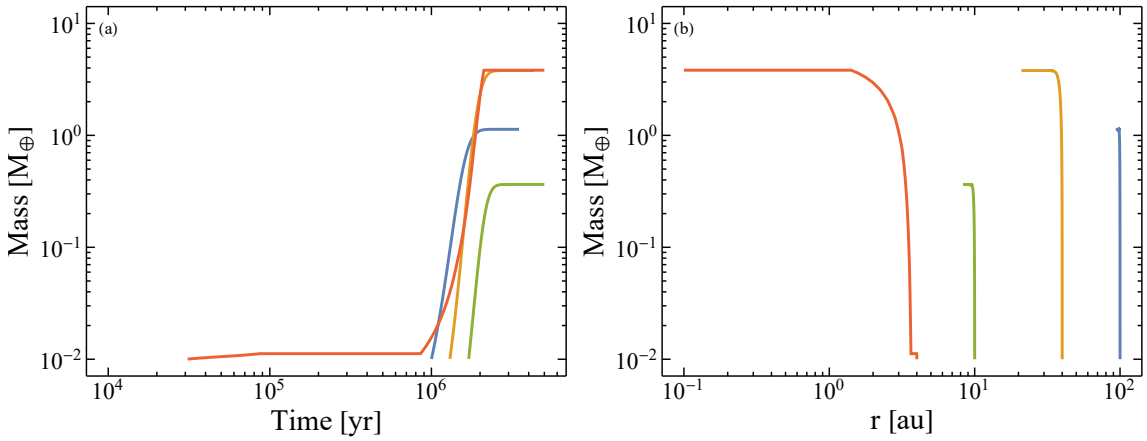

Figure 5.2.1: Panel (a): Growth of a planet core growing with 0.01 cm pebbles over time. The time at which each planet core starts to grow and migrate is shown in Table 5.1. The planet starting to grow at $3 \cdot 10^4$ yr (red curve) only starts to grow significantly after $\sim 9 \cdot 10^5$ yr, due to Stokes number begin to low at earlier times. It reaches a final mass of 3.8 $M_\oplus$. The next core to form (blue case) reaches a mass of 1.1 $M_\oplus$. The third planet which forms (yellow curve) happens to the same final mass as the first, 3.8 $M_\oplus$. The final planet (green curve) only manages to reach a mass of 0.3 $M_\oplus$. What causes the planets to stop growing in all cases is that the dust disk is drained. **Panel(b):** Growth tracks of each planet core showing the mass as a function of radius. Only the first planet which forms (red curve) migrates to the inner edge of the disk. The other cases migrate from 100 au to 93 au (blue curve), 40 au to 20 au (yellow curve) and 10 au to 8 au (green curve).

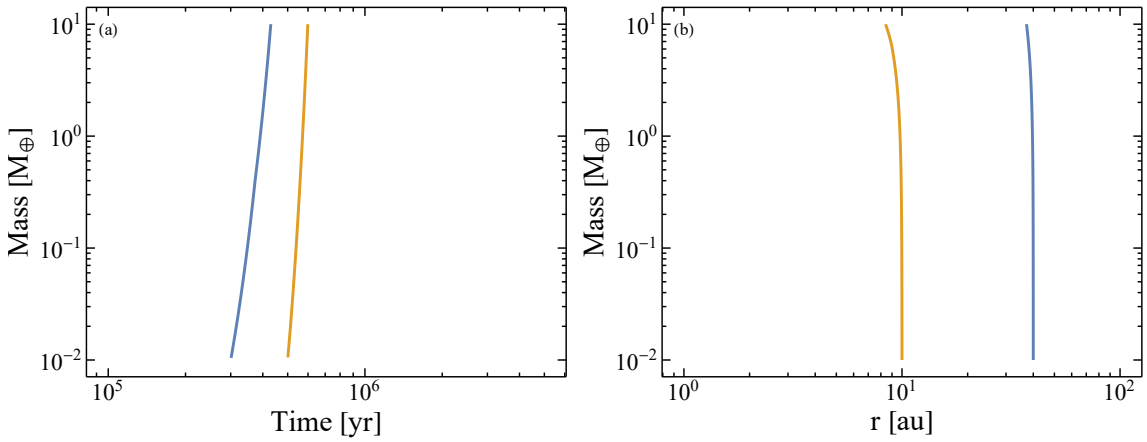

Figure 5.2.2: Panel (a): Growth of a planet core growing with 0.1 cm pebbles over time. The time at which each planet core starts to grow and migrate is shown in Table 5.1. Both cores growing from 0.1 cm sized pebbles take $\lesssim 10^5$ yr to reach a mass of 10 $M_\oplus$. **Panel(b):** Growth tracks of each planet core showing the mass as a function of radius. Since the planets grow so quickly, neither planet significantly migrates inwards in the disk.

Chapter 6

Conclusions

In this work we have investigated the formation of a protoplanetary disk from the gravitational collapse of a molecular cloud core, and the subsequent viscous evolution of the disk. The molecular cloud core was modelled by a Bonnor-Ebert sphere, since observations of molecular cloud core follow the density profile of such a sphere (Alves et al. 2001; Kandori et al. 2005; Kirk et al. 2005; Teixeira et al. 2005). An investigation into how the initial conditions of the molecular cloud core affect the disk evolution was made.

We find that cloud cores collapse on a time scale of 1 to a few 10^5 yr. For a given temperature, the duration of the cloud core collapse scales nearly linearly with the mass of the cloud core.

The lifetime of the protoplanetary disk is tied to the initial angular momentum budget of the collapsing molecular cloud core, with higher angular momentum budgets leading to larger, more massive and longer lived disks. In this model, the produced lifetimes are on the long end, $> 5 \cdot 10^6$ yr for the reference case. One possible explanation for the long disk lifetimes is that the centrifugal radius and hence the angular momentum that is deposited in the disk is overestimated. Shorter lifetimes can be achieved by more slowly rotating cloud cores and/or angular momentum loss in the collapse.

From the perspective of interpreting observations, we do not identify a single relation between stellar mass accretion rate and disk mass. Rather, for a given accretion rate the corresponding disk will depend on the initial angular momentum budget of the cloud, as this will determine how large a fraction of infalling material lands on the disk, and how spread out it is. A combination of different ages and different initial conditions is proposed as an explanation for the spread in accretion rate versus disk mass found by (Manara et al. 2016), with the caveat that the explored parameter space only has limited overlap. Although test made here seem to indicate that the behaviour found in this model would extend further into the parameter space observed by Manara et al. (2016).

In exploring how the size of the dust affect the evolution of the dust disk it was found that

the dust size has a minor effect on the highest dust-to-gas ratio reached in the disk, but it has a significant effect on when the peak is reached. Dust of size 0.1 cm reaches a peak dust-to-gas ratio of $\epsilon = 0.062$ at $t = 6.8 \cdot 10^5$ yr, compared to a peak dust-to-gas ratio of $\epsilon = 0.051$ at $1.9 \cdot 10^6$ yr for the 0.01 cm sized dust. The dust with a size of 0.001 cm peaked at $\epsilon = 0.044$ at the end of the $5.0 \cdot 10^6$ yr simulation. Because it peaked right at the end, it is likely that the dust-to-gas ratio would keep increasing if the simulation ran for longer.

From the range of dust sizes we explored, between 0.001 cm and 0.1 cm, all the cases we explore become streaming instability active at some point. Due to the different times at which they reach the peak in dust-to-gas ratio, they becomes streaming instability active at different times and regions in the disk. In the case with 0.1 cm sized dust, the disk becomes streaming instability active between $\sim 3 \cdot 10^5$ to $\sim 8 \cdot 10^5$ yr, at radii between ~ 70 to ~ 1 au. The 0.01 cm sized dust becomes streaming instability active in two generations. The first occurs in the early parts of the disk formation phase, $1.5 \cdot 10^4 - 3.0 \cdot 10^4$ yr, at radii between ~ 1 and ~ 4 au. For the 0.001 cm sized dust the streaming instability becomes active after $\sim 3 \cdot 10^6$ yr and remains active until the end of the simulation at $5.0 \cdot 10^6$ yr. It starts at radii of ~ 300 au, and at the end it is active between $\sim 30 - 100$ au. We do however note that these result depend on our assumptions of fixed particle sizes and that the results are sensitive to the temperature structure of the disk, which we do not model in detail. Hence, more detailed modelling of the thermodynamics, and including dust coagulation and fragmentation in the model can shed some more light on the validity of these results.

Growth of giant planet cores via pebbles accretion can be quite rapid in the `refrun` case. Planet cores that grow by 0.1 cm sized pebbles grow to a mass of 10 $M_\oplus$ in a few 10^5 yr. Due to the early onset of streaming instability in this disk, the embryo also forms as early as $3 \cdot 10^5$ yr, creating the potential of forming a giant planet core in $< 10^6$ yr. In the disk with 0.01 cm sized pebbles the streaming instability does become active in the inner disk earlier. But due the smaller sized dust particles growth is slower and none of the planets reach 10 $M_\oplus$ before the dust disk is drained. However, we do form a number of planets of a few Mars masses to a few Earth masses at several different orbital radii.

6.1 Future outlook

In terms of improving this model, its most obvious drawback is the previously mentioned lack of more detailed thermodynamics. Hueso & Guillot (2005) used a model where the midplane temperature of the disk is calculated from the effective temperature of the disk using irradiation from the central star and viscous heating. They approximate the vertical radiative transfer though the disk as a combination of optically thin and thick components, using an expression from Nakamoto & Nakagawa (1994). As Hueso & Guillot (2005) state, the temperature evolution is numerically non-trivial since the temperature depends on

the disk viscosity, which in turn depends on the temperature. However, recent disk wind models question the efficiency of viscous heating (Mori et al. 2019).

Better modelling of the dust would also be a good improvement. Models that take into account both fragmentation and coagulation of dust exists (e.g. Birnstiel et al. (2012); Brauer et al. (2008)). This would allows us to calculate particle sizes in a more self-consistent manner, taking into account the effects of coagulation, bouncing and fragmentation. Additionally, the process of particle sublimation is expected to be important near the ice lines, which are regions in the disk where the various chemical components of the disk transition from gas to solid, (Ros & Johansen 2013; Schoonenberg & Ormel 2017). The improved dust modelling would therefore be further improved by more detailed thermodynamics.

Some aspects of parameter space are left unexplored in this work so far. The temperature of the molecular cloud core will affect its collapse. For a given mass, the radius of the Bonnor-Ebert sphere shrinks with the sound speed, and thus the temperature, see Equation (3.11). Doubling the temperature of the molecular cloud cores shrinks has the same effect as halving the mass. It also makes the collapse faster. For a 1 $M_\odot$ Bonnor-Ebert sphere at a temperature of 20 K, the collapse phase lasts $\sim 0.9 \cdot 10^5$ yr, compared to the $\sim 2.5 \cdot 10^5$ yr for the same case at 10 K. Currently, the streaming instability and planet growth was only explored for different dust sizes in the reference case. Considering that this gas disk is very long lived, i.e. it still has a very massive disk at 5 Myr, compared to the expectations from observations, streaming instability and planet formation should be examined in the cases with disk lifetimes more in line with these expectations.

Modelling the evolution of lower mass stars would also be interesting, as M-dwarfs are seen as a promising location for Earth-like planets in the habitable zone, e.g. Trappist 1 (Gillon et al. 2017). This becomes computationally more expensive however. It would require extending the integration grid further inwards, which makes the times step small. Such disks also become more viscous due to the lower stellar mass since the viscosity depends on the Keplerian frequency as $\nu \propto \Omega_\mathrm{k}^{-1}$ and $\Omega_\mathrm{k} \propto M_\star^{-1/2}$, which further reduces the time step, as it is inversely proportional to the viscosity.

Another direction to go is to trace the chemical evolution in the disk as Pignatale et al. (2018) did. They used a model for protoplanetary disk formation and evolution to trace the evolution of various chemical species in the disk. With their model they are able to explain the over-abundance of refractory elements in the outer regions of the Solar system. They also find that materials with different thermal histories are mixed locally, which agrees qualitatively with the three main chondrite groups. Setting time zero of the Solar system to the beginning of the cloud core collapse, the authors also find that calcium-aluminium-rich inclusions (CAIs), whose absolute age can be determined accurately through radioisotope dating, from abundantly between $t \sim 40$ kyr and ~ 70 kyr. This agrees very well with the radio-isotopic dating.

Bibliography

Alcalá, J. M., Natta, A., Manara, C. F., et al. 2014, A&A, 561, A2

ALMA Partnership, Brogan, C. L., Pérez, L. M., et al. 2015, ApJ, 808, L3

Alves, J. F., Lada, C. J., & Lada, E. A. 2001, Nature, 409, 159

Andrews, S. M., Wilner, D. J., Zhu, Z., et al. 2016, ApJ, 820, L40

Ansdell, M., Williams, J. P., van der Marel, N., et al. 2016, ApJ, 828, 46

Antoniucci, S., García López, R., Nisini, B., et al. 2014, A&A, 572, A62

Bai, X.-N. & Stone, J. M. 2013, ApJ, 769, 76

Balbus, S. A. & Hawley, J. F. 1991, ApJ, 376, 214

Ballering, N. P. & Eisner, J. A. 2019, AJ, 157, 144

Bath, G. T. & Pringle, J. E. 1981, MNRAS, 194, 967

Bergin, E. A., Cleeves, L. I., Gorti, U., et al. 2013, Nature, 493, 644

Birnstiel, T., Dullemond, C. P., & Brauer, F. 2010, A&A, 513, A79

Birnstiel, T., Klahr, H., & Ercolano, B. 2012, A&A, 539, A148

Bitsch, B., Johansen, A., Lambrechts, M., & Morbidelli, A. 2015, A&A, 575, A28

Bitsch, B., Morbidelli, A., Johansen, A., et al. 2018, A&A, 612, A30

Blum, J. & Wurm, G. 2000, Icarus, 143, 138

Blum, J. & Wurm, G. 2008, ARA&A, 46, 21

Blum, J., Wurm, G., Poppe, T., & Heim, L.-O. 1998, Earth Moon and Planets, 80, 285

Bonnor, W. B. 1956, MNRAS, 116, 351

Brauer, F., Dullemond, C. P., & Henning, T. 2008, A&A, 480, 859

Burkert, A. & Bodenheimer, P. 2000, ApJ, 543, 822

Chandrasekhar, S. 1957, An introduction to the study of stellar structure (Dover)

Duric, N. 2004, Advanced astrophysics (University Press)

Ebert, R. 1957, Zeitschrift fur Astrophysik, 42, 263

Fang, M., van Boekel, R., Wang, W., et al. 2009, A&A, 504, 461

Fedele, D., van den Ancker, M. E., Henning, T., Jayawardhana, R., & Oliveira, J. M. 2010, A&A, 510, A72

Galli, D., Lizano, S., Shu, F. H., & Allen, A. 2006, ApJ, 647, 374

Galván-Madrid, R., Liu, H. B., Izquierdo, A. F., et al. 2018, ApJ, 868, 39

Gillon, M., Triaud, A. H. M. J., Demory, B.-O., et al. 2017, Nature, 542, 456

Goldreich, P. & Tremaine, S. 1980, ApJ, 241, 425

Goldsmith, P. F., Bergin, E. A., & Lis, D. C. 1997, ApJ, 491, 615

Goodman, A. A., Benson, P. J., Fuller, G. A., & Myers, P. C. 1993, ApJ, 406, 528

Haisch, Jr., K. E., Lada, E. A., & Lada, C. J. 2001, ApJ, 553, L153

Hartmann, L., Calvet, N., Gullbring, E., & D'Alessio, P. 1998, ApJ, 495, 385

Hartmann, L., Herczeg, G., & Calvet, N. 2016, ARA&A, 54, 135

Hayashi, C. 1981, Progress of Theoretical Physics Supplement, 70, 35

Herczeg, G. J. & Hillenbrand, L. A. 2008, ApJ, 681, 594

Hueso, R. & Guillot, T. 2005, A&A, 442, 703

Isella, A. 2006, PhD thesis, Universita' degli Studi di Milano

Isella, A., Guidi, G., Testi, L., et al. 2016, Physical Review Letters, 117, 251101

Johansen, A. & Lambrechts, M. 2017, Annual Review of Earth and Planetary Sciences, 45, 359

Johansen, A., Oishi, J. S., Mac Low, M.-M., et al. 2007, Nature, 448, 1022

Kandori, R., Nakajima, Y., Tamura, M., et al. 2005, AJ, 130, 2166

Kimura, S. S., Kunitomo, M., & Takahashi, S. Z. 2016, MNRAS, 461, 2257

Kirk, J. M., Ward-Thompson, D., & André, P. 2005, MNRAS, 360, 1506

Lambrechts, M. & Johansen, A. 2012, A&A, 544, A32

Lambrechts, M. & Johansen, A. 2014, A&A, 572, A107

Lambrechts, M., Johansen, A., & Morbidelli, A. 2014, A&A, 572, A35

Lambrechts, M., Morbidelli, A., Jacobson, S. A., et al. 2019, arXiv e-prints

Li, Z.-Y., Banerjee, R., Pudritz, R. E., et al. 2014, Protostars and Planets VI, 173

Lubow, S. H. & D'Angelo, G. 2006, ApJ, 641, 526

Manara, C. F., Morbidelli, A., & Guillot, T. 2018, A&A, 618, L3

Manara, C. F., Robberto, M., Da Rio, N., et al. 2012, ApJ, 755, 154

Manara, C. F., Rosotti, G., Testi, L., et al. 2016, A&A, 591, L3

McClure, M. K., Bergin, E. A., Cleeves, L. I., et al. 2016, ApJ, 831, 167

McKee, C. F. & Ostriker, E. C. 2007, ARA&A, 45, 565

Miotello, A., Testi, L., Lodato, G., et al. 2014, A&A, 567, A32

Miotello, A., van Dishoeck, E. F., Williams, J. P., et al. 2017, A&A, 599, A113

Mori, S., Bai, X.-N., & Okuzumi, S. 2019, ApJ, 872, 98

Muzerolle, J., Hillenbrand, L., Calvet, N., Briceño, C., & Hartmann, L. 2003, ApJ, 592, 266

Najita, J. R. & Bergin, E. A. 2018, ApJ, 864, 168

Nakagawa, Y., Sekiya, M., & Hayashi, C. 1986, Icarus, 67, 375

Nakamoto, T. & Nakagawa, Y. 1994, ApJ, 421, 640

Natta, A., Testi, L., & Randich, S. 2006, A&A, 452, 245

Owen, J. E., Clarke, C. J., & Ercolano, B. 2012, MNRAS, 422, 1880

Owen, J. E., Ercolano, B., & Clarke, C. J. 2011, MNRAS, 412, 13

Owen, J. E., Ercolano, B., Clarke, C. J., & Alexander, R. D. 2010, MNRAS, 401, 1415

Paardekooper, S.-J., Baruteau, C., Crida, A., & Kley, W. 2010, MNRAS, 401, 1950

Pascucci, I., Testi, L., Herczeg, G. J., et al. 2016, ApJ, 831, 125

Pignatale, F. C., Charnoz, S., Chaussidon, M., & Jacquet, E. 2018, ApJ, 867, L23

Pinte, C., Dent, W. R. F., Ménard, F., et al. 2016, ApJ, 816, 25

Pollack, J. B., Hubickyj, O., Bodenheimer, P., et al. 1996, Icarus, 124, 62

Poppe, T., Blum, J., & Henning, T. 1999, Advances in Space Research, 23, 1197

Pringle, J. E. 1981, ARA&A, 19, 137

Ros, K. & Johansen, A. 2013, A&A, 552, A137

Schoonenberg, D. & Ormel, C. W. 2017, A&A, 602, A21

Shakura, N. I. & Sunyaev, R. A. 1973, A&A, 24, 337

Shu, F. H. 1977, ApJ, 214, 488

Sicilia-Aguilar, A., Henning, T., & Hartmann, L. W. 2010, ApJ, 710, 597

Takahashi, S. Z., Inutsuka, S.-i., & Machida, M. N. 2013, ApJ, 770, 71

Teixeira, P. S., Lada, C. J., & Alves, J. F. 2005, ApJ, 629, 276

van Dishoeck, E. F., Blake, G. A., Draine, B. T., & Lunine, J. I. 1993, in Protostars and Planets III, ed. E. H. Levy & J. I. Lunine, 163–241

Venuti, L., Bouvier, J., Flaccomio, E., et al. 2014, A&A, 570, A82

Ward, W. R. 1997, Icarus, 126, 261

Weidenschilling, S. J. 1977, MNRAS, 180, 57

Yang, C.-C., Johansen, A., & Carrera, D. 2017, A&A, 606, A80

Youdin, A. N. 2010, in EAS Publications Series, ed. T. Montmerle, D. Ehrenreich, & A. M. Lagrange, Vol. 41, 187–207

Youdin, A. N. & Goodman, J. 2005, ApJ, 620, 459

Youdin, A. N. & Shu, F. H. 2002, ApJ, 580, 494

Zhu, Z., Hartmann, L., & Gammie, C. 2010, ApJ, 713, 1143

Zsom, A., Ormel, C. W., Güttler, C., Blum, J., & Dullemond, C. P. 2010, A&A, 513, A57